Abdalraheem A. Ijjeh, M.Sc. Eng.

FEASIBILITY STUDY OF ARTIFICIAL INTELLIGENCE APPROACH FOR DELAMINATION IDENTIFICATION IN COMPOSITE LAMINATES

A dissertation submitted to the Scientific Board of the Szewalski Institute of Fluid-Flow Machinery, Polish Academy of Sciences in partial fulfillment of the requirements for the Degree of Doctor of Philosophy

Supervisor:
Paweł Kudela, D.Sc. Ph.D. Eng.

July 2022

DEDICATION

To my beloved family.

ACKNOWLEDGMENTS

I would like to express my deepest sense of gratitude to my supervisor, Prof. Paweł Kudela, for his guidance, encouragement, and valuable advice on my research and writing over the whole period of my study. I would like to thank him for his endless support from the initial stage of my PhD studies till the end and for helping me develop a thorough understanding of the subject and my studies. I would also like to thank him for passing on to me his expertise and knowledge of being a scientific researcher.

I would like to express my gratitude to Dr. Maciej Radzienski for supplying the experimental data of the full wavefield measured by SLDV used in the validation of the developed methods in this thesis.

My sincere thanks to my father, Dr. Abdullah Ijjeh, for his continuous guidance, advice, and encouragement throughout my life.

I would like to thank my mother for her endless love, trust, encouragement, and support throughout my life.

I would like to thank my wife, Duaa, and my daughter, Raghad, for their consistent support and encouragement.

I would like to thank my brother, Dr. Abdalraheman Ijjeh, for his consistent support and advice.

And finally, I would like to thank everyone who supported me during my journey of PhD studies.

ABSTRACT

Structural health monitoring (SHM) and non-destructive testing (NDT) approaches are employed to predict the structural remaining functional life via proper diagnosis and prognosis methods. As a result, the purpose is to detect and characterise defects that may risk the integrity and functionality of a structure. However, it is observed that the progress in the fields of SHM and NDT, which utilise elastic waves, has slowed down in recent years. It may be attributed to the limitations of classic techniques of signal processing applied to a complex and challenging problem of the extraction of damage-related features from signals of propagating waves. On the other hand, the accelerated progress in the field of artificial intelligence (AI) methods in recent years, mainly in deep learning and computer vision, revealed new dimensions for solving problems and offered the opportunity to be implemented and integrated with the NDT and further with SHM methods.

The main objective of the dissertation is to develop a novel AI-driven diagnostic system for delamination identification in composite laminates such as carbon fibre reinforced polymers (CFRP). Hence, the potential of utilising artificial intelligence-based approaches to investigate damage identification based on the propagation of Lamb waves is explored. The developed AI systems adopt an end-to-end strategy capable of processing the animation of propagating Lamb waves directly into the damage map.

Additionally, the issue of the slow data acquisition of high-resolution full wavefield imaging techniques was raised. Hence, to overcome such an issue, I present a deep learning approach to recover the high-resolution frames of Lamb wave propagation and their interaction with delamination and boundaries of the structure from low-resolution measurements. Consequently, such a method will speed up the data acquisition process.

In summary, in this dissertation I will investigate the feasibility of utilising full wavefields of Lamb wave propagation in CFRP composite laminates with various deep learning-based approaches to identify delamination in composite laminates.

Following an introductory chapter and a review of the state-of-the-art (Chapters 1-3), I am discussing my contribution to the field in Chapter 4, which consists of four parts:

- Development of a fully connected convolutional neural network (CNN) classification model capable of detecting and localising delamination in a CFRP plate utilising a bounding box method.
- Delamination identification using fully convolutional networks (FCN) trained on input images representing energies computed from full wavefield signals, in which the FCN models are capable of performing pixel-wise image segmentation.
- Delamination identification based on the animation of the full wavefield, in which the model is capable of identifying the delamination in the CFRP plate only by utilising the full wavefield images of Lamb wave propagation.
- Super-resolution image reconstruction, in which the developed deep learning model is capable of recovering the high-resolution full wavefield of Lamb wave propagation from low-resolution measurements which are below the Nyquist sampling rate.

Furthermore, the developed models were verified on experimentally acquired data in CFRP specimens with single and multiple Teflon inserts representing delamination, indicating that the developed models can be used for delamination detection and localisation and further their size estimation.

The results for all developed models are presented in Chapter 5 along with a discussion followed by conclusions and a description of future work in Chapter 6.

PUBLICATIONS

Journal papers

- Ijjeh, Abdalraheem A., Saeed Ullah, and Pawel Kudela. "Full wavefield processing by using FCN for delamination detection." Mechanical Systems and Signal Processing 153 (2021): 107537.
- Ijjeh, Abdalraheem A., and Pawel Kudela. "Deep learning based segmentation using full wavefield processing for delamination identification: A comparative study." Mechanical Systems and Signal Processing 168 (2022): 108671.
- Saeed Ullah, Ijjeh, Abdalraheem A., and Pawel Kudela. "Deep learning approach for delamination identification using animation of Lamb waves." Structural Health Monitoring, SAGE (Under review)
- Ijjeh, Abdalraheem A., Saeed Ullah, Maciej Radzienski and Pawel Kudela. "Deep learning super-resolution for the reconstruction of full wavefield of Lamb waves." Mechanical Systems and Signal Processing (Under review).

Conference papers

- Ijjeh, A., Kudela, P. Feasibility Study of Full Wavefield Processing by Using CNN for Delamination Detection. Proceedings of the International Conference on Structural Health Monitoring of Intelligent Infrastructure, Porto, Portugal, 30 June - 2 July 2021, ISSN 2564-3738, pages 709 – 713.
- Ijjeh, A., Kudela, P. (2023). Delamination Identification Using Global Convolution Networks. In: Rizzo, P., Milazzo, A. (eds) European Workshop on Structural Health Monitoring. EWSHM 2022. Lecture Notes in Civil Engineering, vol 270. Springer, Cham. https://doi.org/10.1007/978-3-031-07322-9_5

Scientific monographs

- Abdalraheem Ijjeh, Machine Learning for SHM: Literature Review, chapter in: Wybrane zagadnienia inżynierii mechanicznej, Praca zbiorowa pod redakcja M.

Mieloszyk, T. Ochrymiuka, Wydawnictwo Instytutu Maszyn Przepływowych PAN, Gdańsk, 2020, ISBN 978-83-88237-97-3.

- Abdalraheem Ijjeh, Data-driven based approach for damage detection, chapter in: Wybrane zagadnienia inżynierii mechanicznej 2021, Praca zbiorowa pod redakcja M. Mieloszyk, T. Ochrymiuka, Wydawnictwo Instytutu Maszyn Przepływowych PAN, Gdańsk, 2021, ISBN 978-83-66928-00-8.

- Abdalraheem Ijjeh, Deep Learning based Damage Imaging techniques, chapter in: Wybrane zagadnienia inżynierii mechanicznej 2022, Praca zbiorowa pod redakcja M. Mieloszyk, T. Ochrymiuka, Wydawnictwo Instytutu Maszyn Przepływowych PAN, Gdańsk, 2022 (Accepted).

Internships during study

- Erasmus+, "Wave propagation in phononic crystals", 05/06/2022 – 10/06/2022, ISEN-JUNIA, CNRS-IEMN, Lille, France, under supervision of Dr. Marco Miniaci.

TABLE OF CONTENTS

LIST OF TABLES

LIST OF FIGURES

Chapter 1

Introduction

The presented work in this dissertation is an outcome of a 3-year project, Feasibility studies of artificial intelligence-driven diagnostics, funded by the Polish National Science Center under grant agreement no. r2018/31/B/ST8/00454.

1.1 Problem statement

Carbon fibre reinforced plastic (CFRP) materials have a wide range of applications in different industries due to their characteristics such as high strength, low density, and resistance to fatigue and corrosion. However, composite structures are exposed to different types of operating conditions during their service life, such as temperature variations and cyclic loading, which ultimately result in initiating damage. Moreover, composite structures are subject to several operating conditions (such as temperature variations and cyclic loading) during their service life, which eventually can initiate fatigue damage in the composite structures. Furthermore, damage mechanisms in composite structures are more complex than those in conventional metallic structures due to the multi-layer property and general anisotropy [1].

One of the main damage types developed in composite structures is inter-laminar delamination. Delamination is developed from matrix micro-cracks in a nonlinear manner with the application of cyclic loading [1, 2], which can alter the compression strength of composite laminates and gradually affect the composite structure to encounter failure by buckling. Therefore, it can seriously decrease the performance of composite structures. Consequently, delamination identification in its early stages can significantly help avoid catastrophic structural collapses.

Various approaches of non-destructive evaluation (NDE) and structural health monitoring (SHM) have been utilised for damage detection in composite structures. Such approaches can be divided into two categories: model-based approaches and data-

driven approaches.

The model-based approaches for SHM aim to reflect the process of damage development in composite materials by implementing a physics-based numerical model and introducing necessary variables to adjust the model to fit the actual application scenario [1]. However, model-based approaches have practical shortcomings that restrict their suitability to simple structures in well-controlled environments. On the other hand, the data-driven approaches for SHM utilise registered data from the structure under different structural states and perform an analysis using data analysis methods. Data-driven approaches that utilise artificial intelligence methods such as deep learning are getting more popular due to the recent advancements in sensing technology. Hence, the deep learning-based approach revealed new dimensions for resolving problems and offered the opportunity to be implemented and integrated with the NDE and further with SHM approaches. Consequently, applying deep learning techniques can handle issues regarding data preprocessing and feature extraction. Nowadays, end-to-end approaches have been developed in which unprocessed data is directly fed into the model to generate a damage map as an output. Consequently, the model will learn to recognise the patterns and detect the damage.

1.2 Purpose of the study

In recent years, artificial intelligence (AI)-based approaches have been utilized by numerous scientific fields. Accordingly, I aim to utilise AI-based approaches in the field of NDT/SHM to develop an AI-driven diagnostic system for delamination identification in composite laminates. Adopting the AI approach will contribute to various aspects of NDT/SHM, elastic wave behaviour, image processing, and animation processing. Therefore, I propose an end-to-end deep learning approach that is capable of performing automatic feature extraction of the delamination characteristics, implying that the supervised deep learning model will learn by itself to extract the damage features and accordingly detect and localise the damage in the investigated composite laminates. A supervised learning-based approach was adopted for this purpose. Accordingly, a large dataset that was numerically generated representing the full wavefield of propagating elastic waves is implemented. It should be underlined that the computation of such a dataset is time-consuming (3 months). As a result, I expect such a system will be an extra safety factor for operational structures, thereby reducing maintenance costs.

1.3 Objectives and motivations

The main objective of the work is to develop an artificial intelligence (AI) driven diagnostic system for delamination identification in composite laminates. Furthermore, to explore the potential of utilising artificial intelligence-based approaches to investigate damage detection and identification based on the propagation of Lamb waves. Data corresponding to elastic wave propagation has very complex patterns of wave reflections. It is difficult to explicitly program instructions that will output a damage map of an element of a structure based on anomalies in propagating elastic waves (e.g., reflections from discontinuities). Hence, this research aims to explore possible solutions that employ deep neural networks (DNN), as they are promising approaches. The progress in the machine learning field in the last decade, along with increasing computation power capabilities, makes it a perfect time to investigate potential applications of DNN. DNN is an emerging tool that has successful applications in computer vision and speech recognition, among other applications. Nowadays, certain neural network (NN) architectures surpass human-level accuracy in image classification. The main advantage of DNN in comparison to other machine learning approaches is scalability. It means that the performance of DNN increases with NN size as well as the size of the dataset used for supervised learning.

Therefore, it is possible to use an end-to-end approach in which DNN processes the animation of propagating waves (input) directly into a damage map (output).

Another objective of this research is to address the issue of slow data acquisition of high-resolution full wavefields of Lamb wave propagation. Hence, to overcome such an issue, I aim to develop a deep learning system capable of recovering the high-resolution frames of Lamb wave propagation and their interaction with delamination and boundaries from low-resolution measurements with high accuracy. Consequently, such a system will speed up the data acquisition process.

This research will help answer legitimate questions regarding the utilisation of deep learning techniques by processing the full wavefield of propagating elastic waves for delamination identification in composite laminates:

- Can the proposed AI-driven diagnostic model be more accurate than the conventional signal processing technique?
- Knowing that experimental signals contain noise, is it adequate to use a numerical model for generating a dataset?

- Can a technique such as data augmentation enhance the training of deep learning models?
- How well can deep learning models generalise to new unseen data? Further, to experimental data acquired by SLDV?
- Is it computationally feasible to utilise all frames of propagating waves, or can utilisation of certain frames be efficient enough?
- Does the implementation of different deep learning architectures result in different accuracies in damage identification? Is the comparison metric among these architectures sufficient for determining the efficient one?
- Do deep learning techniques for delamination identification utilised in this thesis have any potential for practical applications in the long term?
- Can deep learning techniques developed for super-resolution image reconstruction be used to recover the high-resolution full wavefield frame from the low-resolution measurements with adequate accuracy to detect the damage?

1.4 Thesis contribution

The novelty of this work consists of applying for the first time a full wavefield dataset of elastic wave propagation (a numerically generated dataset) as an input to various supervised deep neural networks, which is capable of identifying damage. Accordingly, two main approaches were adopted:

1. One-to-one approach
2. Many-to-one approach

For the one-to-one approach, the developed models take one input image (Root Mean Square (RMS) of the full wavefield frames) and generates one output image of the damage map. The developed models that are based on one-to-one approach are:

- Res-UNet
- VGG16 encoder-decoder
- PSPNet
- FCN-DenseNet
- GCN

Whereas, for the many-to-one approach, a number of frames (representing the propaga- of elastic waves) are fed to the developed models in order to generate a damage map. For such an approach, an autoencoder ConvLSTM model was developed.

Furthermore, I have developed deep learning models to perform an end-to-end super-resolution technique regarding elastic wave propagation and their interaction with the damage and the specimen boundaries. Accordingly, a low-resolution input frame is acquired using a uniform mesh grid with a low number of scanning points. Then, the low-resolution frames are fed to a deep learning model to produce high-resolution frames. Later, the predicted high-resolution frames can be fed to the many-to-one models to identify the damage.

1.5 Thesis organisation

The thesis is organised as follows:

Chapter 2 introduces structural health monitoring (SHM) and its applications, in particular guided waves based SHM for composite materials. Furthermore, an introduction to damage detection and localisation using guided waves is presented.

Chapter 3 introduces artificial intelligence approaches utilised for SHM applications. Furthermore, in chapter 3 conventional machine learning approach consists of data preprocessing, feature extraction, and classification techniques are presented. Moreover, a detailed illustration of the deep learning approach is presented. Finally, a related data-driven-based SHM for damage detection and localisation is presented.

Chapter 4 introduces the acquisition of the synthetic dataset that resembles the full wavefield of the propagating Lamb waves in a plate made of CFRP and their interactions with discontinuities, i.e., the damage and the boundaries of the plate. Furthermore, in chapter 4 various damage detection and localisation techniques are presented. Finally, I present an end-to-end deep learning model utilised for super-resolution image reconstruction that can be utilised for delamination identification.

Chapter 5 presents the evaluation of the developed deep learning models on numerical test cases to demonstrate their capability to predict previously unseen data.

Furthermore, the developed models were also evaluated on experimentally acquired data with single and multiple Teflon inserts representing delamination to investigate their ability to generalise.

Chapter 6 presents the conclusions of this dissertation, and further, it presents the potential future works that could be carried out from the present work.

Chapter 2

State of the art in Structural Health Monitoring

Structural health monitoring (SHM) intends to describe a real-time evaluation of the materials of a structural component or the full construction during the life-cycle of the structure [3]. Furthermore, SHM supports detecting and characterising defects in structures as a whole or in their parts. Detection of structural defects is critical because they may impair the safety of the structure during its operation [4].

The purpose of SHM is to identify any potential change that occurs in a structure that could affect the performance of the entire system at the earliest possible time so that an action can be taken to reduce the downtime, operational costs, and maintenance costs, consequently reducing the risk of catastrophic failure, injury, or even loss of life. Moreover, SHM improves the work organization of maintenance services by replacing scheduled and periodic maintenance inspections with performance-based maintenance. It decreases maintenance labour, in particular, by avoiding dismounting undamaged parts and by reducing individual involvement [3].

We can look at SHM as an improved method to perform Non-Destructive Evaluation (NDE). Nonetheless, SHM involves sensors that are integrated into structures, data transmission, computational power, and processing ability within structures [3]. The typical organization of an SHM system is depicted in Fig. 2.1. Such a system is built from a diagnostic part (low level) and a prognosis part (high level). The diagnostic part is responsible for detecting, localising, and evaluating the damage. The prognosis part includes the production of information concerning the outcomes of the diagnosed damage. In general, we can categorize SHM strategies into two main schemes: local and global schemes. Local schemes were discussed in [5, 6] and global schemes were discussed in [7–9]. Local schemes aim at monitoring a small area of the structure enclosing the transducers that are used for registering the data signals after the structure

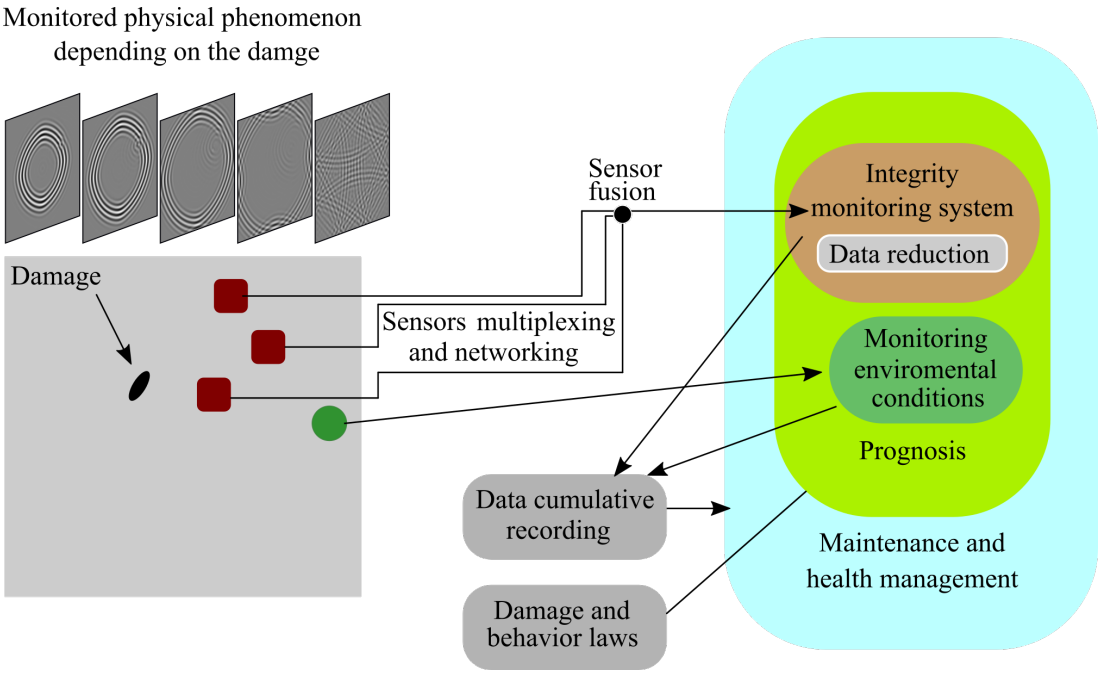

Figure 2.1: Organization of SHM systems.

is exited. For this purpose, a few phenomena are used, like ultrasonic waves [6], eddy currents [5], and acoustic emission [10]. On the other hand, global schemes are related to the global behaviour of the structure [3]. For this purpose, vibration techniques are utilised, which can be classified as signal-based and model-based. Signal-based approaches related to passive SHM systems analyse measured responses of the structure after ambient excitation to identify possible defects [11]. While in active SHM, the structure can be externally exited using e.g. PZT transducers or shakers.

The model-based approaches use various types of models of a monitored structure to detect and localise damage in the structure by utilising relations between the model parameters and distinct damage features [11].

2.1 SHM for composite materials

Composite materials are widely used in various industries, due to their useful characteristics. A composite material can be described as a compound of two or more different materials to acquire new features that cannot be achieved by specific components functioning individually. Distinct from metallic alloys, which are isotropic materials, each material in the composite has its characteristics [12]. Accordingly, several advantages from these various characteristics can be obtained. Generally, composite materials are categorized into [13]:

- Fibre-reinforced composite materials consisting of three parts: the fibres as the discontinuous phase, the matrix as the continuous phase, and the fine inter-phase region, also known as the interface [14].
- Laminated composite materials are an assembly of multiple layers of fibre-reinforced or fabric-reinforced composite materials (e.g. plain weave, twill) that can be combined to implement necessary design features [15].
- Particulate composite materials are characterized as being composed of particles suspended in a matrix (e.g. composite with short fibres).

When comparing composite materials to regular metallic materials, we can notice that composites have some advantages over metallic materials. The advantages can be summarized as [12]:

- low density with high strength and stiffness,
- high vibration damping capacity, and more temperature resistance,
- strong texture in micro-structures, making it easy to design and satisfy different application needs,
- chemical and corrosion resistance.

However, composite materials have some disadvantages. Due to the nature of multiphase materials, composite materials present anisotropic characteristics. It is considered a disadvantage in the case of wave propagation because of the complexity of the processing of registered signals.

Damage can accidentally occur in composite materials, either during the process of manufacturing or during the regular service life of the structure. The lack of reinforcement in the out-of-plane direction causes composite materials to be susceptible to impact damage [16]. Under a high energy impact, little penetration rises in composite materials. Furthermore, low to medium energy impacts can initiate delamination, which is caused by bending cracks, matrix cracking, and shear cracks, which mostly happen below the top surfaces and are barely visible [16]. Delamination can alter the compression strength of composite laminate, and it will gradually affect the composite to encounter failure by buckling [17]. The tension encountered by the composite structure creates cracks and produces delamination between the laminates, which leads to more damage [17]. Furthermore, when a composite laminate encounters low- or high-velocity impact, various damage modes can appear, including fibre crack, matrix crack, delamination, and fibre pullout. All of these damage modes are dependent on

the impact parameters, such as impact energy, impactor mass, or impactor shape [17]. Moreover, additional types of damage can also occur, such as debonding, which occurs when an adhesive stops adhering to an adherend. These defects can seriously decrease the performance of composites. Hence, they should be detected in time to avoid catastrophic structural collapses.

The concept of an SHM system in composite structures is to use a built-in structural diagnostic system, which usually consists of three main components [18]:

- Actuator/sensor technology, which can be embedded in an inspected structure to register and transmit the structural response.
- For real-time condition monitoring of the structure, the registered data needs to be processed by high-performance computing equipment in the control center.
- Data interpretation software for monitoring the registered responses from the in-service structure.

Therefore, it is a crucial step when developing a diagnostic system to integrate and embed sensors with the composite structure. Accordingly, several types of sensors can be integrated and embedded into a composite structure, such as piezoelectric transducers (PZT), optical fibre sensors (e.g., Fiber Bragg grating (FBG)), and Micro-electromechanical Systems (MEMS).

Consequently, defects can only be discovered by analysing the responses of the structure, obtained by sensors, before and after damage occurrence. Accordingly, we cannot expect to have "damage sensors". The only way to detect the damage is by processing and comparing signals received from the sensors before and after the damage occurrence [19]. Subsequently, one can attempt to classify extracted features, which are sensitive to minor damage and can be distinguished from the response to natural and environmental disturbances [19]. Thus, SHM methods in composite materials are essential for damage detection and estimation since SHM implies different types of sensors mixed with damage detection techniques.

2.2 Guided waves based SHM

The approach of adopting elastic wave propagation methods in SHM includes the generation of elastic waves in the examined structure and recording their displacement as a function of time [20]. The generated waves propagate until they reflect from discontinuities, edges, or damage in the structure. The reflected waves contain information about the location and the size of the damage.

Designing a robust SHM system requires knowledge in various scientific fields (e.g., mechanical and electrical engineering, as well as computer science, mathematics, and physics) [21]. Moreover, it requires a deep understanding of various material types and the design of transducers working alone and in networks. Also, there is a need to be familiar with signal processing methods and damage evaluation techniques [21].

In the literature, I will focus on the guided wave-based SHM techniques for composite materials, which have attracted much attention in the past two decades [22]. Guided waves are essentially elastic waves propagating within bounded structures [22], e.g., in a thin plate, elastic waves are guided by the boundaries of the plate.

There are a few benefits from adopting guided wave-based schemes for SHM in structures over vibration-based methods. Generally, transducers utilised in SHM systems are affordable, and due to the lightweight of those transducers, they can be implemented easily in the structure. In addition, it is possible to scan a relatively large area compared to a small number of transducers [22]. Moreover, an important advantage for guided waves over a vibration-based scheme is their high sensitivity for detecting small defects due to the ability to use high-frequency signals (excited and registered). In such a case, guided waves are not sensitive to low-frequency vibrations [22, 23].

Various types of guided waves have been investigated for SHM. A well-known approach is the use of Lamb waves, which propagate within thin plates and shells bounded by stress-free surfaces [22]. Lamb waves were given their name after Horace Lamb, who discovered them and developed a theory to describe the phenomena of their propagation [20]. However, Lamb could not generate those waves physically until Worlton [24] saw the opportunity to utilise Lamb waves characteristics in damage detection [20]. Lamb waves, in general, are generated and registered by piezoelectric (PZT) transducers [16]. Due to the multi-mode and dispersion properties, the propagation of Lamb waves is quite complex [20]. In practical applications, two forms of Lamb waves arise depending on the distribution of the displacement on the top and bottom bounding surfaces. These forms are symmetric, denoted as $S_0, S_1, S_2, \ldots$, and antisymmetric, denoted as $A_0, A_1, A_2, \ldots$, [20]. Fig. 2.2 illustrates the propagation of the fundamental Lamb waves for A_0 and S_0 modes in a structure.

Regardless of the promising characteristics of Lamb waves, using them for SHM applications poses some essential challenges. Among them is the dispersive nature of Lamb wave propagating modes that can convert into each other in the presence of defects and other changes in the mechanical impedance [25]. Moreover, due to some flaws in the bonding within actuators, sensors, and the structure, random noise will emerge in the relevant sensors due to the high sensitivity of Lamb waves toward structural

(a) A_0 mode

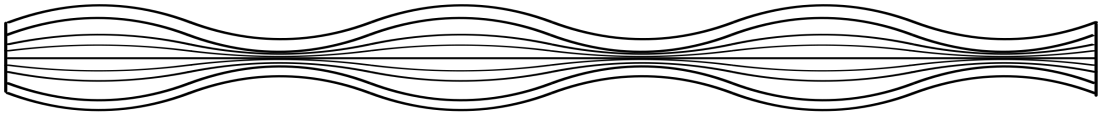

(b) S_0 mode

Figure 2.2: Fundamental Lamb wave modes: (a) A_0 mode, (b) S_0 mode

perturbations. Noise arising from environmental sources, like temperature changes or anisotropy of the material, also summed up to the received signals, making them very complicated and challenging to recognize and interpret [25]. Moreover, an essential point concerns the choice of a carrier frequency for the Lamb waves, because the higher the frequency is, the damage detection of small size is more likely to be detected. However, when the frequency increases, the number of propagating wave modes will increase accordingly. As a result, multiple wave modes propagate and each wave mode has a different velocity, which causes a problem with reflection identification and misinterpretation of the location and size of the damage [20]. It was found that each wave mode shows varying sensitivity to individual damage. Kessler et al. [26] and Ihn et al. [27] found that $A0$ mode is suitable for delaminations to be detected in composite materials, and $S0$ mode was found suitable for crack detection in metallic elements [27, 28]. It was also observed that the design of the transducer influences in a great manner the excited and registered wave modes [29].

2.3 Damage detection and localisation using guided waves

Damage can be defined as changes that occur in a system, either deliberately or accidentally, that adversely alter the current or future performance of the system [30]. Generally, guided wave-based SHM systems can be built upon the processing of signals registered by different types of sensors such as PZTs, optical fibre sensors (e.g., FBG), in addition to Scanning Laser Doppler Vibrometry (SLDV), which is currently considered a Non-Destructive Test (NDT) tool.

2.3.1 Piezoelectric transducer

Piezoelectric transducers (piezoceramic PZT) are utilised in SHM systems to excite guided waves within structures and capture the reflected signals. Based on the arrangement of PZTs, two main approaches are available: *pulse-echo* and *pitch-catch* as presented in Fig. 2.3. In *pulse-echo*, it is possible to have a group of PZTs located nearby, which can be excited to generate Lamb waves. The reflected waves from damage are registered at the same or another PZT. Hence, this method depends on the reflection of waves from the damage. While in the *pitch-catch* approach, generated Lamb waves by PZTs (actuators) are transferred through the damage and registered at PZTs (sensors).

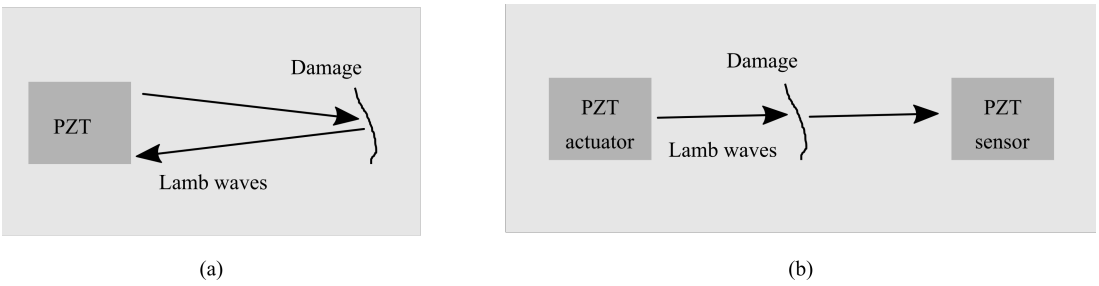

Figure 2.3: (a) Pulse echo (b) Pitch catch.

In general, configurations of PZT transducers for damage detection and localisation for SHM can be classified into two main arrangements, which are *concentrated* and *distributed* arrangements. Hence, a lot of work has been performed in the literature utilising PZT configurations for generating and sensing Lamb waves.

The following research articles are examples in which the authors used the *concentrated* transducers arrangement. Giurgiutiu [31] implemented a PZT wafer active sensor (PWAS) in a phased array to investigate Lamb waves in plates. The results that he obtained were encouraging regarding the location of the damage and its size. Additionally, Wilcox [32], investigated omni-directional wave transducer arrays for the rapid inspection of large areas of plate structures. In his work, two arrangements of PZTs were examined. The first one consists of a densely circular area with PZTs in which it presents an excellent concentrated peak at the location of the reflector, though it requires plenty of transducers. The other arrangement consists of a single circular ring of PZTs, which is quite efficient in any circumstance that involves various reflectors. Moreover, Malinowski et al. [33] performed a numerical analysis on an array of PZTs of a star shape for various damage scenarios. Their method confirmed good damage localisation.

Furthermore, the *distributed* arrangement was implemented in many research articles. In this arrangement, PZT transducers are spread over the entire inspected area. Schubert [34] tested different types of the above-mentioned arrangements. Moreover, Qiang et al. [35] used a rectangular network of transducers on composite material, whereas a triangular network of transducers was examined in [36] for an isotropic specimen.

It can be concluded from previous work that using these approaches for damage detection and localization is only suitable for simple structures. Furthermore, the estimation of damage size is very challenging. It is because of the limited information extracted from the registered signals at discrete PZT locations. These challenges arise due to various limitations (e.g., the added mass and attached cables to the structure alter the propagating waves). Additionally, it is difficult to distinguish the registered signals among different objects (e.g. bolts and rivets), the edges, and the actual damage. Another challenge arises due to the effect of temperature on propagating guided waves, as it will change their amplitude and phase (the arrival time) [37]. Therefore, the increase in the temperature will cause the amplitude of the guided waves to decrease and the arrival time to increase. Therefore, it becomes important to compensate for this issue [38]. Moreover, it is impossible to obtain high-resolution damage influence maps with a sparse array of sensors. To overcome these limitations, a full wavefield measurement approach was introduced. As a result of utilising a full wavefield, a damage influence map is produced, which makes it possible to estimate the size of the damage [39].

2.3.2 Scanning Laser Doppler Vibrometry

Scanning Laser Doppler Vibrometer (SLDV) was developed and presented in experimental research in the early 1980s. SLDV employs the Doppler frequency shift principle to measure the velocity of a moving object, in which the amount of the shifted frequency depends on the velocity of the moving object [40]. SLDV links a computer-controlled XY scanning mirror with a camera inside the optical head, which densely scans the vibrating surface of the structure and gets a large number of high-resolution measurements [41]. Essentially, the grid of points resembles a dense array of PZTs. Application of such a dense array of PZTs would be otherwise impractical. Hence, SLDV is employed for full wavefield measurements instead of PZT arrays. Consequently, vibrations of a structure and the propagation of guided waves can be measured accurately [39].

However, in many situations, it is necessary to obtain information about the vibrations of the measured object in three dimensions. In such situations, a 3D vibrometer is used, which holds three 1D scanning vibrometer heads in addition to the data

acquisition system and a control system. A 3D vibrometer measures a location with three independent laser beams that hit the target from three different directions, which yields a measurement of the complete in-plane and out-of-plane velocity of the target.

SLDV has been broadly used for sensing Lamb waves. Several works in the literature are concentrated on damage imaging methods for damage identification by using the signals sensed at a grid of points and recorded by SLDV. For instance, authors in [42] applied a frequency wavenumber domain analysis utilising a 2D Fourier transform to detect a crack in an aluminium plate. The method of wavenumber frequency filtering of SLDV data was applied for damage imaging in [43]. Authors in [44] introduced a new method of imaging crack growth in a structure. In the proposed method, they employed full wavefield data captured by SLDV. Also, authors in [45] utilized SLDV based measurement for inferring the dispersion curves for $A0$ Lamb wave mode. Moreover, SLDV has been used to scan and capture Lamb waves in various types of composite plates for damage detection [46–51].

Despite all the advantages of utilising SLDV, there are some disadvantages. The first drawback concerns the surface of the specimen, which must be smooth and characterised by proper reflectivity. Otherwise, the captured signal-to-noise ratio will be decreased [39]. Furthermore, experimenting with using SLDV requires a lot of time since the SLDV performs measurements at a single point in space at a time. Due to registering a full wavefield of Lamb waves, the process of measurements must be repeated by keeping the same excitation and pausing until the wave completely attenuates [39].

2.4 Compressive sensing of wavefield

As previously stated, guided waves, specifically Lamb waves, are frequently used for SHM and NDT. For point-wise measurements in the former scenario, an array of transducers is typically used. These are typically piezoelectric transducers that can function as actuators as well as sensors, as in active guided wave-based SHM. It should be emphasized that round-robin actuator-sensor measurements can be performed very quickly, allowing for near-real-time monitoring of a structure.

There has been a lot of recent research on the application of SLDV for NDT [44, 52–55]. For guided wave excitation, either a piezoelectric transducer or a pulse laser is utilized, and measurements are taken by SLDV at one location on the surface of an inspected structure. The method is continued automatically for other points in a scanning fashion until the full wavefield of Lamb waves is obtained.

Full wavefield measurements are taken on a very dense grid of points opposite to

sparsely measured signals by sensors. Hence, they deliver much more useful data from which information about damage can be extracted in comparison to signals measured by an array of transducers. On the other hand, SLDV measurements take much more time than measurements conducted by an array of transducers. It makes the SLDV approach unsuitable for SHM, in which continuous monitoring is required. But it is very capable for offline NDT applications.

One can imagine that in the future, a matrix of laser heads instead of the single laser head used nowadays will be developed to reduce SLDV measurement time. Alternatively, compressive sensing (CS) and/or deep learning super-resolution (DLSR) can be applied. It means that SLDV measurements can be taken on a low-resolution grid of points and then the full wavefield can be reconstructed at high-resolution.

CS was originally proposed in the field of statistics [56, 57] and used for efficient acquisition and reconstruction of signals and images. It assumes that a signal or an image can be represented in a sparse form in another domain with appropriate bases (Fourier, cosine, wavelet). On such a basis, many coefficients are close to or equal to zero. The sparsity can be exploited to recover a signal or image from fewer samples than required by the Nyquist–Shannon sampling theorem. However, there is no unique solution for the estimation of unmeasured data. Therefore, optimisation methods for solving under-determined systems of linear equations that promote sparsity are applied [58–60]. Moreover, a suitable sampling strategy is required.

Since then, CS has found applications in medical imaging [61], communication systems [62], and seismology [63]. It is also considered in the fields of guided waves and ultrasonic signal processing [64–70]

Harley et al. [64] utilised a general model for Lamb waves propagating in a plate structure (without defects) and L_1 optimisation strategies to recover their frequency-wavenumber representation. They applied sparse recovery by basis pursuit and sparse wavenumber synthesis. They used a limited number of transducers and achieved a good correlation between the true and estimated responses across a wide range of frequencies. Mesnil et al. [65] were focused on the reconstruction of a wavefield that includes the interaction of Lamb waves with delamination. Similar to previous studies, analytic solutions were utilised to create a compressive sensing matrix. However, the limitation of these methods is that dispersion curves of Lamb waves propagating in the analysed plate have to be known a priori.

Perelli et al. [66] incorporated the warped frequency transform into a compressive sensing framework for improved damage localisation. The wavelet packet transform and frequency warping were used in [67] to generate a sparse decomposition of the

acquired dispersive signal.

Di Ianni et al. [68] investigated various bases in compressive sensing to reduce the acquisition time of SLDV measurements. Similarly, a damage detection and localisation technique based on a compressive sensing algorithm was presented in [69]. The authors have shown that the acquisition time can be reduced significantly without losing detection accuracy.

Another application of compressive sensing was reported in [70]. The authors used signals registered by an array of sensors for tomography of corrosion. They investigated the reconstruction success rate depending on the number of actuator-sensor paths.

The group of DLSR methods is applied mostly to images [71–73] and videos [74, 75]. Image super-resolution (SR) is the process of recovering high-resolution images from low-resolution images. A similar approach can be used in videos, where data is treated as a sequence of images. Notable applications are medical imaging, satellite imaging, surveillance and security, and astronomical imaging, amongst others. Also, deep learning super sampling developed by NVIDIA and FidelityFX super-resolution developed by AMD were adopted for video games [76]. Mostly supervised techniques are employed, which benefit from recent advancements in deep learning methods ranging from enhanced convolutional neural networks (CNN) [74], through an extension of PixelCNN [71] to generative adversarial networks (GANs) [73], to name a few. Nevertheless, so far neither of these methods has been applied to the wavefields of propagating Lamb waves. The exception is an enhancement of wavefields as the second step of SR preceded by classic CS [77, 78].

2.5 Summary

Engineering structures are vulnerable to several types of damage that may occur naturally or artificially. Hence, the damage will reduce the expected lifetime of the running structures, increase their maintenance costs, and sometimes lead to catastrophic consequences. Therefore, to avoid such consequences, SHM techniques are applied.

In this chapter, several SHM approaches for detecting and localising damage within composite structures that utilise guided Lamb waves were presented. I demonstrated that guided-wave based SHM systems can be built by processing signals registered by PZTs or SLDV. Furthermore, the wavefield acquisition process can benefit from the latest advancements in sparsity-based signal processing studies. Hence, compressive sensing theory was introduced, which is a remarkable example in this field.

Chapter 3

Deep learning approaches for SHM

Artificial Intelligence (AI) refers to the ability of machines to imitate the human mind in such a way as "learning and problem-solving" [79]. AI has various definitions, however, it can be defined as any device that can sense its environment and consequently takes steps that maximize its opportunity of accomplishing its goals [79]. Historically, AI was introduced in 1956 at the Dartmouth summer conference by John McCarthy. For many years after the Dartmouth summer conference, AI has been in "AI winter" due to the lack of computational power. Moreover, its algorithms were not fully understood mathematically. However, in recent years, AI has returned to the stage for several reasons. The first reason was the advanced evolution that occurred in technology that produced high computational powers (e.g., graphics processing units (GPU)). GPU computational power exceeds that of traditional Central Processing Units (CPUs) due to the high capability of parallel computing, which makes it more efficient in running algorithms for large datasets. The second reason is the tremendous amount of data available nowadays, which can remarkably improve the learning process of an AI system, as its effectiveness depends on learning from its environment.

In general, AI can be divided into two classes: Strong AI and weak AI. Tab. 3.1 presents the main differences between them.

Table 3.1: AI classes

Category	**Strong AI**	**Weak AI**
Definition	Sort of AI that possesses the same human intellectual capabilities, or exceeds it.	Sort of AI that is utilised for a specific application design.
Purpose	To surpass and replace the human mind	To imitate the human intellectual thinking.

Engineering structures such as buildings, roads, tunnels, power generation systems, rotating machinery, and aircraft are considered important in our modern life. However, such structures are prone to various types of damage. Therefore, it is essential to

maintain them and keep them safe during their operational lifetime. Health monitoring presents an essential tool in management activities as it allows identifying early and progressive structural damage [80]. Obtained data from monitoring structures is large and needs to be transformed into valuable information to assist the development and design of maintenance activities, improve safety, reduce uncertainties, and extend our knowledge regarding the monitored structure.

SHM is one of the most robust tools for managing infrastructure. Traditionally, the procedure of performing an autonomous damage identification for engineering structures, such as civil, mechanical or aerospace, is referred to as SHM [81]. SHM aims to describe a real-time evaluation of a structure during its life-cycle [3]. Moreover, SHM assists in detecting and characterizing damage in a structure as a whole or its parts. Damage detection in a structure is crucial since it may reduce safety and performance during its operational lifetime [4]. Furthermore, the SHM approach involves monitoring a structure continuously through an array of sensors that periodically measure the response of the structure, then extracting the sensitive damage features from these measurements to perform statistical analysis on these features to examine the condition of the structure.

Generally, there are two approaches to SHM: physics-based and data-based. In the physics-based approach, the inverse problem method is applied in which numerical models such as finite element models are implemented. Damage identification results by comparing the registered readings from the structure with the estimated data from the models. On the other hand, the data-based approach is related to the AI domain (machine learning and deep learning), in which models are developed to learn the behaviour of the structure based on earlier registered data, leading to performing pattern recognition for damage identification.

The data-based approach can be applied to both supervised and unsupervised learning [82]. Supervised learning can be utilised in the field of SHM where data of the damaged and undamaged conditions is available in which the detection models can train [83]. On the other hand, unsupervised learning is applied when only undamaged cases are available. Therefore, the detection models train only on such data [83].

3.1 Machine learning approach

Machine learning (ML) is a sub-field of AI that belongs to the computer science field. ML is defined as "the ability of a computer to learn without being explicitly programmed" [84].

The conventional way of software engineering is through creating rules by humans and then combining them with data to find a solution to a problem. Alternatively, when it comes to ML, it utilises data and answers to learn the rules behind the problem [85]. In Fig. 3.1 the conventional software programming and ML are presented in (a) and (b) respectively. In ML, machines have to run through a learning process to learn inference rules, which are responsible for controlling the relations within a phenomenon. Hence, it is called an ML.

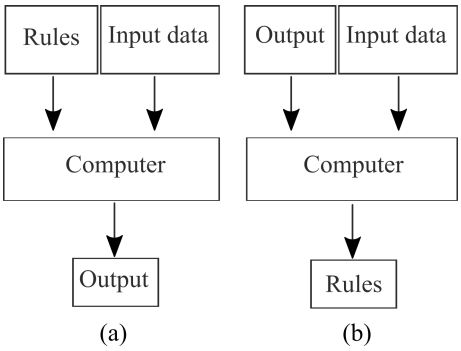

Figure 3.1: (a) Conventional Programming (b) Machine learning.

ML techniques in SHM were heavily utilised by researchers for damage detection [22, 86, 87]. Moreover, ML techniques attempt to map the patterns of the input data acquired by sensors to output targets for damage estimation at different levels. Accordingly, ML techniques demand high domain knowledge of the examiner to perform hand-crafted damage-sensitive feature extraction on the raw data acquired by sensors before being fed into a suitable ML model. Generally, the process of damage-sensitive features extraction (hand-crafted) in the field of SHM emerged due to the enormous development in the physics-based SHM techniques such as modal strain energy (MSE) [88], modal curvature (MC) [89], modal assurance criterion (MAC), and coordinate (MAC) [90], modal flexibility (MF) [91], damage locating vector (DLV) [92], wavelet transform [93, 94] and probabilistic reconstruction algorithm (PRA) [95] among others.

Different methods can be implemented when performing ML. Generally, those methods are grouped into four approaches: supervised learning, unsupervised learning, reinforcement learning, and transfer learning. Fig. 3.2 shows the different types of ML approaches.

Supervised learning is the task of training a machine to learn how to develop inference rules from the training data and how to map inputs with outputs. The training data is a collection of variables together with their labels (e.g., a set of civil images) of structures that are labelled as damaged or undamaged (healthy). During the learning process, the machine gets a collection of inputs simultaneously with the corresponding

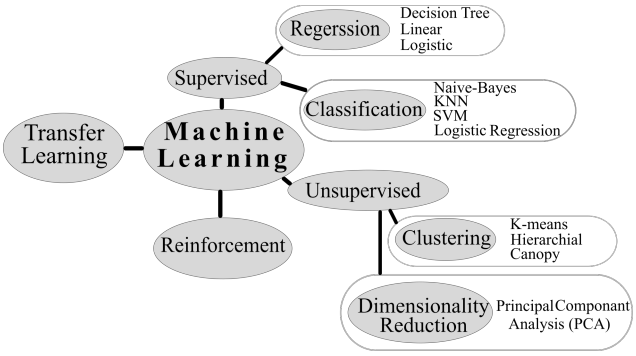

Figure 3.2: Machine Learning Approaches.

label (ground truth). Accordingly, by comparing its predicted output with the correct output to find errors, it modifies the model and the learning occurs [96]. Supervised learning uses patterns to predict the values of the output label for new unlabeled data by applying methods like regression and classification [96].

Unsupervised Learning is applied to such data with no historical labels [96]. In this case, the model does not know the ground truth labels of the input values. Therefore, the algorithm needs to figure out some common characteristics among the input values. Consequently, unsupervised learning is more difficult than supervised learning due to the absence of supervision, which implies the problem becomes less defined.

Reinforcement learning is based on the trial and error principle, which means the algorithm learns through actions that explore the environment in a way that results in the greatest rewards [79]. The reinforcement learning process consists of three parts: the agent, which is responsible for making decisions; the environment that relates to any interaction with the agent; and the actions that are taken by the agent. Figure. 3.3 illustrates the procedure of the reinforcement learning approach.

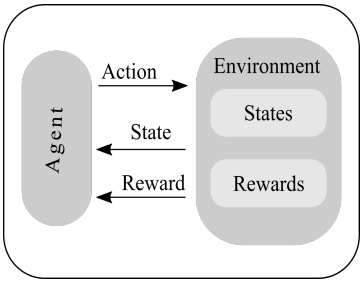

Figure 3.3: Reinforcement Learning.

Transfer learning differs in a way compared to the traditional ML approaches designed for particular tasks, implying that their learning and knowledge can not be transferred from one model to another. Therefore, when starting a new ML task, we have to start

from scratch. On the contrary, in transfer learning, the model knowledge (e.g., features and weights) can be transferred from a previously learned task to a new learning task.

3.1.1 Data prepossessing and feature extraction techniques

In SHM applications, the damage identification process is based on comparing the collected data from the structure without damage (base-line) with its current status to determine if there are any occurrences of changes such as damage. Accordingly, signal processing techniques must be applied to the collected data to identify components of interest in a registered signal from a structure. In general, the process of extracting features of the defects that occurred in structures can be achieved in different domains: time domain, frequency domain, time-frequency domain, impedance domain, and modal analysis domain [97].

In this section, various methods for signal processing, data prepossessing and feature extraction are presented.

Fourier Transform

The Fourier Transform (TF) is considered a conventional method for signal analysis. It is used to decompose the registered time-domain signal into its frequency components. Then, the signal can be analysed for its frequency components because the FT coefficients of the transformed function demonstrate the contribution of the sine and cosine functions at each frequency. FT presents global information about the frequency content; therefore, it is suited for signals with stationary frequency content, meaning their frequency content does not change with time [98]. Alternatively, there are other time-frequency representations (TFR) that can identify the local frequency content and are better suited for non-stationary-frequency signals [98]. The Short-time Fourier transform (STFT) is considered the simplest example of a TER, in which the STFT divides the signal into a number of short overlapping segments in the time domain. Each segment is multiplied in time using a fixed modulation window and the FT is used on the resulting signal [98].

Wavelet Transform

The Wavelet Transform (WT) is a mathematical function for data preprocessing that enhances the process of feature extraction in a wide range of applications such as civil engineering, power engineering, traffic engineering, mechanical systems, and aerospace engineering. Furthermore, WT is considered one of the most widely used tools for

signal preprocessing in SHM in recent years [99]. The principal idea of WT is to split data signals into different scale components, accordingly, analysing each component with a resolution matched to its scale [100]. The WT is based on dilated scales and shifted windows that can perform a time-frequency resolution of a data signal. WT is represented in the following Eqn. (3.1), which yields a 2D coefficients matrix $WT\{x\}(a,b)$:

$$WT\{x\}(a,b) = \int_R \Psi_{a,b}(t)x(t)dt, \tag{3.1}$$

$\Psi_{a,b}$ is defined as the mother wavelet which scales and dilates wavelets, where a and b are the scales and dilation parameters. Scaling in WT indicates stretching or compressing it in the time domain. Therefore, compressed wavelets are represented by smaller scales while stretched wavelets can be produced by larger scales [100].

Principal component analysis

PCA is a popular method used for damage identification in SHM. Further, PCA shows a solid and efficient performance in feature extraction and structural damage detection [101–103]. Besides, PCA proves to be an effective tool to improve the training efficiency and enhance the classification accuracy for other ML algorithms, such as unsupervised learning methods [104–106].

PCA is a dimensionality reduction technique utilised to reduce the dimensionality of large data (input space) into a lower dimension (feature space) through transforming a large set of variables into a smaller one with minimal loss information [107]. Moreover, PCA can be used for damage detection by eliminating noise and obtaining sensitive features of damage as eigenvectors. The PCA technique is illustrated below. In the beginning, a matrix $U(t)$ is constructed as shown in Eqn. (3.2), which contains all registered data with time histories:

$$U(t) = \begin{bmatrix} u_1(t1) & u_2(t1) & \dots & u_M(t1) \\ u_1(t2) & u_2(t2) & \dots & u_M(t2) \\ \vdots & \vdots & \ddots & \vdots \\ u_1(t_N) & u_2(t_N) & \dots & u_M(t_N) \end{bmatrix} . \tag{3.2}$$

where t corresponds to the time, u_i $(i = 1, 2, ..., M)$ represents the response from the $i-th$ sensor installed in the monitored structure, M represents the total number of sensors, t_j $(j = 1, 2, ..., N)$ represents the $j-th$ time step of the data, and N is the total time observations during monitoring. Additionally, each column represents the data registration of one sensor. The next step is to normalise the time series of each sensor data registration by subtracting the mean value shown in Eqn. (3.3):

$$\bar{u_i} = \frac{1}{N}\sum_{j=1}^{N} u_i(t_j) \ . \tag{3.3}$$

Equation (3.4) represents the normalised matrix:

$$U'(t) = \begin{bmatrix} u_1(t1) - \bar{u_1} & u_2(t1) - \bar{u_2} & \dots & u_M(t1) - \bar{u_M} \\ u_1(t2) - \bar{u_1} & u_2(t2) - \bar{u_2} & \dots & u_M(t2) - \bar{u_M} \\ \vdots & \vdots & \ddots & \vdots \\ u_1(t_N) - \bar{u_1} & u_2(t_N) - \bar{u_2} & \dots & u_M(t_N) - \bar{u_M} \end{bmatrix} \tag{3.4}$$

After computing the normalised matrix, the covariance matrix is computed as shown in Eqn. (3.5):

$$C = \frac{1}{M} U'^T U' \ . \tag{3.5}$$

Next, the eigenvalue and the corresponding eigenvector of the covariance matrix are computed through solving the following Eqn. 3.6:

$$(C - \lambda_i I)\psi_i = 0 \ . \tag{3.6}$$

where I represents the $M \times M$ identity matrix, $\psi_i = [\psi_{i,1}, \psi_{i,2}, \dots, \psi_{i,j}]^T$ in which $\psi_{i,j} (j = 1, 2, \dots, M)$ is the element related to the $j - th$ sensor. Usually, eigenvalues are sorted into decreasing order, particularly $\lambda_1 > \lambda_2 > \dots > \lambda_M$. Then, the first eigenvector ψ_1 corresponding to λ_1 holds the greatest variance and consequently holds the most important information for the original matrix U. The first few principal components hold most of the variance, whereas the remaining less important components involve the measurement of noise. Accordingly, the first few eigenvectors are utilised as sensitive features for damage detection and localisation.

Auto-associative Neural Networks

Auto-associative Neural Network (AANN), which is also called an autoencoder, is considered as one of the ANN architectures. Generally, AANN is composed of five layers as shown in the Fig. 3.4, which includes the input layer, mapping layer, bottleneck layer (has fewer neurons than the input and the output layers), demapping layer, and the output layer. AANN is considered an unsupervised learning technique. The idea behind AANN is to map the input using nonlinear functions and then reconstruct it using nonlinear functions so the network can learn from the inputs themselves.

Originally, the AANN technique was based on nonlinear principal component analysis (NLPCA), which is a powerful statistical technique used in the process of feature extraction and data dimensionality reduction [108]. The difference between the PCA and NLPCA is that NLPCA is the utilisation of nonlinear functions for mapping the input data as shown in Eqn 3.7.

$$T = G(X). \tag{3.7}$$

As mentioned previously, T is the score matrix, X is the input data of size $(m \times n)$ where m represents the number of variables and n represents the number of observations,

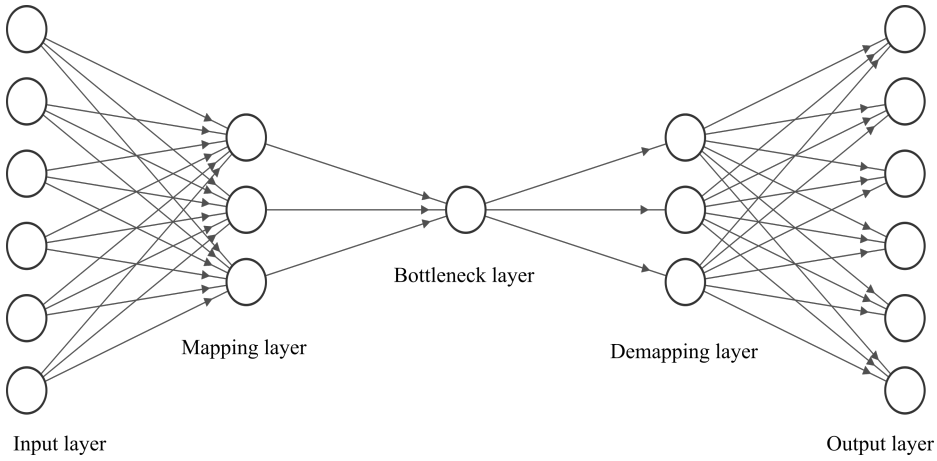

Figure 3.4: Auto-associative Neural Network architecture.

and G is a nonlinear vector function that holds several individual nonlinear functions. Accordingly, the de-mapping process is performed by the inverse of the Eqn (3.7) using a nonlinear function H as shown in Eqn (3.8). The loss of information that occurred due to the mapping and de-mapping process can be calculated in the reconstruction error matrix as shown in Eqn (3.9) [108].

$$\hat{X} = H(T) \tag{3.8}$$

$$E = X - \hat{X} \tag{3.9}$$

Mahalanobis squared distance

MSD is an effective multivariate distance measuring technique in which it measures the distance between a point and a distribution. Therefore, MSD is utilised with multivariate statistics for outlier detection [109]. Assuming X to be training set with data acquired when the undamaged structure is under environmental and/or operational variations (EOVs) with multivariate mean vector μ and covariance matrix Σ [110]. Accordingly, the damage index (DI_i) between feature vectors from the training set X and any new feature vector from the test matrix Z is calculated using Eqn. (3.10):

$$DI_i = (z_i - \mu)\Sigma^{-1}(z_i - \mu)^T, \tag{3.10}$$

where z_i is a tested feature vector. The performance of this technique mainly relies on acquiring all likely EOVs in the training set [110].

Gaussian mixture models

Gaussian mixture models (GMM) are a clustering method commonly used with unsupervised learning, in which it aims to find main clusters of points in a dataset that share

some common characteristics or features. Additionally, GMM has also been referred to as Expectation-Maximization (EM) clustering and is based on the optimization strategy. The damage detection is performed based on multiple MSD-based algorithms, in which the covariance matrices and mean vectors are functions of the main components. A GMM is defined as a superposition of K Gaussian distributions as shown in Eqn. (3.11):

$$p(x) = \sum_{k=1}^{K} P(k)\mathcal{N}(x|\mu_k, \Sigma_k), \tag{3.11}$$

where x represents the training samples in the dataset, and $P(k)$ corresponds to the mixture proportion (contribution weight) of the $k-$th distribution, in which the mixture proportion must satisfy $0 \leq P(x) \leq 1$. The sum of all mixture proportions satisfies the following Eqn. (3.12):

$$\sum_{k=1}^{K} P(x) = 1. \tag{3.12}$$

$\mathcal{N}(x|\mu_k, \Sigma_k)$ refers to the conditional probability of the instance x for the $k-$th Gaussian distribution $\mathcal{N}(\mu_k, \Sigma_k)$ presented in Eqn. 3.13:

$$\mathcal{N}(x|\mu_k, \Sigma_k) = \frac{\exp(-\frac{1}{2}(x-\mu_k)^T\Sigma_k^{-1}(x-\mu_k))}{(2\pi)^{\frac{d}{2}}\sqrt{\det(\Sigma_k)}}, \tag{3.13}$$

where μ_k and Σ_k are the mean and the covariance of that Gaussian distribution, respectively. The complete GMM is parameterized by the mean vectors, covariance matrices and the mixture weights from all component densities $\{\mu_k, \Sigma_k, P(x)\}_{k=1,\ldots,K}$.

The parameters can be carried out from the training data using the classical maximum likelihood estimator (CMLE) based on the EM algorithm [111]. Damage can be detected through estimating k DIs for each data sample x as shown in Eqn. (3.14):

$$DI_q(x) = (x-\mu_k)\Sigma_k^{-1}(x-\mu_k)^T, \tag{3.14}$$

where μ_k and Σ_k refers to all observations from the k data component. For each observation the DI is given by the smallest DI estimated on each component as in Eqn. (3.15):

$$DI(x) = \min[DI_k(x)], \tag{3.15}$$

3.1.2 Classification techniques

In this section, various classification techniques utilised in classifying the extracted features are presented.

Support vector machine

Support vector machine (SVM) is a supervised ML model that is utilised as a classification and regression tool. The idea behind SVM is to find an optimal hyperplane (e.g separate line) in N-dimensional space (N is the number of features) that separates the classes. Furthermore, the hyperplane aims to maximize the margin between the points on either side, hence the so-called "decision line/boundary". Also, when we try to separate two classes of data points, we could have many possible hyperplanes. However, our goal is to find the hyperplane that has the maximum margin (i.e., the maximum distance between data points of both classes). Figure 3.5 shows SVM hyperplanes in 2D feature space and 3D feature space.

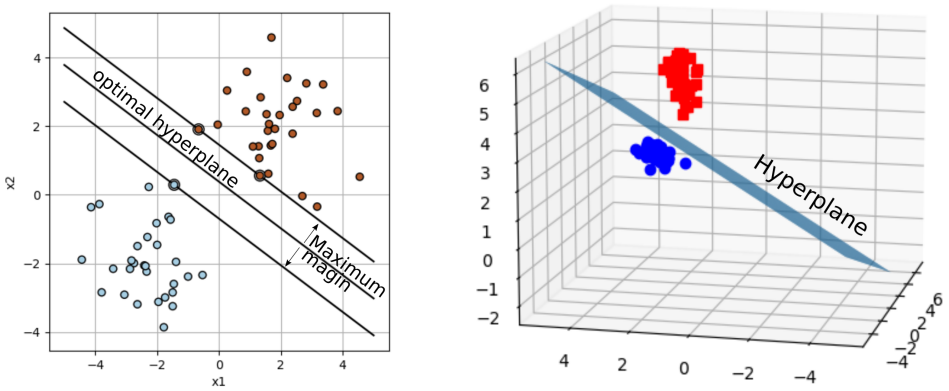

(a) Hyperplane 2D feature space. (b) Hyperplane 3D feature space.

Figure 3.5: SVM for 2D and 3D feature space.

K-Nearest Neighbor

K-Nearest Neighbor (KNN) is a supervised ML technique utilized to perform classification tasks. KNN does not have a specialized training phase. It saves all the training data and uses the entire training set for classifying a new data point, which adds time complexity at the testing time. Moreover, KNN is a non-parametric learning algorithm, which means it does not make any assumptions regarding the input data, which is useful considering the real-world data does not obey the typical theoretical assumptions such as linear separability, and uniform distribution, among others.

In the KNN technique, first, the distance between the new data point and the other data points is calculated. Furthermore, any distance method can be applied, e.g., Euclidean, Manhattan, etc. Accordingly, it picks the K-nearest points, where K is an integer number (number of neighbours) that can be chosen in such a way that the model will be able to predict new unseen data accurately. Then, it assigns the new

data point to the class to which the majority of the K data points belong. Figure 3.6a shows initial data points (training set) before classification, and Fig. 3.6b shows the result of applying KNN techniques to the data points (3 classes) assuming $K = 6$.

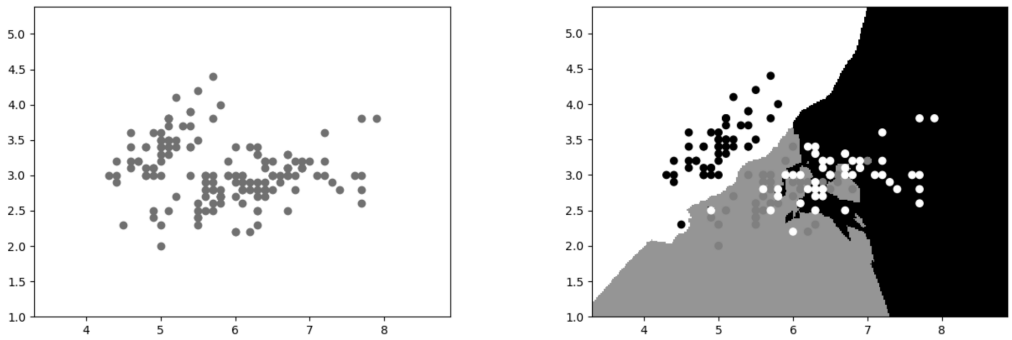

(a) Data points.

(b) 3-Classes with $K = 6$.

Figure 3.6: KNN algorithm: data classification with $K = 6$.

Decision tree

Decision trees are supervised ML algorithms that are used in applications for classification and regression. Additionally, decision trees are considered the basis for many other ML techniques, such as random forests, bagging, and boosted decision trees. The idea of a decision tree is to represent the whole data as a tree where each internal node represents a test on an attribute (a decision rule), and each branch represents an outcome of the test; finally, each leaf node (terminal node) holds the label of the class.

Decision tree can be divided into two categories:

1. Categorical variable decision trees: which includes categorical target variables that are divided into categories. A category means that the decision falls into one of the categories and there is no in-between such as (Yes/No category).

2. Continuous variable decision trees: which has a continuous target variable that can be predicted based on available information (e.g. crack length).

Figure 3.7 presents a typical decision tree. Any decision tree has a root node where data input is carried through. Furthermore, the root node is split into sets of decision rules that result either in a leaf node, which is a non-splitting node, or in another decision rule, creating what is so-called a branch or sub-tree. In cases where there are decision rules that can be eliminated from the tree, a process called "pruning" is applied to minimize the complexity of the algorithm.

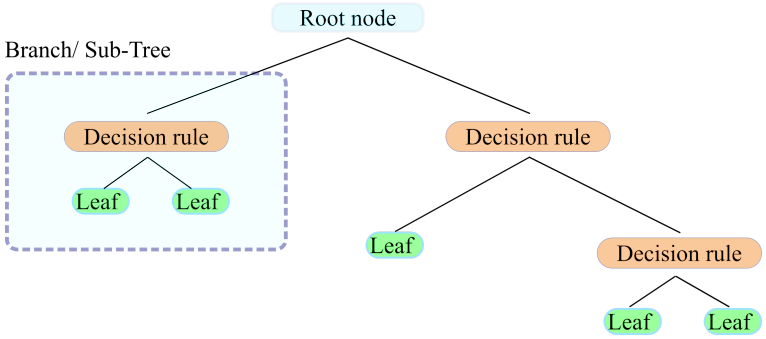

Figure 3.7: Decision tree.

3.2 Deep Learning approach

Deep Learning (DL) is a subfield of machine learning. DL was developed as a solution to the problem of feature engineering extraction, which necessitates a high level of experience and talent to extract damage-sensitive features for specific SHM applications. DL is a type of representation learning that recognizes the appropriate data representations for models like classification and detection.

It can be said that DL techniques have progressed rapidly in recent years as a result of significant advancements in computational power (e.g., central processing units (CPU), graphical processing units (GPU), etc.), as well as the availability of big data and the development of new learning algorithms [112]. As a result, DL-based SHM methods have been used to address difficulties with ML-based SHM.

DL was first motivated by the way the human brain learns. It has a large number of neurons that are densely connected to build a hierarchical structure capable of receiving data from the visual cortex, which can recognise the distinct shapes of edges of an object. These learned patterns are then transferred to a brain area capable of detecting more complex patterns.

DL is a type of hierarchical learning [96] in which non-linear functions are used to extract data representations from raw input data [113]. The collected representation data has simple learnable extracted characteristics at the shallowest layers. As you progress deeper into the stages, those extracted features become increasingly complicated, learnable features.

3.2.1 Multilayer Perceptrons

The simplest DL networks are called multilayer perceptrons (MLP), which are constructed from a group of multiple layers of perceptrons (artificial neurons). Hence, the term

"deep" comes from multiple layers. A perceptron has several inputs and outputs, which have weighted connections with a nonlinear activation function. By performing this operation, a non-linearity is injected into the network, which is important for the learning process. Therefore, if the non-linearity is not considered, no matter how many layers are in the network, it will act like a single-layer neuron. Because by just linearly adding these layers, it will produce another linear output. As a result, a neuron can not update its weights, resulting in no learning. Artificial neuron structure is presented in Fig. 3.8. There are several non-linear functions used in artificial neural networks, such

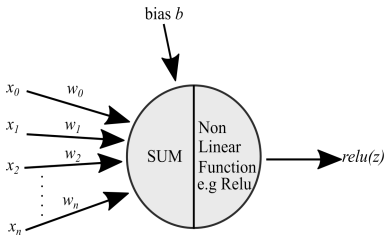

Figure 3.8: Structure of Perceptron.

as the Rectified Linear Unit (Relu), which is commonly used, as shown in Eqn (3.16):

$$Relu(z) = \begin{cases} 0, & \text{if } z < 0 \\ z, & \text{otherwise} \end{cases}, \tag{3.16}$$

Other non-linear functions are the Sigmoid logistic function as shown in Eqn (3.17):

$$\sigma(z) = \frac{1}{1 + e^{-z}}, \tag{3.17}$$

And hyperbolic tangent function tanh as shown in Eqn (3.18) [113]:

$$\tanh(z) = \frac{e^{z} - e^{-z}}{e^{z} + e^{-z}}, \tag{3.18}$$

where z is the summation of adjustable weights $\{w_0, w_1, \ldots, w_n\}$ multiplied by input variables (from previous layer) $\{x_0, x_1, \ldots, x_n\}$ and a bias b as shown in Eqn (3.19):

$$z = \sum_{i=0}^{n} w_i \times x_i + b, \tag{3.19}$$

Supervised learning is the traditional approach to learning in which a neural network builds its knowledge from a given labelled dataset, where the ground truth output is known previously [113].

Optimization and Deep Learning

MLP models learn to find the desired output by updating the network parameters such as weights and biases. Accordingly, a model does a comparison between the calculated

output (predicted) and the ground truth output (target). For this purpose, an objective function (cost function) is applied to estimate the loss (error) between the predicted output and the target. Accordingly, this process needs to be optimized to minimize the estimated value of the loss. A well-known optimization algorithm utilised in DL is the gradient descent (GD) [113]. Fig. 3.9 illustrates the concept of GD in one dimension, in which weights $\{w_0, w_1, \ldots, w_n\}$ are initially assigned randomly. GD aims to reduce the cost function $J(w)$ at each step to reach the $J_{min}(w)$ (global minimum) by calculating the gradient, which represents the slope of the cost function. Accordingly, the weights

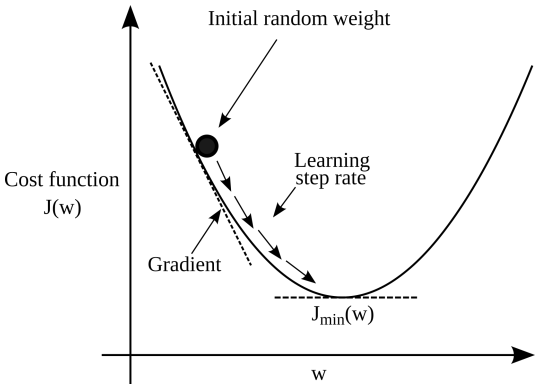

Figure 3.9: The process of Gradient Descent.

are modified as shown in Eqn. (3.20):

$$w_{i+1} = w_i - \alpha \frac{\partial J(w)}{\partial w_i}, \tag{3.20}$$

where the partial derivative $\frac{\partial J(w)}{\partial w_i}$ is the gradient, and α is the learning rate, which is the amount that the weights are updated during the learning process [79]. Therefore, the learning rate monitors the rate at which the neural network learns. Hence, small learning rates require more training time because of the small changes made to the weights when updated, whereas large learning rates result in accelerated changes, consequently, require less training time:

The backpropagation algorithm is the most widely used learning algorithm for neural networks, in which it back propagates the calculated gradients across all the perceptrons. Accordingly, all weights and biases are updated, which leads to minimizing the loss value.

Optimization Challenges in Deep Learning

The optimization algorithm in DL aims to reach the global minimum value of the cost function $J(w)$. However, some challenges during the training process may occur. The

most tricky challenges are the local minima, saddle points, vanishing gradients, and exploding gradients.

The local minima occur during training when the optimization algorithm ends up with a value of the cost function $J(w)$ that is smaller than values of $J(w)$ at any other points in the local neighborhood of w. Figure 3.10 shows that during the optimization process, it is possible to end up in local minima.

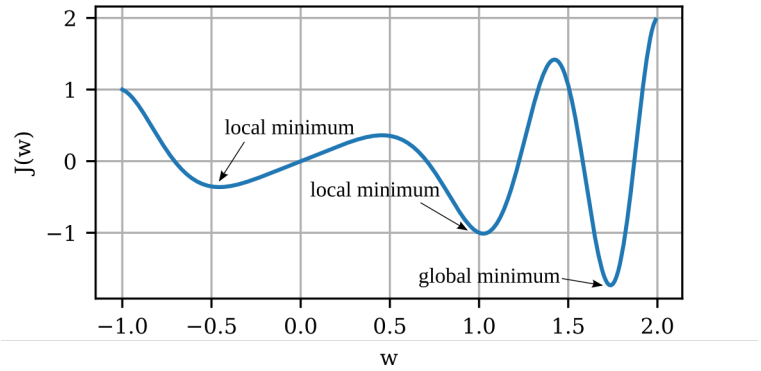

Figure 3.10: Local minima.

A saddle point is any location where all gradients of a cost function vanish but is neither a global nor a local minimum, as shown in Fig. 3.11.

The vanishing gradients are the most encountered problem during the optimization process, as the gradients become too small, causing the learning process to get stuck for a long time before it makes any progress or stops at all [114]. On the other hand, the exploding gradients problem occurs when the gradients become so large that they lead to numerical overflow and result in "NaN" values [114].

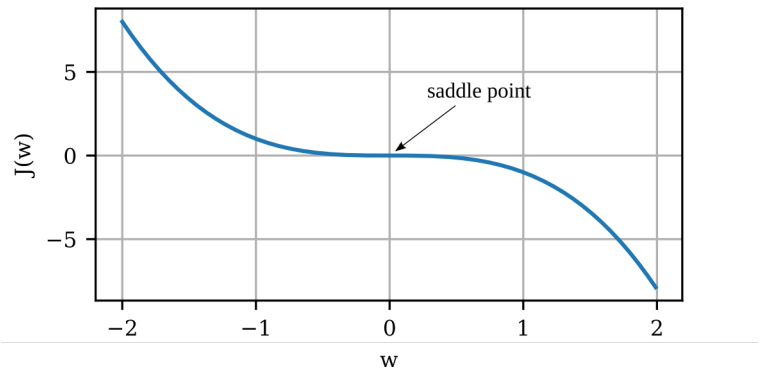

Figure 3.11: Saddle point.

3.2.2 Convolutional Neural Network

Convolutional Neural Network (CNN) is a special type of artificial neural network (ANN) that was initially developed in the 1980s by Fukushima [115] who was inspired by the discoveries of Hubel and Wiesel regarding the cat's visual cortex. CNN is one of the most utilised architectures in DL for image processing as they can recognise complex patterns of images by performing convolution operations.

In mathematics, a convolution is an operation performed between any two functions, as for example $f, g : \mathbb{R}^d \to \mathbb{R}$ to produce a third function $(f * g)$ depicted in Eqn. (3.21):

$$(f * g)(x) = \int f(z)g(x - z)dz \tag{3.21}$$

In which, we measure the overlap between f and g, as one function is flipped and shifted by x.

In the case of discrete objects defined on the set $\mathbb{Z}$ of integers, the integral operation turns into a summation of elementwise multiplied components, as depicted in Eqn. (3.22):

$$(f * g)(x) = \sum_a f(a)g(i - a) \tag{3.22}$$

For inputs with two dimensions, we have a corresponding sum with indices (a, b) for f and $(i - a, j - b)$ for y respectively as depicted in Eqn. 3.23 that describes a cross correlation operation:

$$(f * g)(i, j) = \sum_a \sum_b f(a, b)g(i - a, j - b) \tag{3.23}$$

The convolution operation for image processing is essentially a cross-correlation operation, also known as a sliding dot product or sliding inner-product. CNN was designed to process data as tensors with different dimensions. For a 1D data tensor, it can represent various data forms, such as signals and sequences, in addition to sentences in various languages in translation problems. For a 2D data tensor, it can represent an image in grayscale (one channel). Furthermore, by combining three 2D tensors, a coloured 3D image is produced due to the different intensities of the pixels in the (RGB) channels. A 4D tensor represents volumetric data, such as a sequence of 3D images or a video.

A convolutional layer has a number n of convolution kernels (filters), in which each kernel has a set of weights of a size (w_k, h_k, d_k). The kernel slides over an input image of a size (w, h, d) performing a convolution operation (dot product), where w and h represent the image width and height, respectively, while d represents the depth (number of channels). The outputs of the convolution operation are feature maps that

are locally connected to the outputs of the previous layer. Figure 3.12 illustrates the convolution operation for a 3D input and the calculated output (feature map) with a new shape of $(h_n \times w_n \times d_n)$.

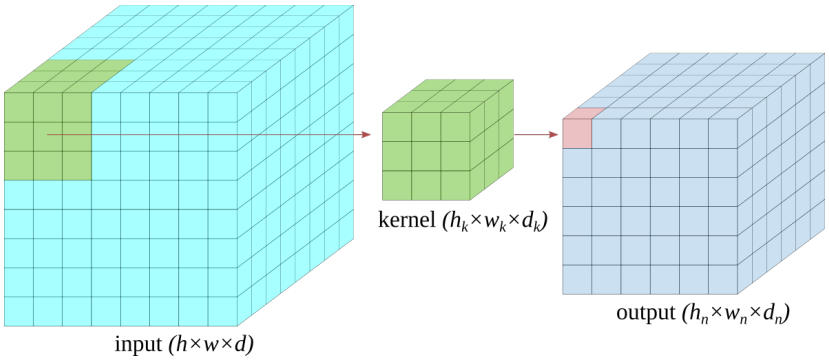

Figure 3.12: Convolution operation with a sliding kernel.

Typically, the feature map size diminishes due to the convolution operation, though, the feature map can keep the same size of the input by applying some padding over the input. The calculations of new height and width of the output are illustrated in Eqns (3.24) and (3.25):

$$h_n = \frac{h + 2 \times p - h_k}{s} + 1, \tag{3.24}$$

$$w_n = \frac{w + 2 \times p - w_k}{s} + 1, \tag{3.25}$$

where h_n and w_n are the new height and width dimensions of the feature map, respectively, after applying the convolution. The padding p is added to the input image of a feature map to guarantee that both the input and the output have the same dimensions. h_k and w_k represent the height and the width of the convolutional kernel, respectively. The stride s defines how much the convolutional kernel slides each step during convolution. The number of channels at the output feature map (d_n) equals the applied number of convolutional kernels (n).

Typically, when we train a CNN model, its kernel weights are initialised randomly. Accordingly, during the backpropagation process, all learnable parameters (kernel weights) are updated. Consequently, kernels learn to detect different types of edges (vertical, horizontal, and diagonal edges), colour intensities, etc.

Commonly, a convolutional operation is followed by a non-linear activation function such as (ReLU, sigmoid, tanh), followed by a downsampling operation (pooling). The idea behind the pooling operation is to aggregate related features into one by reducing the spatial dimensions of the feature maps (e.g., width, height, and depth) [113], which reduces the computation complexity. Figure 3.13 presents the downsampling operations

that max and average pooling. Furthermore, the pool size is 2×2 with strides of 2. The Maxpool picks the maximum value in the local pool filter in a feature map, whereas the average pool picks the average value in the local pool filter in a feature map. A

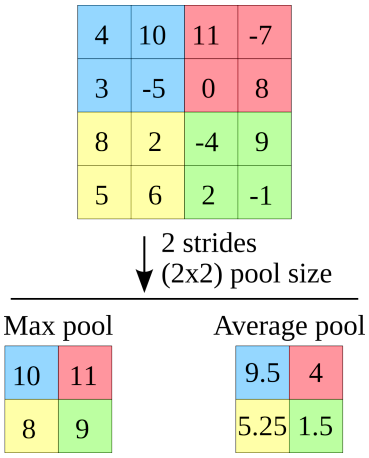

Figure 3.13: Types of downsampling operations.

convolution operation, followed by a non-linear activation function, and pooling, is referred to as a convolutional block. Moreover, a convolutional block can be stacked and repeated several times. Finally, to pass the output from the convolutional block to the dense layer, a flattened layer is utilised to produce a 1D tensor. Figure 3.14 presents the default architecture of a CNN.

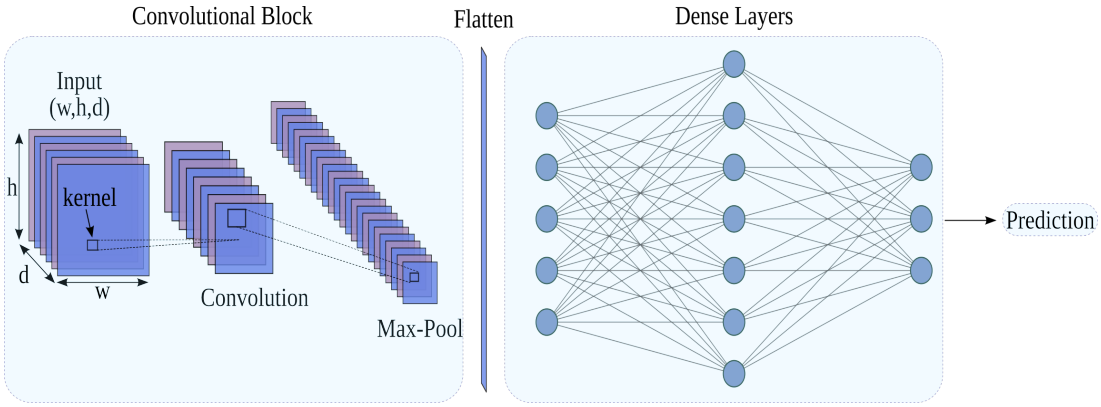

Figure 3.14: Convolutional Neural Network architecture.

CNN became popular after the competition of the "Large Scale Visual Recognition Challenge 2012 (ILSVRC2012)", when Krizhevsky et al. [116] introduced Krizhevsky et al. [116], which is a deep CNN applied to a large dataset of $1,000,000$ images and $1,000$ different classes. The AlexNet results were magnificent. This success has stimulated the progress of the development of GPU technology and the use of the non-linear activation function Relu [113]. In the next few years, several spectacular CNN

architectures were presented (e.g., VGG-16, ResNet, Inception-v4, and others).

3.2.3 Recurrent neural networks

Recurrent neural networks (RNN) are a class of ANN that was introduced to work with time-series data (sequential data). The RNN technique can remember its data input because of its internal memory, which makes it a powerful and promising technique in the field of DL. Since there are temporal problems such as natural language processing, language translation, image captioning, and so on, they require to be handled sequentially. In the traditional deep neural networks (feed-forward), information only moves in one direction from the input layer through hidden layers to the output layers. However, this is not the case for the RNN technique, which implies the current output of an RNN depends on the prior input sequence. Accordingly, future events are also used to predict the output of a given sequence. Figure 3.15 depicts the difference between RNN and feed-forward deep neural networks. As shown in Fig. 3.15a, for the RNN, the output of a certain layer is looped back to its input, which helps in making the prediction. However, in feed-forward networks shown in Fig. 3.15b, the inputs and outputs are independent, as there is only one direction for the data to move.

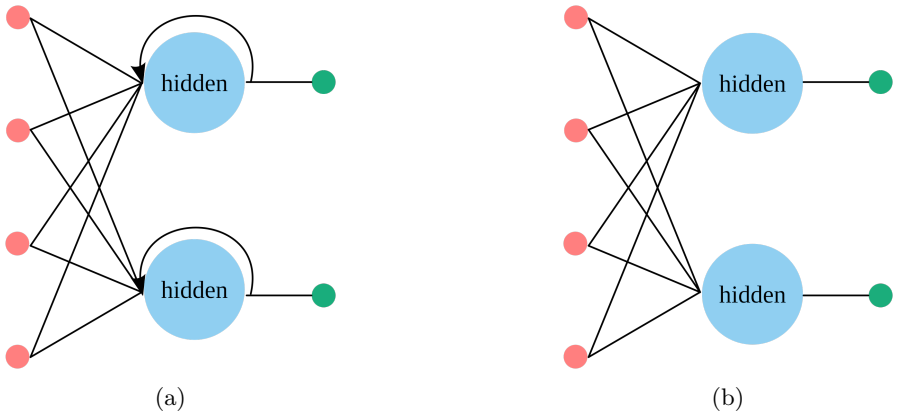

Figure 3.15: (a) RNN v.s. (b) Feed-forward neural network.

Figure 3.16 presents a visualisation of an unrolled RNN, where x_t corresponds to the sequential timestamped input at time t, h_t corresponds to the internal state and Y_t corresponds to the predicted timestamped output at time t. An unrolled RNN can be seen as a cascading sequence of feed-forward networks.

In feed-forward neural networks, the learnable parameters (adjustable weights) are available only for the forward path of data propagation and are updated through the back-propagation algorithm. In RNNs, there are two paths of data propagation (forward and backwards). Hence, there are learnable weights for both directions.

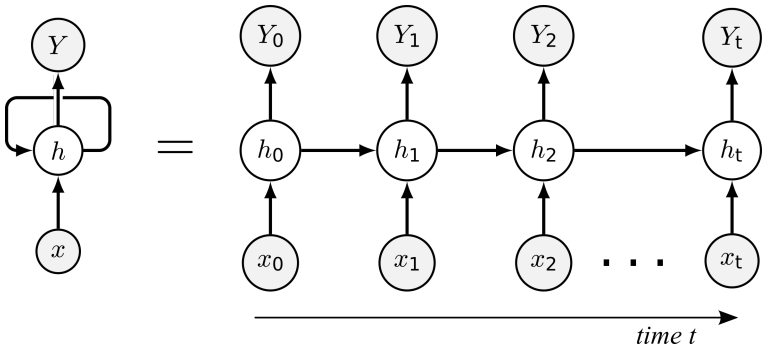

Figure 3.16: Unrolled RNN.

Further, weights are updated using back-propagation through time (BBTT) [117]. BBTT depends on the number of timestamps, so it is computationally expensive when there are a high number of timestamps as BBTT performs a back-propagation algorithm on unrolled RNN. Consequently, when implementing RNNs, issues may arise during updating the learnable weights using BBTT, which are vanishing and exploding gradients. To overcome such issues, Hochreiter et al. [118] introduced a long-term memory (LSTM), which is a memory extension for a regular RNN to address the problem of long-term dependencies. Further, LSTMs handle inputs or outputs of any length, which makes LSTMs powerful for solving very complex sequential problems. LSTM is composed of four units: an input gate, a cell state, a forget gate, and an output gate as presented in Fig. 3.17. These gates help regulate the flow of information, which is added to or removed from the cell state. The hidden states in LSTM hold the short-term memory while the cell state holds the long-term memory.

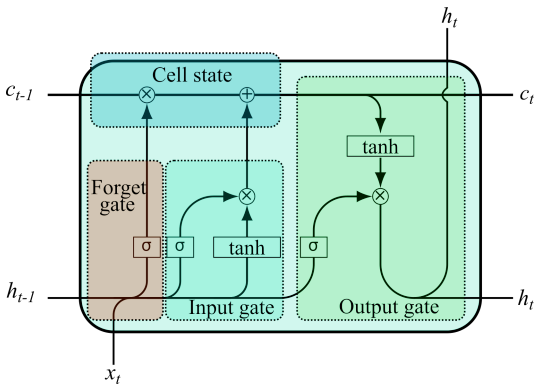

Figure 3.17: LSTM architecture.

The purpose of the forget gate is to determine which information to consider and which to neglect. The current input x_t and the previous hidden state h_{t-1} are passed through a sigmoid function which will produce values between 0 and 1. Then the outputs of

the sigmoid are multiplied with the previous cell state c_{t-1} to discard outputs equal to zero. Equation (3.26) depicts the calculation at the forget gate:

$$f_t = \sigma(W_f.[h_{t-1}, X_t] + b_f), \tag{3.26}$$

where W represents the learnable weights, and b represents the bias term.

The input gate i_t takes the current input X_t with the previous hidden state h_{t-1} and applies the sigmoid function to get values in a range between 0 (not important) and 1 (important), then the same current input X_t, and the hidden state h_{t-1} are passed through a tanh function at $\tilde{C}_t$ that will regulate the network by transferring the values into a range between -1 and 1. Then, the outputs from the sigmoid and tanh functions are multiplied point-by-point to eliminate 0 values. Equation (3.27) depicts the calculation at the input gate:

$$\begin{aligned} i_t &= \sigma\left(W_i \cdot [h_{t-1}, X_t] + b_i\right), \\ \tilde{C}_t &= \tanh\left(W_s \cdot [h_{t-1}, X_t] + b_c\right). \end{aligned} \tag{3.27}$$

At this point, the network has sufficient information obtained from the input and forget gates. Hence, the current cell state C_t is calculated by multiplying the previous cell state C_{t-1} with the output of the forget gate, and then the result is added to the calculated input values as depicted in Eqn. (3.28):

$$C_t = f_t * C_{t-1} + i_t * \tilde{C}_t. \tag{3.28}$$

The output gate o_t computes the next hidden state h_t which is holds information related to the current inputs. Accordingly, the current input X_t and the previous hidden state h_{t-1} are passed through a third sigmoid function to produce values between 0 and 1. The current cell state C_t is passed through a tanh function and multiplied point-by-point with o_t to produce the new hidden state h_t which is transferred to the next timestamp. Equation (3.29) illustrates the calculations at the output gate:

$$\begin{aligned} o_t &= \sigma\left(W_o\left[h_{t-1}, X_t\right] + b_o\right), \\ h_t &= o_t * \tanh\left(C_t\right). \end{aligned} \tag{3.29}$$

Recently, LSTMs have been widely used for large-scale learning of language translation models, speech recognition systems, chatbots, forecasting stock markets, text data analysis, and many more [119, 120]. However, LSTMs are inefficient in capturing spatial information by themselves when the time series inputs are consecutive images. Accordingly, the ConvLSTM layer, which is a combination of CNN and LSTM units, was introduced by Shi et al. [121] to solve such a problem. For ConvLSTM, the convolution operations are applied both at the input-to-state transition and at the

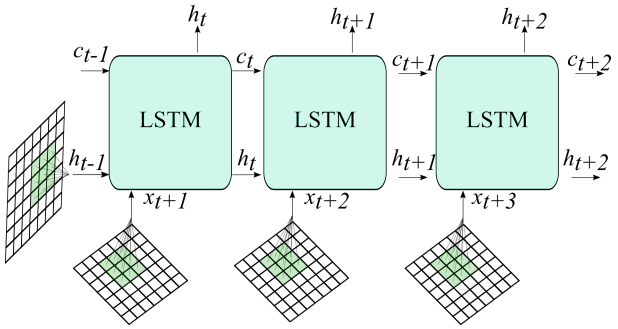

Figure 3.18: ConvLSTM architecture.

state-to-state transitions. ConvLSTM, shown in Fig. 3.18 is a variation of the LSTM cell as it performs a convolution operation within the LSTM cell. ConvLSTM is a combination of a convolution operation and an LSTM cell. Thus, ConvLSTM can capture the time-correlated and spatial features in a series of consecutive images. Equation (3.30) depicts the ConvLSTM operations as the inputs $X_1, \ldots, X_t$, hidden states $h_1, \ldots, h_t$, cell states $C_1, \ldots, C_t$ and input, forget, and output gates are represented as i_t, f_t, and o_t, respectively:

$$\begin{aligned} i_t &= \sigma\left(W_{xi} * X_t + W_{hi} * h_{t-1} + W_{ci} \odot C_{t-1} + b_i\right) \\ f_t &= \sigma\left(W_{xf} * X_t + W_{hf} * h_{t-1} + W_{cf} \odot C_{t-1} + b_f\right) \\ C_t &= f_t \odot C_{t-1} + i_t \odot \tanh\left(W_{xc} * X_t + W_{hc} * h_{t-1} + b_c\right) \\ o_t &= \sigma\left(W_{xo} * X_t + W_{ho} * h_{t-1} + W_{co} \odot C_t + b_o\right) \\ h_t &= o_t \odot \tanh\left(C_t\right) \end{aligned} \tag{3.30}$$

where $*$ indicates the convolution operation, and $\odot$ represents the Hadamard product. Recently, ConvLSTM has become very popular and is increasingly being used in more and more image processing applications.

3.3 Data-driven based SHM/NDT Techniques: Related work

The importance of SHM systems originates from their ability to monitor the condition of structures in real-time. SHM systems can be developed using data-driven methods, which require a huge amount of data that are captured by monitoring the status of a structure.

The process of extracting features from structures in conventional techniques needs a lot of time and experts in the field. Therefore, introducing machine learning methods to the feature extraction process became necessary. Hence, deep learning methods can

generalise and learn new features by themselves, which improves their functionality in damage estimation.

DL approach makes it possible to use registered data in their raw form without any need to perform feature extraction. Hence, such an approach has an end-to-end structure that automatically learns and discovers the hidden features in a high dimensional input data [122, 123]. Figure 3.19 illustrates the main differences between the conventional ML-based SHM and DL-based SHM approaches.

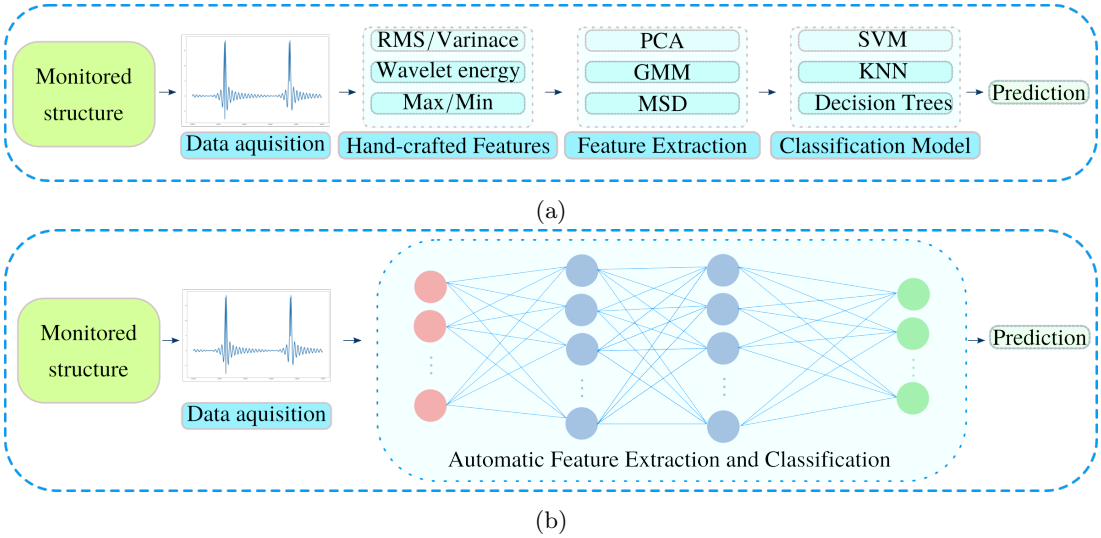

Figure 3.19: (a) Conventional ML based SHM vs. (b) DL based SHM.

Worden et al. [124] have proposed several axioms related to SHM systems implemented using machine learning methods. According to them, damage detection can be performed in unsupervised learning. However, recognising the damage type and how significant it is can not be performed without supervised learning. Moreover, the feature extraction process is essential for damage detection, and it can be performed by analysing and processing the signals captured by the sensors (e.g. PZT actuators), and then converting them to damage information. Therefore, introducing machine learning methods to the feature extraction process became necessary. Hence, machine learning methods can generalise and learn new features by themselves, which improves their functionality in damage estimation.

3.3.1 Machine learning based SHM/NDT

In recent years data-driven methods based on machine learning have increased in a significant way. In the following, I will present some methods for damage detection and estimation based on machine learning techniques.

Das et al. [125] presented a method for estimating several types of defects (delamination,

saw cut, notches, and drilled holes) in composite material. For this purpose, a collection of PZT transducers were attached to the surface of the structure to generate and register Lamb waves propagation. Accordingly, a time-frequency domain was utilised to extract features related to defects from the registered response. Those extracted features were fed to one-class SVM, which performs classification and damage estimation.

Moreover, Dib et al. [126] proposed a novelty classifier based on one-class SVM for detecting damage. The method was conducted by extracting data from damage impact on a glass-fibre composite plate and then evaluating the performance of the classifier. To extract the necessary features from the propagated wave the registered signal was segmented into L time bins, and the Fourier transform was applied to each time bin. Accordingly, the features vector was constructed from the signal phase and the amplitude for each segmented time bin.

Vitola et al. [127] developed a damage detection and classification methodology that was examined on aluminium plates. An array of PZT transducers was placed on the plate surface to sense wave propagation in the structure. The methodology is based on the use of principal component analysis (PCA) and machine learning techniques for recognising patterns. PCA means analysing a large amount of information by finding the principal components. However, the PCA method is not invariant to scaling, thus, data must be normalized [128]. Next, normalised data is fed to several machine learning models for training. For this purpose, several classification algorithms were applied, decision trees, KNN and SVM. However, only a few of these models presented good outputs in damage detection.

Godin et al. [129] applied Acoustic Emission signals (AE) in their approach, which happen due to a sudden release of stored energy when damage occurs. AE signals contain important information about the discriminative features for the damage type such as fibre breakage, de-cohesion of the interface, or a crack in the matrix in composite materials. Authors in this work presented supervised and unsupervised classifiers to recognise different damage patterns through grouping AE signals from the tensile tests of unidirectional glass/polyester composite into several different classes. For clustering AE signals, a K-means algorithm was used. AE signals were clustered based on several metrics such as the AE signal duration, amplitude, rise time, and the number of counts to the peak. Accordingly, the clustered labelled data is fed into a KNN supervised classifier. A trained classifier can classify new coming data accordingly. Regarding the unsupervised classification, the Kohonen classifier was utilised [130], which is a self-organising map (SOM) which is a neural network consisting of neurons as processing units.

Nazarko et al. [131] monitored the axial bolt forces using elastic wave propagation signals. Six-bolt flange connections were put through a series of static tensile tests in the lab. For the accurate measurement of axial force, some bolts were equipped with washer load cells. Additionally, a few bolts were equipped with piezoelectric transducers (actuator and sensor operating in a pitch-catch arrangement) to capture the elastic wave signals. The outcomes of the ultrasonic testing were then integrated with the artificial neural network (ANN) for both signal compression and as a tool for user interface. The outcomes demonstrated that ANNs could predict the axial forces in bolts with a reasonable amount of accuracy. Significant potential exists for actual NDT inspections, according to the suggested method [131].

Pashmforoush et al. [132] proposed a technique to classify damage to various lay-up configurations in glass/polyester composites. For this purpose, the K-means algorithm with the genetic algorithm was utilised. PCA was used to reduce the data dimensionality. Next, a combination of the K-means algorithm with the genetic algorithm is used for clustering the data. The reason for applying the genetic algorithm is to find the optimal number of cluster centres for the KNN algorithm. Parameters of the AE signals such as peak amplitude, frequency, rise time, energy, and duration were estimated for each cluster and utilised as discriminative features. AE signal frequency was found to be a good feature for discrimination. Accordingly, AE signals with the highest frequency were corresponding to fibre breakage, AE signals with the lowest frequency were corresponding to matrix cracking, and the frequencies range in-between were corresponding to the debonding defect.

Nazarko et al. [133] investigated the potential of utilising artificially deteriorated signals of Lamb waves in training a novelty detection (ND) system for early damage detection. To train auto-associative neural networks, the authors used principal components that were generated from signals that were measured experimentally. The measurements of Lamb waves in the investigated specimens made of aluminium and glass fibre reinforced polymer serve as an excellent illustration of how the ND algorithm accurately handles both simple and complex signals. It was also noted that the proposed ND method maintained its sensitivity and robustness when it used raw signals with a relatively low sampling rate, on a relatively narrow time window, and further noised signals.

3.3.2 Deep learning based SHM/NDT

Deep learning techniques have widely been utilised for the inspection and maintenance of civil infrastructure and have shown very promising results [134–141].

Besides the widespread applications of deep learning for SHM/NDT in civil engineering,

deep learning is still less investigated for the purpose of damage detection based on guided waves in composite materials.

Guided waves approaches are widely utilised in SHM/NDT due to the fact it can detect very small damage sizes [142]. Damage detection and localisation approaches using guided waves are based on the measurements of the PZT sensors, whether bonded or embedded into the investigated structure. PZT sensor(s) are responsible for the excitation of the structure by a short ultrasonic pulse (usually, the used frequency is in the range of hundreds of kHz) that propagates through an investigated structure such as plates or pipes as an elastic wave. The registered signals (baseline) are stored and compared with other registered signals acquired through the lifetime of the investigated structure. Damage detection using the baseline subtraction approach for guided waves is based on subtracting damage-free registered measurements from the newly registered measurements to obtain the new changes that occurred to the structure. These changes are considered as damage information. The baseline approach is effective in controlled environments where the variations of the operational/environments (i.e. considerations of multiple sensing modalities, uncertainty in material properties, bounding conditions, etc.) are negligible [112]. Such variations can alter registered data leading to false alarms. The effect of such variations can be reduced through physics-based modeling, which can simulate an undamaged scenario (baseline) for the wave propagation through the investigated structure. Then, the simulated baseline can be used in the subtraction for damage detection. However, in real-world structures, it is difficult to adjust the parameters of the model to match the experimental registered data. Accordingly, data-driven techniques based on ML and DL approaches can be the solution and deliver robust models for many real-life variations.

In the following, methods for damage size estimation based on machine learning and deep learning techniques are presented, which are targeted in the field of SHM/NDT.

Melville et al. [143] proposed a CNN model for the prediction of damage state in thin metal plates to overcome the issue of inaccurate representation of guided wave propagation when applying conventional approaches. The model utilizes the full wavefield scans of thin plates (aluminium). Moreover, the acquired raw data used for training the model was divided into undamaged and damaged states equally. The model achieved higher accuracy regarding damage detection equal 99.98% when compared to SVM which achieved 62%.

Sammons et al. [144] proposed a CNN model based on X-ray computed tomography for delamination estimation in a composite structure. Furthermore, image segmentation was applied to the input images to identify the damage. However, the model was only

able to identify small delaminations.

Moreover, Chetwynd et al. [145] presented a multi-layer perceptron (MLP) network for damage detection in curved composite panels, in which, stiffeners were added to represent the damage. The Authors in this work investigated the propagation of Lamb waves through the panel in which they were generated and registered by a PZT array. Furthermore, for each Lamb wave response, a novelty index was obtained. The index value is compared to some threshold value, in which if the index value exceeds the threshold it implies that there is damage to the structure. Accordingly, the MLP network was fed by obtained novelty indexes, and performed two operations: classification and regression. The classification network was designed to define three convex regions of the panel and then to determine whether the panel is damaged or not. On the other hand, the regression network is capable of estimating the exact location of the damage

Furthermore, De Fenza et al. [146] proposed an artificial neural network (ANN) model for damage detection in plates made of aluminium alloys and composite utilising Lamb waves. Response data of wave propagation were used to calculate damage indexes which were fed into the model as an input. Accordingly, the model performs automatic feature extraction in conjunction with the probability ellipse-based method. The ANN model and probability ellipse (PE) method were applied to identify the damage location. The results from the ANN model and the PE presents how it is useful to apply damage indexes as a baseline for such methods to evaluate damage in aluminium and composite structures. Ewald et al. [147] presented a CNN model called (DeepSHM) for signal classification using Lamb waves. Furthermore, the model provides an end-to-end approach for SHM by utilising response signals captured by sensors. Moreover, response signals were preprocessed by wavelet transform to get the wavelet coefficient matrix (WCM). Further, the CNN model was trained with the WCM to obtain neural weights.

Full wavefield scanning using SLDV is time-consuming, however, simply reducing the number of scanning points will result in low-quality images. Keshmiri Esfandabadi et al. [148] proposed a compressive Sensing technique using ConvNets to enhance the resolution for images captured by SLDV while decreasing the number of measurement scan points down to 10% of the number of the full gird scanning points. Although, the proposed technique enhanced the image resolution, however, there is a side effect, which resembles the fact when enhancing the resolution, the most affected region is the damaged area. Accordingly, the damage features will be altered. On the other hand, this may be an indication of the location of the damage.

Furthermore, Melville et al. [149] proposed a technique for damage detection in thin metal plates (aluminum and steel), using full wavefield data scanned by SLDV. Using this data to train a deep neural network of 4 hidden layers including 2 convolutional layers for features extraction and 2 fully connected layers. The developed model shown good results when compared with traditional machine learning SVM. Moreover, Melville [150] introduced a method for detecting damage in structures based on the k-means algorithm. The method is known as "dictionary learning" which uses full wavefield data collected from thin metal plates. The method was applied to structures with different material types and thicknesses that were not used during training to prove how well the model in damage detection in various conditions. However, their work was not implemented for a further step, which is damage localization and classification.

3.4 Summary

In this chapter, I presented several techniques that had studied and examined guided Lamb waves in composite materials to detect and localise the damage using signal processing techniques. Consequently, it can be concluded that DL methods have had more and more applications in SHM/NDT in recent years. However, these are theoretical implementations rather than practical implementations in the field, which can be evidence of the lack of maturity of these methods. The other conclusion can be that it is observed that signal processing methods based on handcrafted feature extraction have progressed into end-to-end approaches.

Chapter 4

Methodology

In this chapter, several DL methodologies were presented to detect and localise delamination in composite laminates based on non-contact ultrasonic wavefield imaging that can provide precise details about the health status of the investigated specimen. Accordingly, a large synthetic dataset was generated representing the full wavefield of the Lamb waves propagating in a CFRP plate and their interaction with discontinuities such as the delamination and the plate edges, acquired by SLDV from the bottom surface of the plate. The acquisition process of the synthetic dataset is explained in detail in the section 4.1.

The deep learning models were trained using a supervised scheme. Hence, it uses a training set to train the developed models to predict the desired output. The developed methods are end-to-end approaches, in which the whole unprocessed training dataset is fed into the model. Hence, it will learn by itself to identify distinct patterns and detect damage. In section 4.2, a fully connected CNN classifier model for detecting and localising delamination is presented in detail. In section 4.3, I present five FCN models for delamination identification. Further, the developed models were trained using the RMS images in which the developed models are performing pixel-wise image segmentation. In section 4.5, a deep learning model for delamination identification utilising the animation of a full wavefield is presented.

As mentioned earlier, ultrasonic wavefield imaging with SLDV can provide detailed information on the health status of an inspected structure. However, high spatial resolution, which is frequently required for precise damage size estimation, typically demands a prolonged scanning time. In section 4.6, I present a DL model for image super-resolution reconstruction in which the full wavefields of Lamb waves are recovered from low-resolution wavefields acquired with a reduced number of measuring points into high-resolution wavefields. Accordingly, this can allow for a precise recovery of propagating waves and their interactions with discontinuities such as delaminations

and boundaries of the plate. Consequently, this process will speed up the acquisition of data. Furthermore, the reconstructed full wavefield can be used in damage imaging.

All developed models were implemented and trained with the Keras API [151] running on top of TensorFlow [152]. The NVIDIA GeForce RTX 2070 with 8 GBs of memory was utilised to train the CNN classification models. Furthermore, the NVIDIA Tesla V100 GPU with 32 GBs of memory was utilised to train the FCN models, the AE-ConvLSTM model, and the DLSR model. Moreover, training the developed models requires tuning of many hyperparameters such as learning rate, momentum, choice of the optimizer, dropout rate, batch size, and the number of epochs, among others. Accordingly, to obtain satisfactory results, I used the trial and error approach to tune the hyperparameters of the developed models.

4.1 Synthetic dataset acquisition

The essential part of this work was the generation of a synthetic dataset of a full wavefield of propagating Lamb waves in a plate made of CFRP. Therefore, in this work, a numerical dataset of propagating waves in carbon fibre reinforced composite plates was computed by using the parallel implementation of the time domain spectral element method [153].

The dataset resembles the particle velocity measurements at the bottom surface of the plate acquired by the SLDV in the transverse direction as a response to the piezoelectric (PZT) excitation placed at the centre of the plate. The input signal was a five-cycle Hann window modulated sinusoidal tone burst. The carrier frequency was assumed to be 50 kHz. The total wave propagation time was set to 0.75 ms so that the guided wave could propagate to the plate edges and back to the actuator twice. The number of time integration steps was 150000, which was selected for the stability of the central difference scheme.

The material was a typical cross-ply CFRP laminate. The stacking sequence $[0/90]_4$ was used in the model. The properties of a single ply were as follows [GPa]: $C_{11} = 52.55$, $C_{12} = 6.51$, $C_{22} = 51.83, C_{44} = 2.93, C_{55} = 2.92, C_{66} = 3.81$. The assumed mass density was 1522.4 kg/m^3. These properties were selected so that wavefront patterns and wavelengths simulated numerically are similar to the wavefields measured by the SLDV on CFRP specimens used later on for testing the developed methods for delamination identification. The shortest wavelength of the propagating A0 Lamb wave mode was 21.2 mm for numerical simulations and 19.5 mm for experimental measurements, respectively.

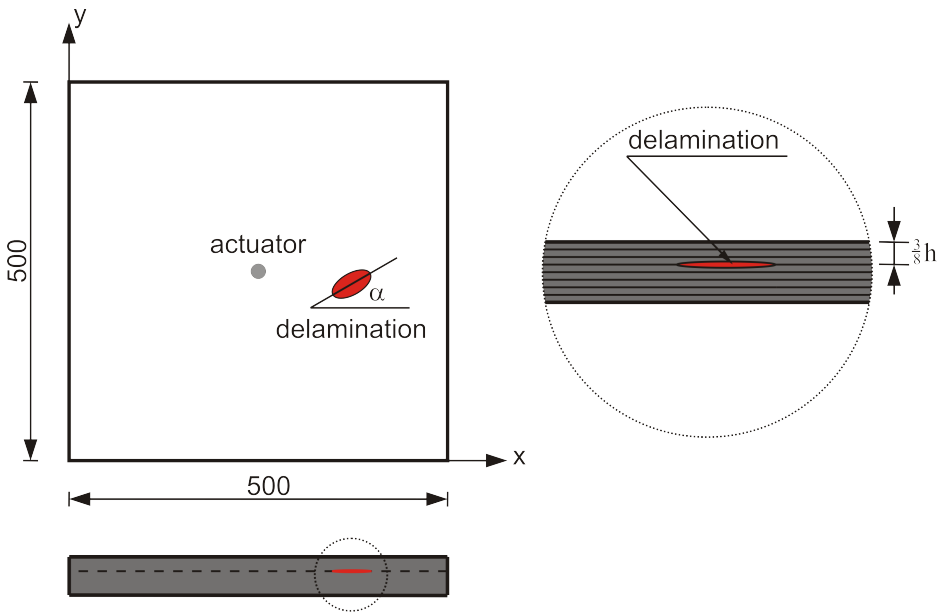

Figure 4.1: Setup for computing Lamb wave interactions with delamination.

For each case, single delamination was modelled by using the method of splitting nodes between appropriate spectral elements. It was assumed that the composite laminate is made of eight layers of a total thickness of 3.9 mm. The delamination was modelled between the third and fourth layer (see Fig. 4.1 for details). It should be noted that Fig. 4.1 shows an exaggerated cross-section through the delamination. Zero-volume delamination was assumed in the model. Delamination spatial location was selected randomly so that the interaction of guided waves with delamination is different for each case. It includes cases when delamination is located in the corner of the plate, which is the most difficult to identify by signal processing methods. Additionally, the size of the delamination of elliptic shape was randomly simulated by selecting the size of the ellipse minor and major axes. Furthermore, the angle between the delamination major axis and the horizontal axis was randomly selected. In summary, the following random parameters were simulated in each case:

- delamination geometrical size (ellipse minor and major axis randomly selected from the interval $[10\,\text{mm}, 40\,\text{mm}]$),
- delamination angle (randomly selected from the interval $[0°, 180°]$),
- coordinates of the centre of delamination (randomly selected from the interval $[0\,\text{mm}, 250\,\text{mm} - \delta]$ and $[250\,\text{mm} + \delta, 500\,\text{mm}]$, where $\delta = 10\,\text{mm}$).

These parameters are defined in Fig. 4.2, which shows exemplary random delamination locations, sizes, and shapes for Lamb wave propagation modelling. It is important to note that the numerical cases include delaminations at the edges and corners of

the plate. It resulted in random spatial placement of delaminations. The plate with

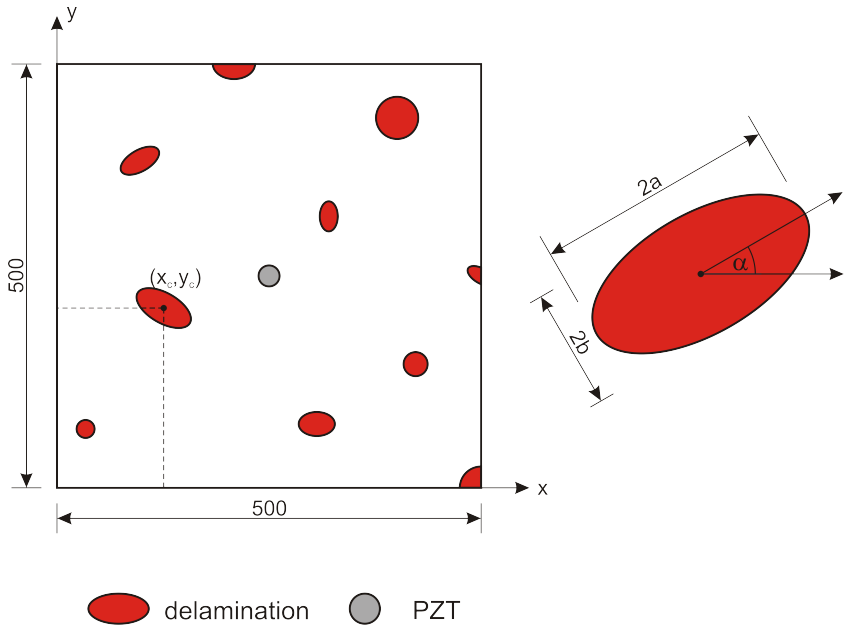

Figure 4.2: Exemplary locations, sizes and shapes of random delaminations used for Lamb wave propagation modeling.

overlayed 475 delamination cases is shown in Fig. 4.3.

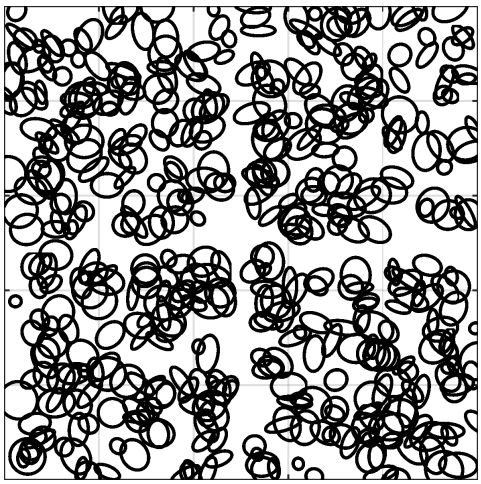

Figure 4.3: The plate with 475 cases of random delaminations.

The output from the top and bottom surfaces of the plate in the form of particle velocities at the nodes of spectral elements were interpolated on the uniform grid of 500×500 points by using shape functions of elements (see [153] for more details). It essentially resembles measurements acquired by SLDV in the transverse direction (perpendicular to the plate surface).

An example of the simulated full wavefield data on the top and bottom surfaces is presented in Fig. 4.4. It should be noted that stronger wave entrapment at delamination

can be observed in the case of the wavefield at the top surface. It is because the delamination within the cross-section is located closer to the top surface. It makes it easier to detect delamination by processing wavefields at the top surface.

It must be noted that the output from the wave propagation model is in the form of a 3D matrix that contains the amplitudes of propagating waves at location (x, y) and time t_k. Hence, we can view it as a set of frames of propagating waves at discrete time moments. It is better visible if the root mean square (RMS) according to Eqn. 4.1 is applied to the wavefield. The RMS is defined as:

$$\hat{s}(x, y) = \sqrt{\frac{1}{N} \sum_{k-1}^{N} s(x, y, t_k)^2}, \tag{4.1}$$

where the number of sampling points N was 512. Therefore, the dataset was collapsed to 475 2D matrices in which amplitudes are stored as double-precision values. The result of this operation is presented in Fig. 4.5. Based on the image analysis, the shape of the delamination can be easier to discern for the top case.

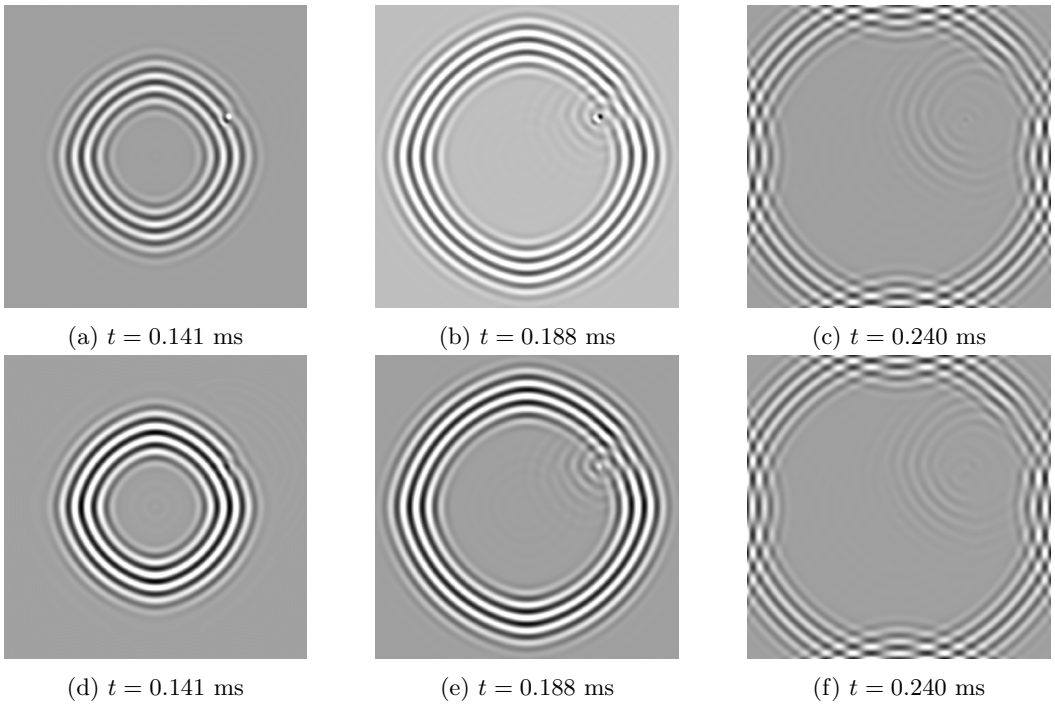

(a) $t = 0.141$ ms (b) $t = 0.188$ ms (c) $t = 0.240$ ms

(d) $t = 0.141$ ms (e) $t = 0.188$ ms (f) $t = 0.240$ ms

Figure 4.4: Full wavefield at the top surface (a)–(c) and the bottom surface (d)–(f), respectively, at selected time instances showing the interaction of guided waves with delamination.

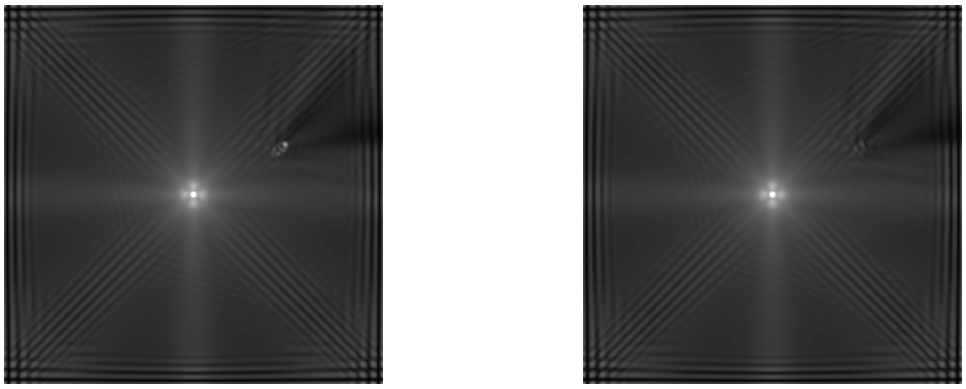

(a) top (b) bottom

Figure 4.5: RMS of the full wavefield from the top surface of the plate (a) and the bottom surface of the plate (b).

4.2 Delamination detection using fully connected CNN classifier

In this section, I present my initial attempt to solve the problem of delamination detection in CFRP materials by utilising CNN models for classification purposes.

The bounding box method was used for the classification of the location of the delamination with the input as RMS (Fig. 4.6a) and the binary representation of the delamination shape as ground truth (label shown in Fig. 4.6b).

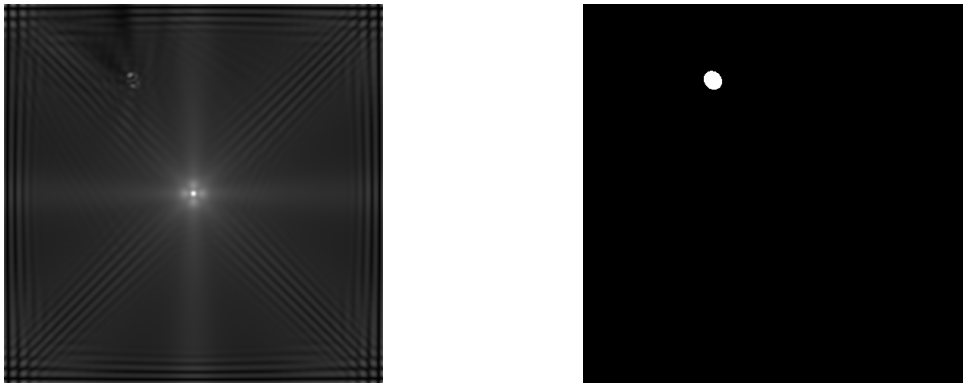

(a) (b)

Figure 4.6: (a) RMS image: from the top of the plate, (b) Label.

Accordingly, CNN models with fully connected dense layers were developed for delamination detection in CFRP. Moreover, the developed models are based on supervised learning to perform a classification task, therefore for each generated case of delamination a ground truth (label) is given.

4.2.1 Data preprocessing

In order to reduce the computation complexity of the model, the dataset for training the model was prepared by resizing the RMS input image to (448×448) pixels. Then, it was split into (14×14) patches, and each patch has a size of (32×32) pixels as shown in Fig. 4.7a. Consequently, the preprocessed dataset has a size of $(93100 \times 32 \times 32 \times 1)$, where (93100) is the total number of patches for all 475 cases.

To investigate the effect of increasing the resolution of RMS images over delamination identification, I made another preparation by upsampling the RMS input image to (512×512) pixels with cubic interpolation. Then the upsampled RMS image was split into 16×16 patches, and each patch has a size of (32×32) pixels as shown in Fig. 4.7b. The second preprocess dataset has a size of $(121600 \times 32 \times 32 \times 1)$, where (121600) is the total number of patches for all 475 cases. For each patch in the RMS input image, there is a corresponding patch in the ground truth image of size (32×32) as presented in Figs. 4.7c and 4.7d, respectively.

For training purposes, the dataset was divided into two portions: 80% training set and 20% testing set. Additionally, the validation set was created as a 20% of the training set.

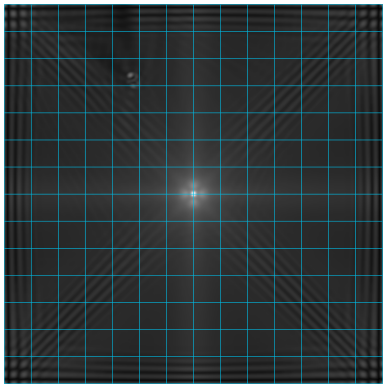

(a) RMS image splitted into (14×14) patches.

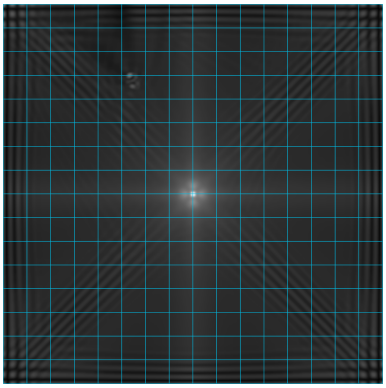

(b) RMS image splitted into (16×16) patches.

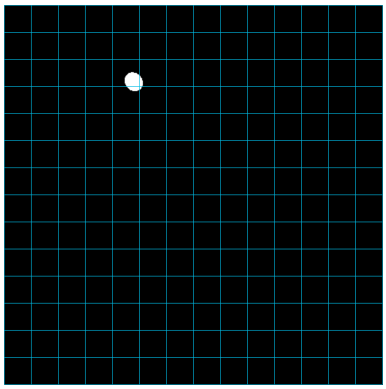

(c) Label image splitted into (14×14) patches.

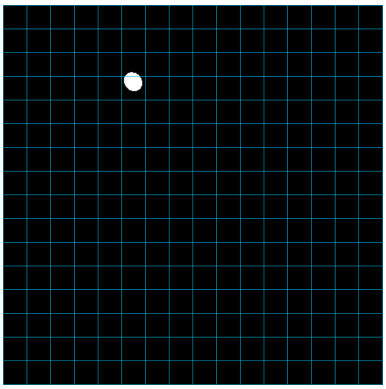

(d) Label image splitted into (16×16) patches.

Figure 4.7: Data preparation for bounding box method.

4.2.2 CNN classification models

The architecture of the implemented CNN model for classification purposes is presented in Fig. 4.8. The model takes an input patch of size (32 × 32) pixels, followed by a convolutional layer that has (64) filters of size (3 × 3). Moreover, in the convolution operation, the padding was set to be the same, and the activation function was Relu. Then, a pooling layer is applied, which has a pool filter of size (2 × 2) with a stride of (2). This operation of convolution and pooling is repeated two times. The output of the second pooling layer is flattened and fed into the dense layers in which the model has two fully connected layers. The first dense layer has (4096) neurons, and the second dense layer has (1024) neurons. A dropout of probability ($p = 0.5$) was added to the model to reduce the overfitting issue.

Moreover, selecting a proper objective function (loss) during training is important as the loss function reflects how well the model learns to predict. Hence, I have applied the mean square error (MSE) loss function depicted in Eqn. 4.2, which calculates the sum of the squared distances between the predicted output values and the ground truth values:

$$MSE = \frac{1}{M * N} \sum_{M,N} (Y_{(m,n)} - \hat{Y}_{(m,n)})^2, \tag{4.2}$$

where M and N are the number of rows and columns in the input images, $Y_{(m,n)}$ is the ground truth value, and $\hat{Y}_{(m,n)}$ is the predicted value.

The final layer in the model is the output layer, in which the model outputs two predictions (damaged and undamaged). Hence, the softmax activation function was used, which estimates the probability of each predicted output as being damaged or undamaged, implying that the sum of the two probabilities must be one. The reason behind choosing the softmax at the output layer is to avoid thresholding of the predicted output (e.g. a sigmoid produces values in a range between (0 and 1)). The softmax activation function is depicted by Eq. (4.3):

$$P(x)_i = \frac{e^{x_i}}{\sum_j^C e^{x_j}}. \tag{4.3}$$

where $P(x)_i$ is the probability of each target class x_j across all potential target classes x_j, C in our instance being two classes (damaged and undamaged).

Additionally, an argmax function is used to find the maximum probability between each of them in order to predict the label of the output (y_{pred}). Equation 4.4 depicts the argmax function.

$$y_{pred} = \text{argmax}_i \left(P(x)_i\right) \tag{4.4}$$

Accordingly, the whole patch of size (32 × 32) is classified as damaged if there is at

least one pixel of delamination, otherwise, it is considered undamaged. Finally, the predicted output (delamination) is surrounded by a bounding box as the final output.

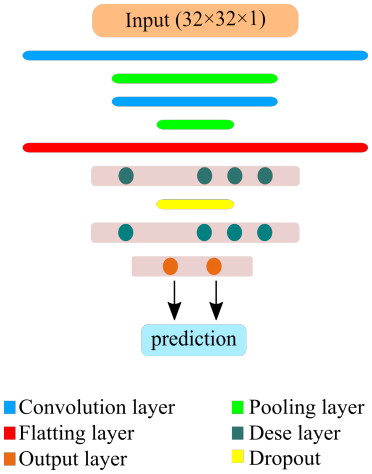

Figure 4.8: CNN classifier architecture.

4.3 FCN models for delamination identification

DL approaches have advanced quickly in recent years in many different real-world applications. An important and challenging application among others in DL is computer vision, in which we train a machine to automatically extract useful information from digital images, videos, and other visual inputs. Hence, an image segmentation technique that is well-known in computer vision applications is broadly utilised for such a purpose. Consequently, this technique aims to assign a class to each pixel in the input image. Thus, it can be utilised in several real-world applications like self-driving automobiles, medical imaging, traffic management systems, video surveillance, and more.

In this section, I present five DL models based on Fully Convolutional Networks (FCN) [154] that aim to automatically perform feature extraction by training the models using full wavefield images. Therefore, the models will learn by themselves to recognise the different patterns further, detect the delamination and localise it. Consequently, the implemented models will perform a pixel-wise segmentation by classifying every pixel of the input image as damaged or not.

The key idea of FCN is to replace the dense layers of neurons with convolutional layers, hence, reducing the computation complexity. Hence, FCN can be implemented by stacking convolutional layers and skipping dense layers in an encoder-decoder scheme. The encoder aims to produce compressed feature maps from the input image at various scale levels using cascaded convolutions and downsampling operations. While the

decoder is responsible for upsampling the condensed feature maps to the original input shape.

The softmax function (see Eqn. 4.3) was used at the output layer for all developed FCN models. Additionally, the categorical cross-entropy (CCE) loss function [155], commonly known as the "softmax loss function", was utilised in all FCN models. The difference between the actual damage (ground truth) and the expected damage is estimated using CCE as the objective function. The CCE is illustrated by Eq. (4.5), where $P(x)_i$ refers to the softmax value of the target class:

$$CCE = -\log\left(P(x)_i\right). \tag{4.5}$$

It should be noted, as there are only two classes to predict, a sigmoid activation function at the output layer can be combined with a binary cross-entropy (BCE) without affecting the predicted outputs.

The implemented DL models for pixel-wise semantic segmentation for delaminations identification are depicted in Figure 4.9. In the following subsections (4.3.1 - 4.3.6), the data preprocessing and the five DL models will be illustrated.

4.3.1 Data preprocessing

The implemented FCN models for pixel-wise image segmentation have a one-to-one prediction scheme. In other words, the models take one image input and predict one output image. Accordingly, to train the FCN models, the calculated RMS images of the full wavefield at the bottom surface of the plate (see Fig. 4.5b) were utilised. The dataset consisting of RMS images which were used in this research paper is available online [156].

To enhance the performance of the optimizer during the training process, the colour scale values were normalised to a range of $(0-1)$ instead of the initial scale which was in a range of $(0-255)$. Furthermore, I have applied data augmentation to the dataset (475 RMS images) by flipping the images horizontally, vertically, and diagonally. As a result, the dataset size increased four times -1900 images were produced. I have split the dataset into two portions: 80% for the training set and 20% for the testing set. Moreover, a K-folds cross-validation technique [157] was applied to the training set to reduce the overfitting which happens when the model is able to fit on the training data, while it poorly fit on the new unseen data. In other words, the model only learns the patterns of the training data therefore the model will not generalise well. The main advantage of the K-folds method versus a regular train/test split is to reduce the overfitting by utilising data more efficiently as every data sample is used in both

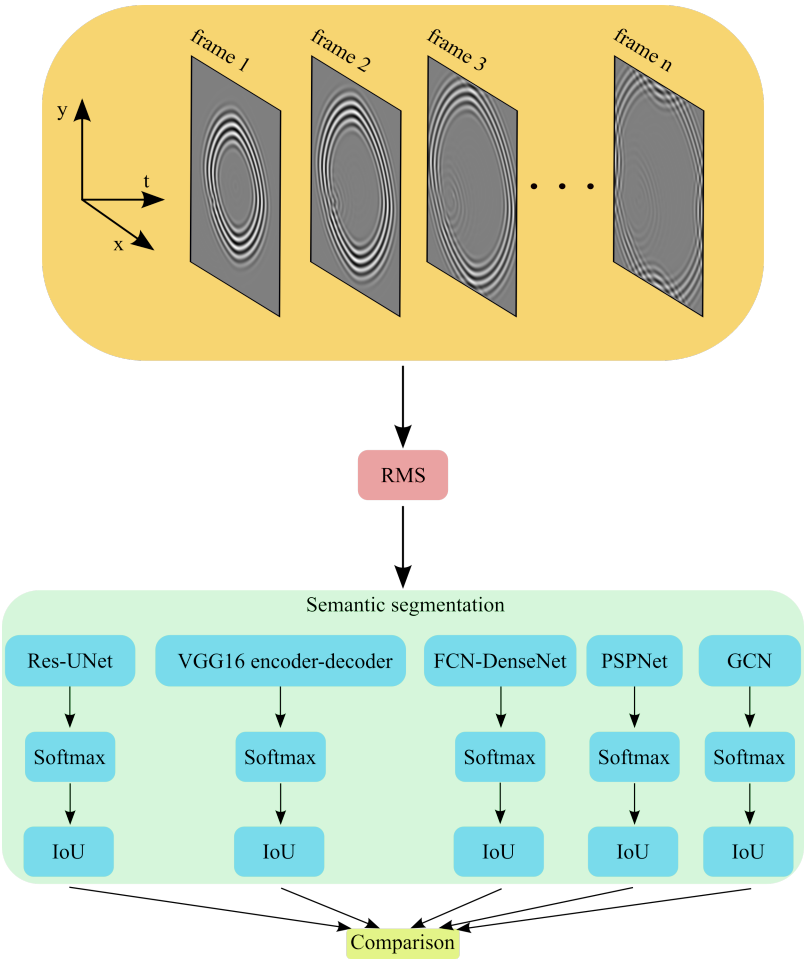

Figure 4.9: Schematic diagram of the approach used for comparison of semantic segmentation methods accuracy.

training and validation. Therefore, by using this technique, I aim to improve the ability of the model to generalise and reduce overfitting. Figure 4.10 illustrates the K-folds cross validation technique.

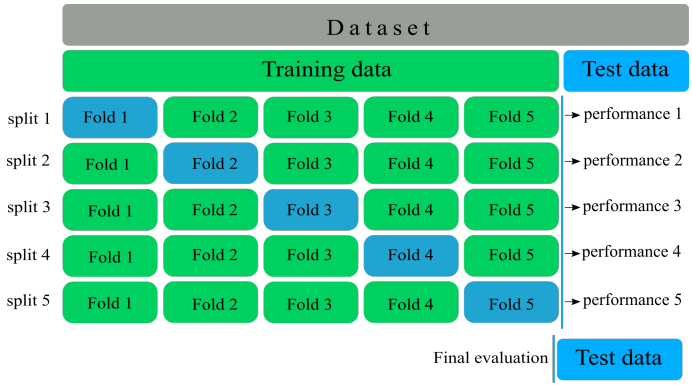

Figure 4.10: K-folds cross validation.

4.3.2 Residual UNet model

The Residual UNet (Res-UNet) model was inspired based on residual learning [158] and UNet approaches [159]. The Res-UNet architecture is depicted in Fig. 4.11. The encoder (compressive) path aims to capture the detailed features of an input image, whereas the decoder (decompressive) path aims to perform exact localization. As a result, residual connections were established at two levels in order to prevent the spatial and contextual information from the preceding layers from being lost:

- at each step of the encoder and decoder paths,
- between the encoder parts and their corresponding decoder parts (skip connections) which ensures that the feature maps which were learned during the downsampling will be utilized in the reconstruction.

Several downsampling (Max-pool) blocks are used in the encoder section. Each block applies two convolutional layers followed by a (2×2) max pooling with a (2×2) strides that selects the maximum value in a local pool filter in one feature map (or n-feature maps), resulting in a reduction in the dimension of feature maps [113], and in turn, a reduction in computation complexity. Each convolutional layer does (3×3) convolution operations, then batch normalization (BN), and finally a Relu. Furthermore, after each downsampling block, the number of convolutional filters is increased, allowing the model to learn complex patterns successfully.

The bottleneck layer is a joining point in the model's deepest layer, located between the encoder and the decoder. Two convolutional layers with (1024) filters make up the bottleneck, which aids the model in learning and recognizing complex features.

The decoder is composed of a number of upsampling blocks that function together to recover original input dimensions and improve resolution. As in the downsampling block, each upsampling block transmits the input through two convolution layers, followed by a transmission up layer consisting of a transposed convolutional layer (upsampling). The transposed convolutional layer varies from the standard upsampling function in that it introduces learnable parameters for the transposed convolution filters, which improve learning process of the model. Furthermore, the number of filters used by the convolutional layer is reduced by half after each upsampling operation to keep the model symmetrical.

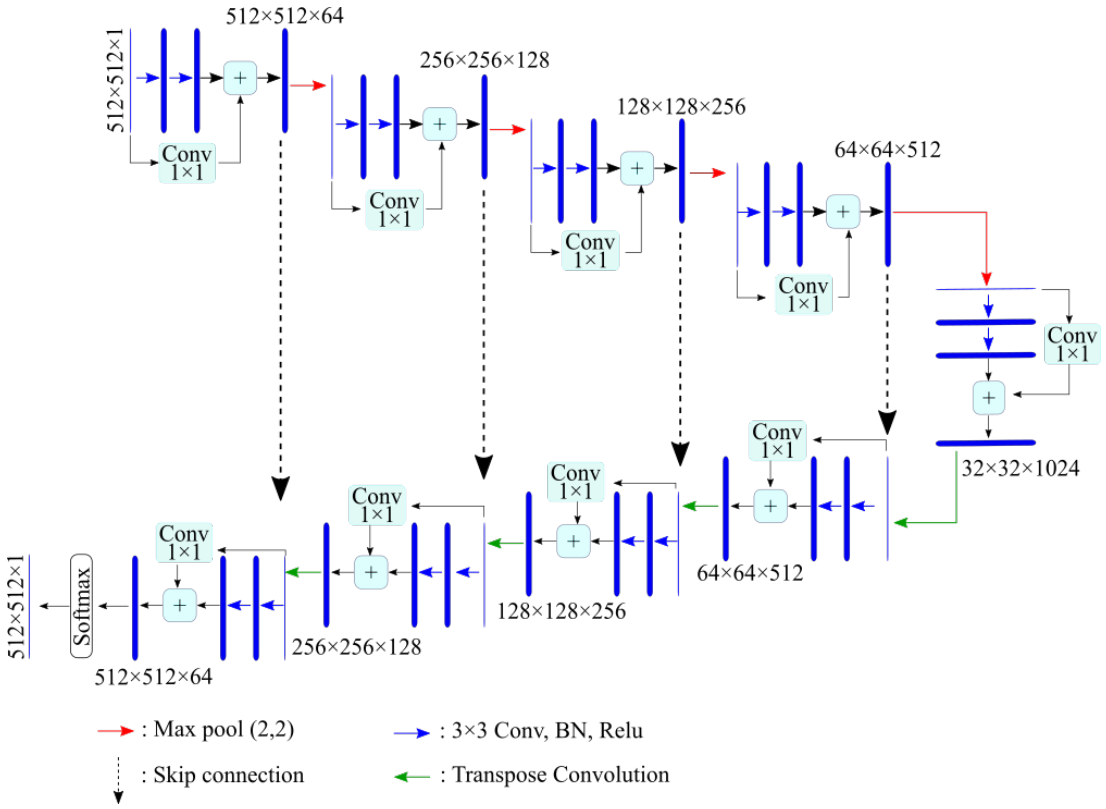

Figure 4.11: Res-UNet architecture.

4.3.3 VGG16 encoder-decoder

The application of the VGG16 [160] architecture as a backbone encoder to the UNet [159] approach is addressed in this model. VGG16 is a classification algorithm that consists of 13 convolutional layers, pooling layers, and (3) dense layers. The dense layers were removed form the original VGG16 model, and a 13 convolutional layers were applied resulting in an encoder-decoder scheme for pixel-wise image segmentation. The architecture of the VGG16 encoder-decoder model is shown in Fig. 4.12. The model is U-shaped like, and consists of two parts: encoder and decoder. The encoder is made up of (five) convolutional blocks with a total of (13) (3×3) convolutional layers, followed by BN and Relu as the activation function. After each convolutional block, a Max pool operation with a pool size of (2×2) is conducted, followed by dropout. The upsampling process is used to retrieve spatial resolution, and it contains 5 convolutional blocks of total 13 convolutional layers. Bilinear interpolation with (2×2) kernel size is used for upsampling. In order to improve recovering fine-grained information, skip connections were added between downsampling blocks and the matching upsampling blocks, allowing feature re-usability from earlier layers.

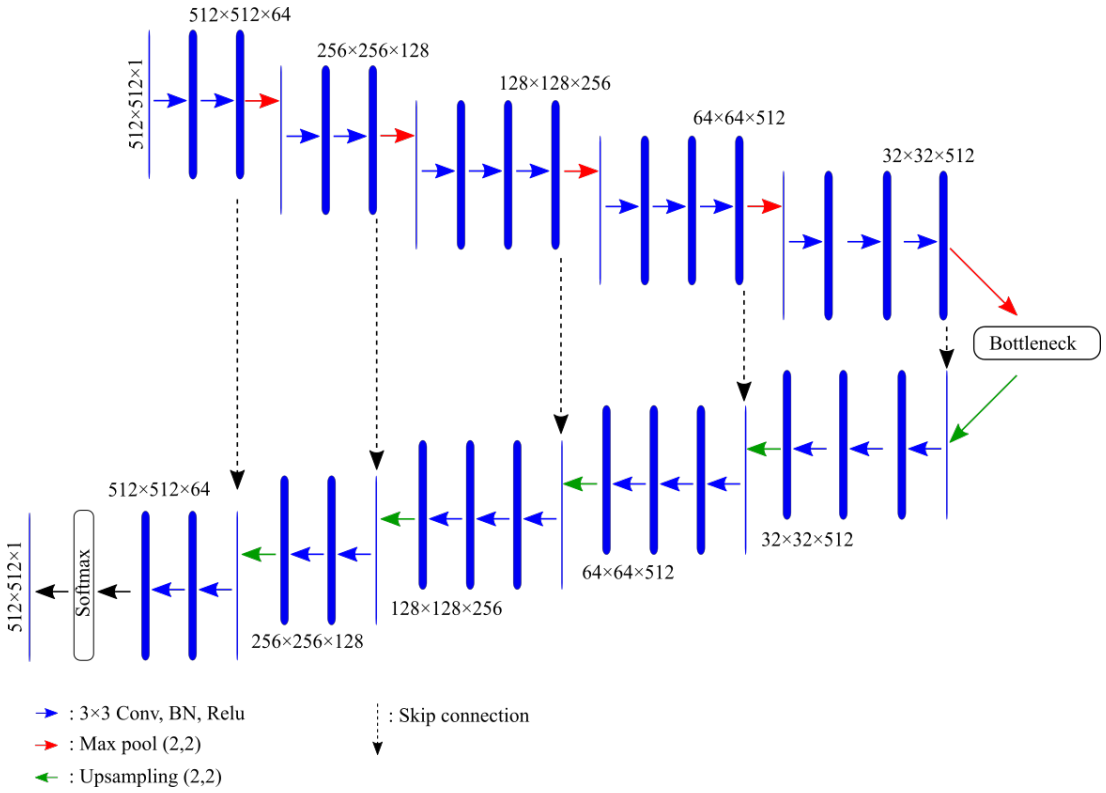

Figure 4.12: VGG16 encoder decoder architecture.

4.3.4 FCN-DenseNet model

FCN-DenseNet is a pixel-wise image segmentation algorithm that was first introduced in [161]. To boost the resolution of the final feature map, FCN-DenseNet uses a U-shaped encoder-decoder architecture with skip connections between downsampling and upsampling channels. Hence, FCN-DenseNet introduced a dense block representing its main component. The dense block is made up of n layers, each of which is made up of a set of operations, as given in Table 4.1. The purpose of the dense block is to concatenate the input (feature maps) of a layer with its output (feature maps) to emphasize spatial details information. The architecture of the dense block is presented in Fig. 4.13.

A transition down layer was added to execute a (1×1) convolution followed by a (2×2) Maxpooling operation to minimize the spatial dimensionality of the resulting feature maps. As a result, a transition-up layer was added to recover the spatial resolution. FCN-DenseNet essentially upsamples feature maps from the previous layer using a transpose convolution technique. Upsampled feature maps are concatenated with those produced by the skip connection to provide the input to a new dense block.

As the upsampling approach expands the spatial resolution of the feature maps, the

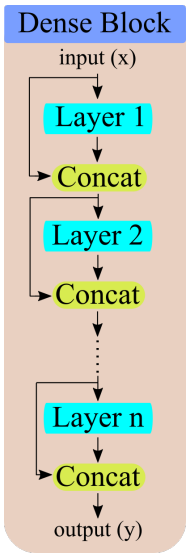

Figure 4.13: Dense block architecture.

input to the dense block is not concatenated with its output during upsampling to avoid the overhead of memory shortage. The FCN-DenseNet architecture for image segmentation utilized for delamination detection is shown in Fig. 4.14. Table 4.1 presents the architecture of a single layer, the transition down and transition up layers in details.

Layer	Transition Down	Transition Up
Batch Normalization	Batch Normalization	3×3 Transposed Convolution
Relu	Relu	strides $= (2 \times 2)$
(3×3) Convolution	(1×1) Convolution	
Dropout $p = 0.2$	Dropout $p = 0.2$	
	(2×2) Maxpooling	

Table 4.1: Layer, Transition Down and Transition Up layers.

4.3.5 Pyramid Scene Parsing Network

The main idea of PSPNet [162] is to combine local and global features to give appropriate global contextual information for pixel-level scene parsing. As a result, a spatial pyramid pooling module was developed to execute four different layers of pooling with four different pooling sizes and strides. The pyramid pooling module is able to capture contextual features from many scales in this way.

To enhance the PSPNet model a ResNet-50 model [158] was added. It works as a backbone for feature map extraction with dilation at the last two layers of ResNet.

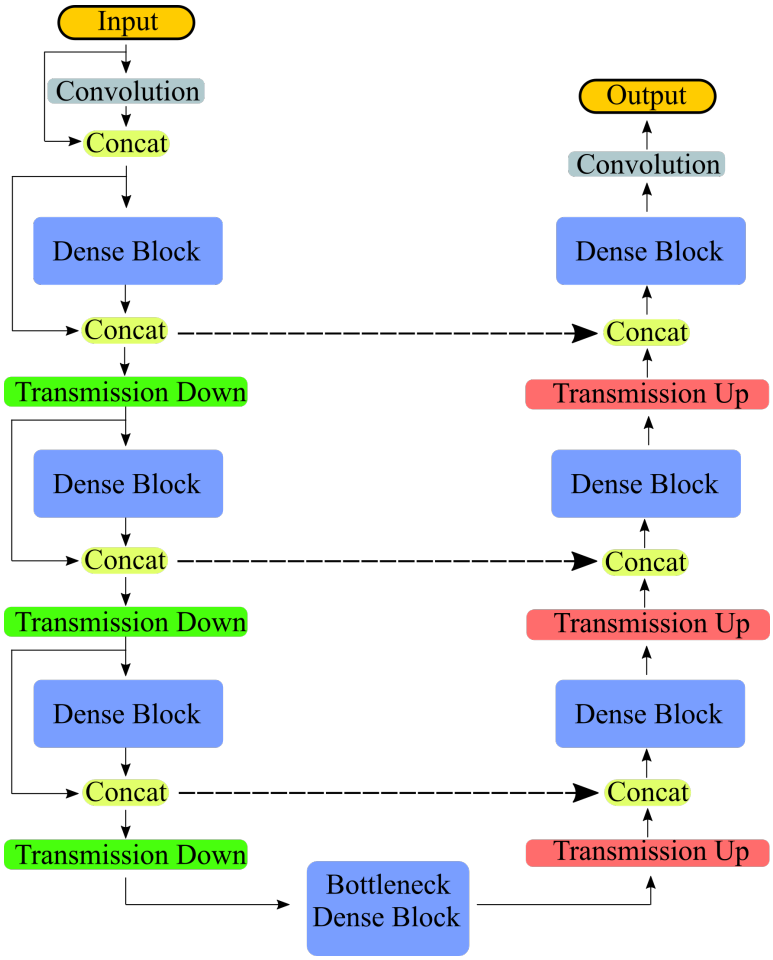

Figure 4.14: FCN-DenseNet architecture.

The implemented PSPNet architecture is shown in Fig. 4.15. Hence, a pyramid pooling module was utilised at 4 pooling levels. The coarsest level of a single bin output depicted in the red box was generated using global average pooling. (2×2), (4×4), and (8×8) are the pooling sizes for the other three sub-region levels, respectively. To minimize the dimensionality of the generated feature maps, a (1×1) convolutional layer was applied, followed by a BN and Relu. Subsequently, bilinear interpolation was used to upsample the feature maps created at each level. Furthermore, the upsampled features are combined with the output of ResNet-50 to produce both local and global context information. The pixel-wise segmentation predictions were then generated using two cascaded convolutional layers.

4.3.6 Global Convolutional Network

Peng et al. [163] introduced the Global Convolutional Network (GCN) to address the importance of having large kernels for both localization and classification operations for

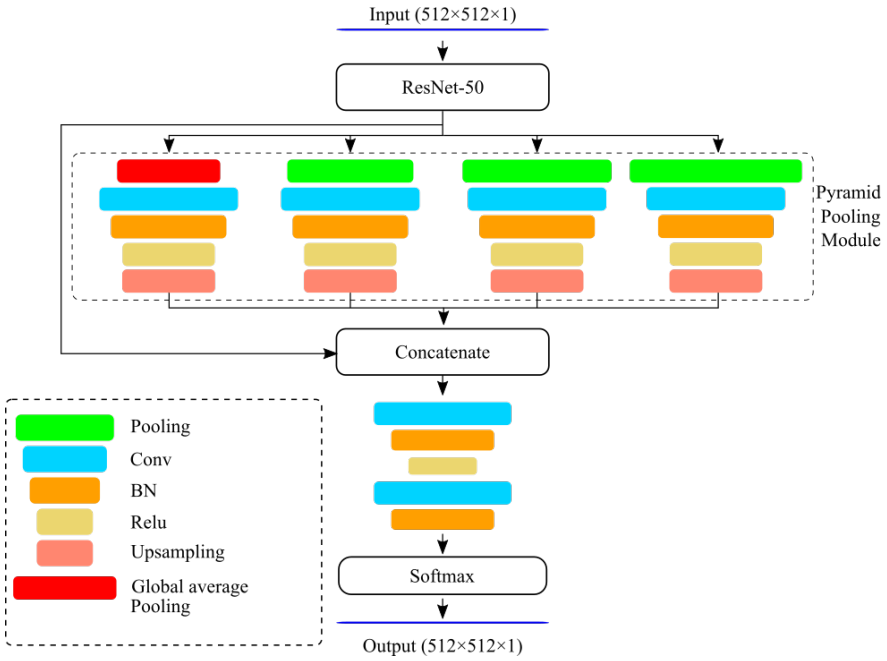

Figure 4.15: PSPNet architecture.

semantic segmentation in order to increase the size of respective fields. However, when performing classification and localization tasks, a contradiction emerges due to the fact that classification tasks necessitate invariant models for various transformations such as rotation and translation while localisation tasks necessitate models that are sensitive to any modification and appropriately assign each pixel to its semantic category. To alleviate such contradiction, two design principles were proposed: (1) For the classification task, in order to improve the capability of the model to handle different transformations, a large kernel size must be used to enable dense connections between feature maps and per-pixel classifiers; (2) for localisation task, the model must be fully convolutional. Additionally, fully connected or global pooling layers are not applied as these layers will discard the localisation information.

The implemented GCN technique for semantic segmentation is shown in Fig. 4.16.

A residual network was used as a backbone for improving the feature extraction process, as demonstrated in Fig. 4.16, further, the residual block is presented in Fig. 4.17a. A GCN block presented in Fig. 4.17b is placed after each residual block, which employs a mix of $(1 \times k)+(k \times 1)$ and $(k \times 1)+(1 \times k)$ convolutions to establish dense connections within $(k \times k)$ region in the feature map. The boundary refinement (BR) block, depicted in Fig. 4.17c, is then used to improve the predictions along the object borders, resulting in a lower resolution score map. Furthermore, the upsampling operation is done recursively. It upsamples the low-resolution score maps and then concatenate them with a higher one to produce a new score maps. The deconvolution operation is

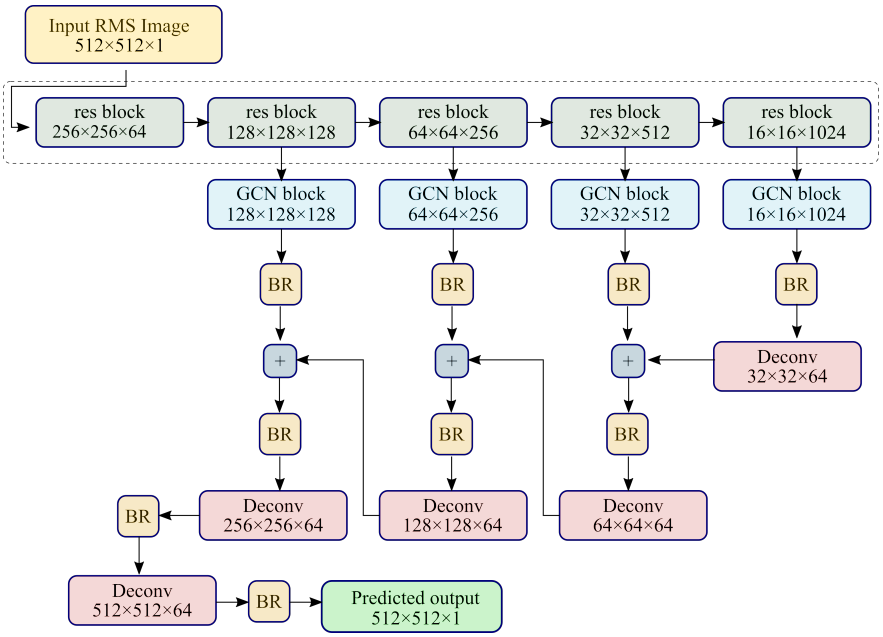

Figure 4.16: Global Convolution Network whole architecture.

repeated until the original image size is obtained.

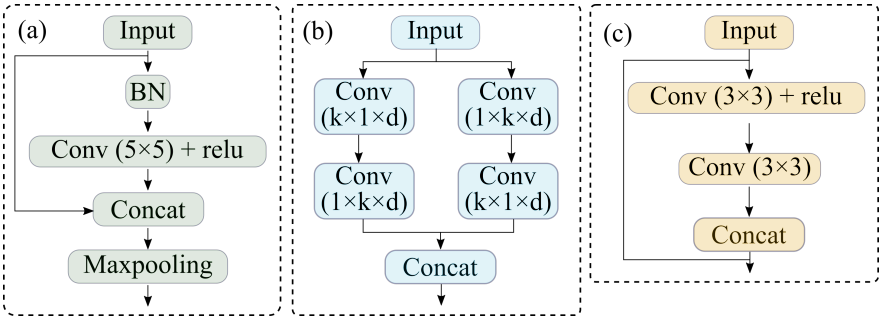

Figure 4.17: (a) Residual block, (b) Global Convolution Network block, (c) Boundary Refinement.

4.4 Convergence of FCN models

When a deep learning model approaches convergence during training, the loss falls within an error range around the final value. In other words, a model converges when extra training is ineffective. Figure 4.18 presents the plots of the training loss and validation loss values with respect to epochs during the training phase regarding the developed models. I set the number of epochs in all developed FCN models to 20, as this was sufficient to train the models. It is clear that all developed FCN models converge after a certain number of epochs, in which the loss reaches its minimum

value. Furthermore, the FCN models do not show any sign of overfitting or underfitting as shown in Figs. 4.18a, 4.18b, 4.18c, 4.18d, and 4.18e regarding Res-UNet, VGG16 encoder-decoder, FCN-DenseNet, PSPNet and GCN, receptively.

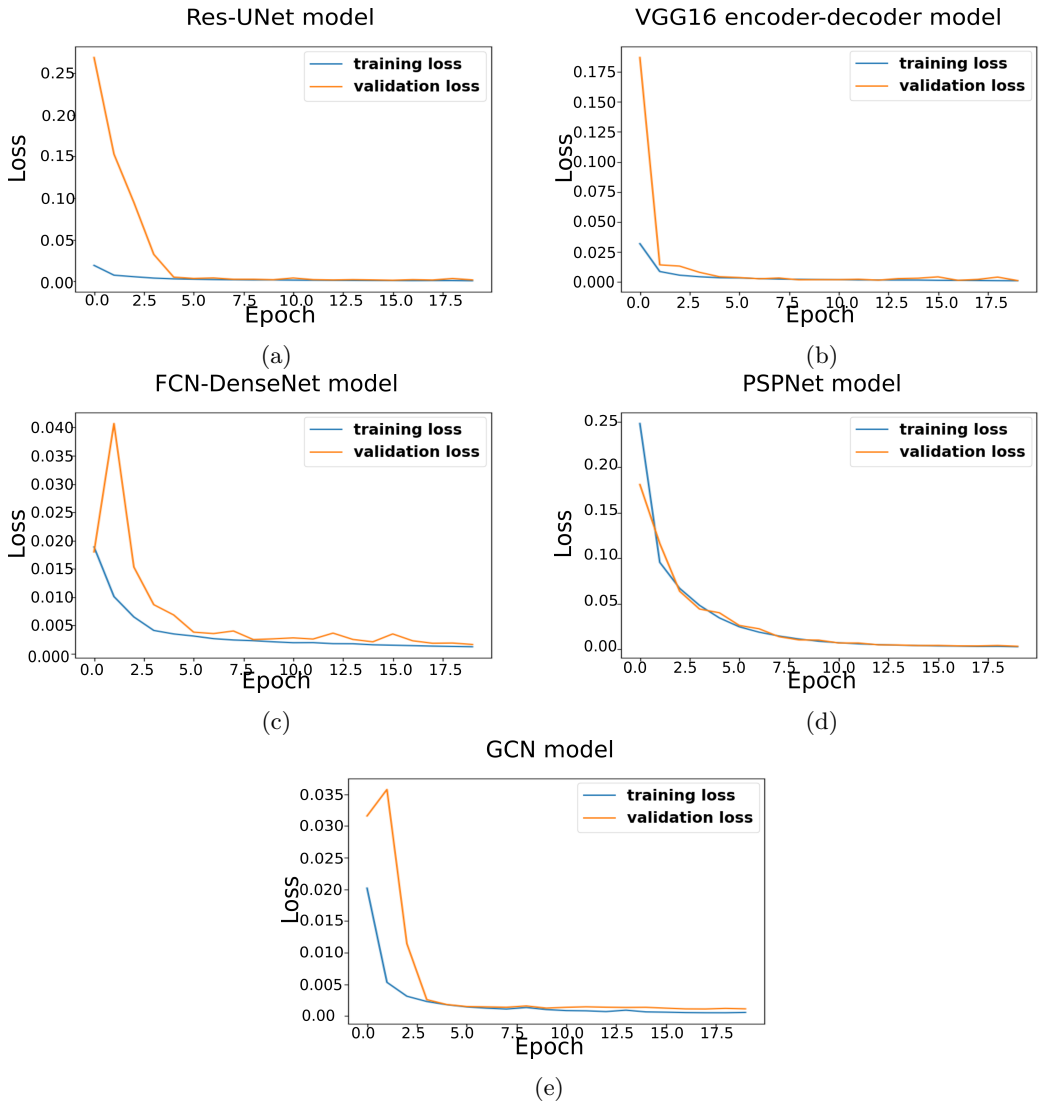

Figure 4.18: FCN models: training and validation losses during training phase.

4.5 DL model for delamination identification based on animation of full wavefield

In this section, I utilised full wavefield frames of Lamb waves propagation in an end-to-end deep learning model to identify CFRP delamination instead of using RMS images as in the FCN models. Accordingly, a many-to-one prediction scheme was adopted by employing convolutional-based recurrent neural networks (RNNs) to perform pixel-wise image segmentation. A sequence of full wavefield frames is fed into the proposed deep learning models to identify the delamination. Hence, in the segmentation problem, there are two classes: undamaged and damaged. To the best of my knowledge, it is the first implementation of deep neural networks utilising Lamb wave propagation animations for damage imaging with semantic segmentation. The proposed model showed excellent results in identifying the delamination in the numerically generated dataset, and it also showed its capability to generalise delamination identification in real-world scenarios.

4.5.1 Data preprocessing

Similar to the previous work [164], 475 cases were simulated, representing Lamb wave propagation and interaction with single delamination for each case.

It should be underlined that the previous dataset contained the RMS of the full wavefield, representing wave energy spatial distribution in the form of images for each delamination case [156]. On the other hand, the currently utilised dataset contains frames of propagating waves (512 frames for each delamination scenario). The new dataset is available online [165].

As mentioned earlier, the dataset contains 475 different cases of delaminations, with 512 frames per case, producing a total number of $243,200$ frames with a frame size of (500×500) pixels representing the geometry of the specimen of size (500×500) mm^2. Thus, using all frames in each case has high computational and memory costs. Frames displaying the propagation of guided waves before interaction with the delamination have no features to be extracted (see Fig. 4.19). Hence, for training, only a certain number of frames were selected from the initial occurrence of the interactions with the delamination.

Figure 4.19 shows selected frames at different time-steps of the propagating Lamb waves before and after the interaction with the damage. Frame f_1 represents the initial interactions with the delamination, which was calculated using the delamination location and the velocity of the $A0$ Lamb wave mode. While frame f_m represents the

last frame in the training sequence window, $m = 24$ for the developed model which will be discussed in the next subsection.

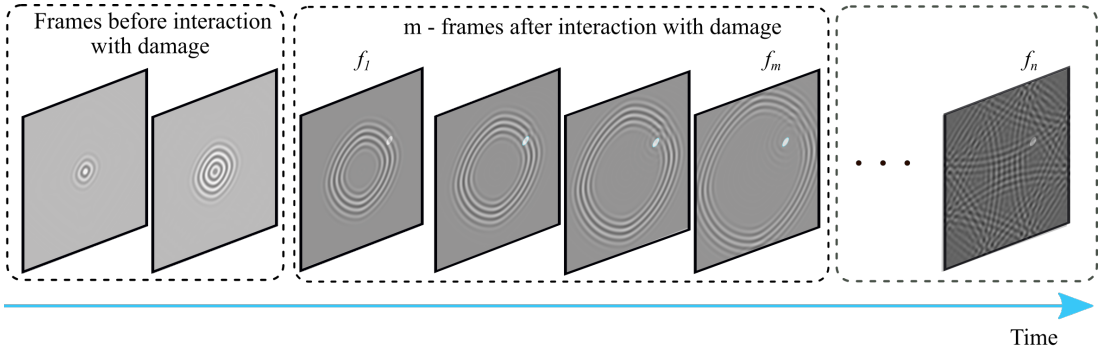

Figure 4.19: Sample frames of full wave propagation.

Furthermore, the dataset was divided into two sets: training and testing, with a ratio of 80% and 20% respectively. Moreover, a certain portion of the training set was preserved as a validation set to validate the model during the training process. Additionally, the dataset was normalised to a range of $(0, 1)$ to improve the convergence of the gradient descent algorithm.

Additionally, for the training purposes, I have upsampled the frames (by using cubic interpolation) to 512×512 pixels to maintain the symmetrical shape during the encoding and decoding process. Further, the validation sets have portions of 10% and 20% regarding the training set.

Figure 4.20 illustrates the complete procedure of obtaining intermediate predictions for the testing cases and finally calculating the RMS image, where f_1 refers to the starting frame and f_n is the last frame, $(n = 512)$ in our dataset. Further, m refers to the number of frames in the window, hence, $m = 24$ frames for the developed model, and k represents the total number of windows. Accordingly, I slide the window over all input frames. The shift of the window is one frame at a time. Deep learning model predictions $\hat{Y_k}$ are obtained for each window and combined to the final damage map by using the $\overline{RMS}$:

$$\overline{RMS} = \sqrt{\frac{1}{N}\sum_{k=1}^{N} \hat{Y_k}^2}. \tag{4.6}$$

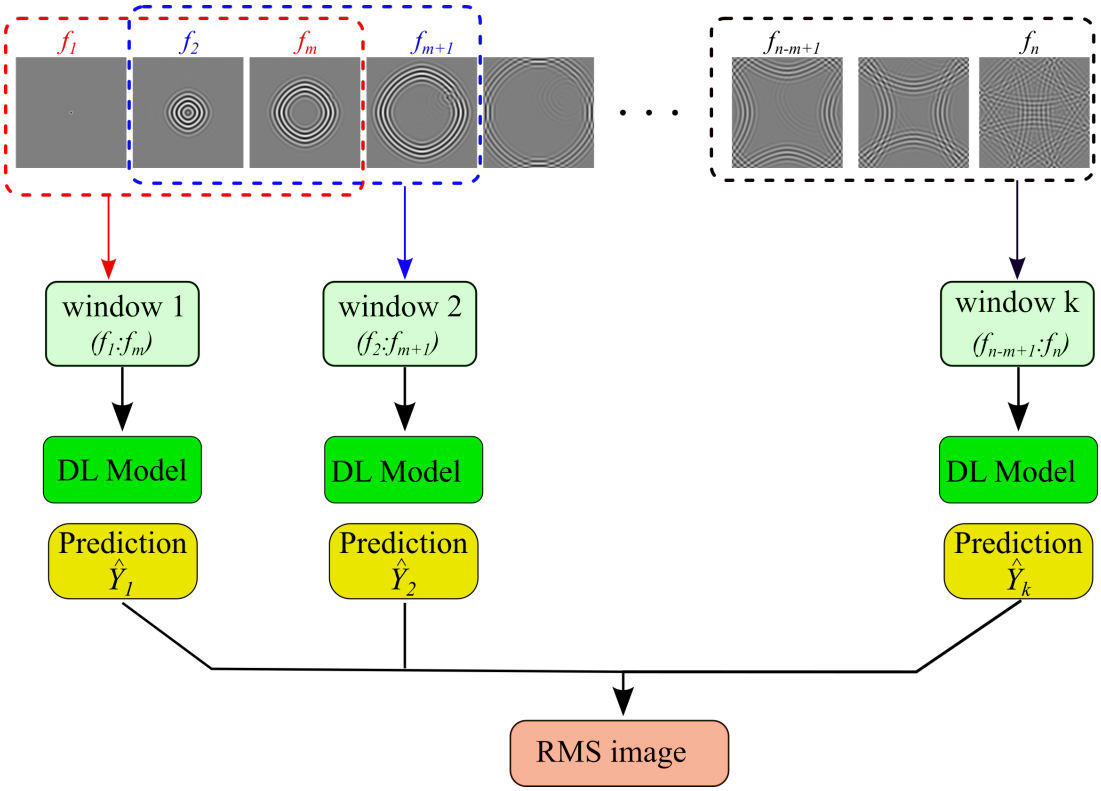

Figure 4.20: The procedure of calculating the RMS prediction image (damage map).

4.5.2 Autoencoder ConvLSTM model

In this work, I developed an end-to-end deep learning model utilising full wavefield frames of Lamb wave propagation for delamination identification in CFRP materials as presented in Fig. 4.21. The developed model has a scheme of many-to-one sequence prediction, which takes n number of frames representing the full wavefield propagation through time and their interaction with the delamination to extract damage features, and finally predict the delamination location, shape, and size in a single output image.

In the implemented model, I applied an autoencoder technique (AE) which is well-known for extracting spatial features. The idea of AE is to compress the input data within the encoding process then learn how to reconstruct it back from the reduced encoded representation (latent space) to a representation that is as close to the original input as possible. Hence, I have investigated the use of AE to process a sequence of input frames to perform image segmentation. Therefore, a Time Distributed layer presented in Fig. 4.22 was introduced to the model, in which it distributes the input frames into the AE layers in order to process them independently.

As previously mentioned, an AE consists of three parts: the encoder, the bottleneck, and the decoder. The encoder is responsible for learning how to reduce the input

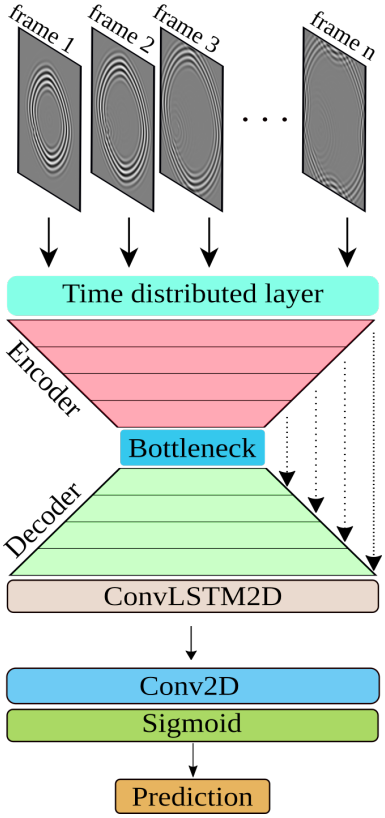

Figure 4.21: Autoencoder ConvLSTM model architecture.

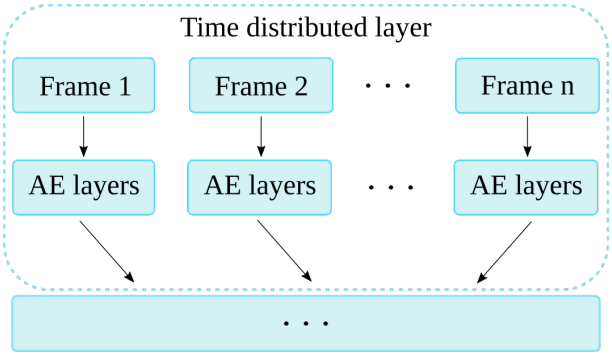

Figure 4.22: Flow of input frames using Time distributed layer.

dimensions and compress the input data into an encoded representation.

The encoder part presented in 4.21 consists of four levels of downsampling. The purpose of having different scale levels is to extract feature maps from the input image at different scales. Every level at the encoder consists of two 2D convolution operations followed by a Batch Normalization then a Dropout is applied. Furthermore, at the end of each level a Maxpooling operation is applied to reduce the dimensionality of the inputs.

The bottleneck presented in Fig. 4.21 has the lowest level of dimensions of the input data, further it consists of two 2D convolution operations followed by a Batch Normaliza-

tion.

The decoder part presented in Fig. 4.21, is responsible for learning how to restore the original dimensions of the input. The decoder part consists of two 2D convolutional operations followed by Batch Normalization and Dropout, and an upsampling operation is applied at the end of each decoder level to retrieve the dimensions of its inputs. Skip connections linking the encoder with the corresponding decoder levels were added to enhance the features extraction process. The outputs of the decoder were forwarded into the ConvLSTM2D layer to learn long-term spatiotemporal features.

Further, I applied a 2D convolutional layer as the final output layer followed by a sigmoid activation function which outputs values in a range from $(0, 1)$ to indicate the delamination probability. Consequently, a threshold value must be chosen to classify the output into a damaged represented by (1) or undamaged represented by (0). Hence, I set the threshold value to (0.5) to exclude all values below the threshold by considering them as undamaged and taking only those values greater than the threshold to be considered as damaged.

Furthermore, Fig. 4.23 presents the plot of the training loss and validation loss values with respect to epochs during the training phase of the AE-ConvLSTM model. The number of epochs for the AE-ConvLSTM model was set to 100. As shown in the Fig. 4.23, the developed AE-ConvLSTM model converges, and it has no signs of overfitting or underfitting.

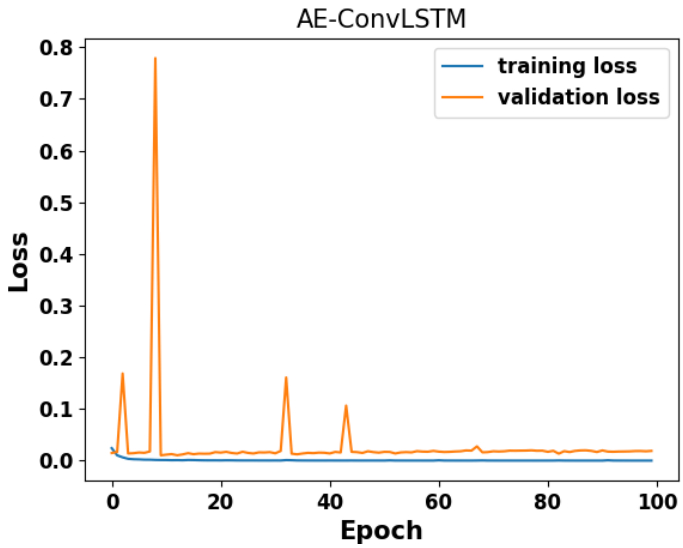

Figure 4.23: AE-ConvLSTM model: training and validation losses during training phase.

4.6 Super-Resolution image reconstruction for delamination identification

In this section, I present a framework for full wavefield reconstruction of propagating Lamb waves from spatially sparse SLDV measurements of resolution below the Nyquist wavelength λ_N. The Nyquist wavelength is the shortest spatial wavelength that can be accurately recovered from wavefield by sequential observations with spacing Δx which is defined as $\lambda_N = 2\Delta x$.

For the first time, an end-to-end approach for the SR problem is used in which a deep learning neural network is trained on a synthetic dataset and tested on experimental data acquired by SLDV. It means that the approach is solely based on DLSR. It is different from methods presented in the literature which utilize CS theory [64, 69] or CS theory in conjunction with super-resolution convolutional neural networks for wavefield image enhancement [77, 78]. The efficacy of the developed framework is presented and compared with the conventional CS approach. The performance of the proposed technique is validated by an experiment performed on a plate made of carbon fibre reinforced polymer (CFRP) with embedded Teflon inserts simulating delaminations.

4.6.1 Dataset preparation

To train a deep learning model to perform super-resolution image reconstruction, I have to reproduce a low-resolution training set from the original high-resolution dataset. Initially, I resized the frames in the original high-resolution dataset to (512×512) pixels to obtain the desired output frame shape while performing image reconstruction from the low-to high-resolution.

The maximum permissible distance between grid points according to Nyquist theorem is calculated as in Eqn. (4.7):

$$d_{max} = \frac{1}{2 * k_{max}} = \frac{1}{2 * 51.28\ [\text{m}]} = \frac{\lambda}{2} = \frac{19.5}{2}\ [\text{mm}]. \tag{4.7}$$

where k_{max} is the maximum wavenumber, and λ is the shortest wavelength.

On the other hand, the longest distance between grid points on uniform square grid in 2D space is along the diagonal as shown in Fig. 4.24. Therefore, the number of Nyquist sampling points along edges of the plate is defined as:

$$\begin{aligned} N_x &= \frac{L}{d_{max}/\sqrt{2}}, \\ N_y &= \frac{W}{d_{max}/\sqrt{2}}, \end{aligned} \tag{4.8}$$

where L is the plate length, and W is the plate width.

In our particular case, $L = W = 500$ [mm], and number of Nyquist points $N_x = N_y = N_{Nyq} = 73$.

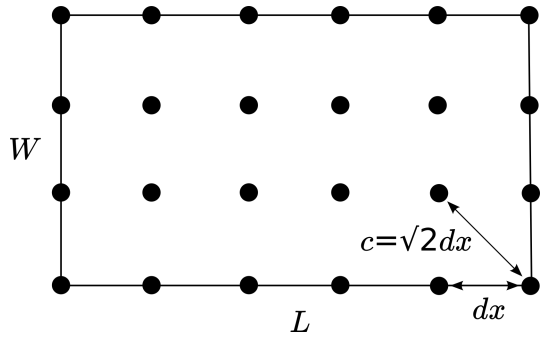

Figure 4.24: Longest distance between grid points.

To train the DLSR model, I have generated low-resolution full wavefield frames of $(n \times n)$ points, where $n = 32$, which is below the Nyquist sampling rate of a 2D frame. Hence, I have performed image subsampling with bi-cubic interpolation and a uniform mesh of size (32×32) pixels with a compression rate (CR) of 19.2% from the Nyquist sampling rate as depicted in Eqn. (4.9):

$$CR(\%) = (\frac{n}{N_{Nyq}})^2 = (\frac{32}{73})^2 = 19.2\% \tag{4.9}$$

Figure 4.25 shows a three SR Frames with their corresponding LR frames at different time steps.

Furthermore, I selected (128) consecutive full wavefield frames per delamination case to reduce computation complexity during training. The selected frames start from the initial occurrence of the interaction with the delamination, as frames displaying the propagation of guided waves before interacting with the delamination have no valuable features to be extracted.

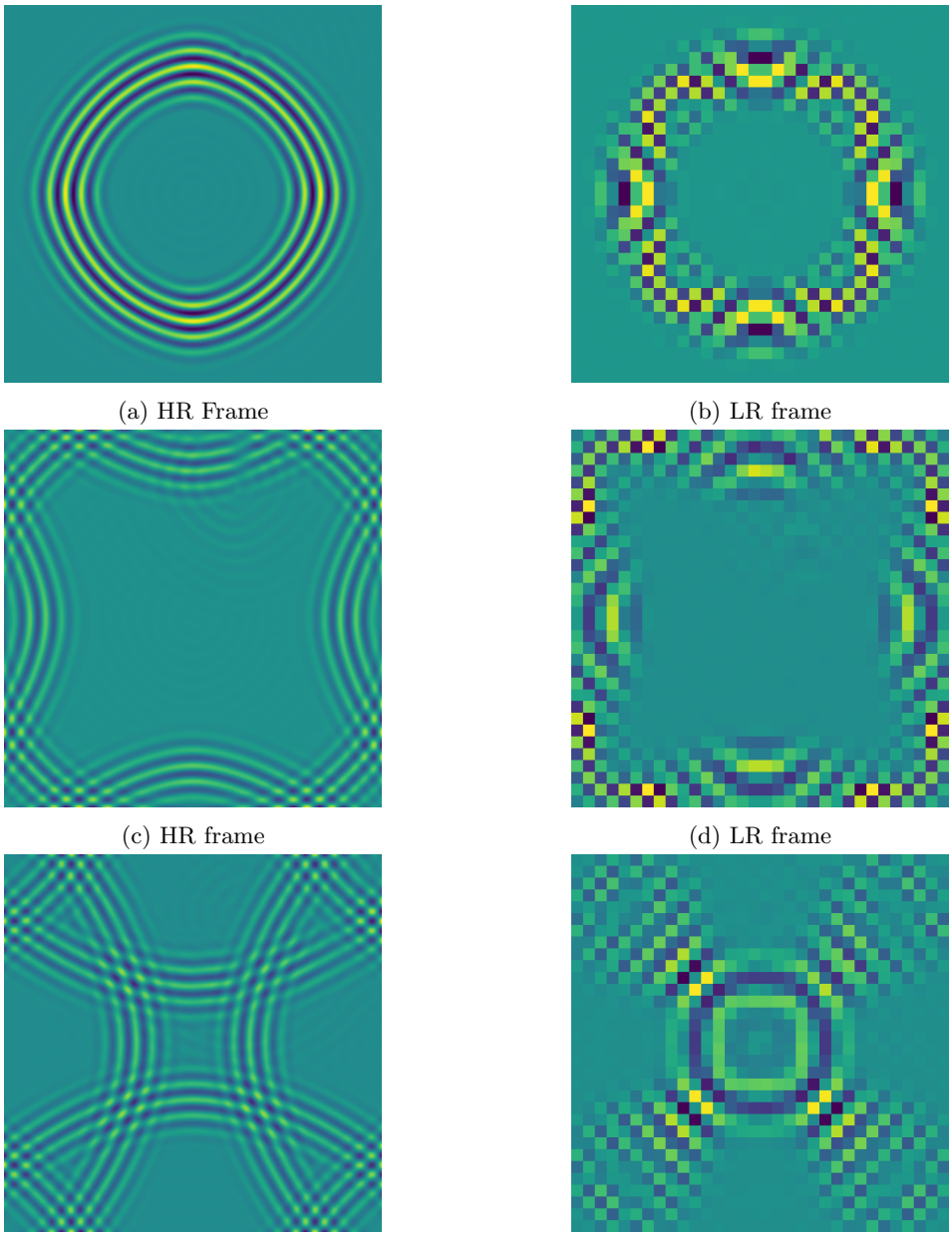

(a) HR Frame (b) LR frame

(c) HR frame (d) LR frame

(e) HR frame (f) LR frame

Figure 4.25: High-resolution (HR) and Low-resolution (LR) frames at different time steps.

4.6.2 DL approach for SR image reconstruction

Single image Super-Resolution (SISR) aims to generate a visually pleasing high-resolution (HR) image from its de-graded low-resolution (LR) measurement.

Residual dense network (RDN) was introduced by Zhang et al. [72] to perform SISR. RDN aims to solve the issue of unexploited hierarchical features obtained from the original low-resolution (LR) images. Accordingly, to resolve this issue RND introduced a residual dense block (RDB) which is capable to fully exploit all hierarchical features obtained from all convolutional layers.

Figure 4.26 shows the architecture of a RDB which consists of four layers (L_1, L_2, L_3,-L_4). Therefore, a RDB can extract the abundant local features through dense connected

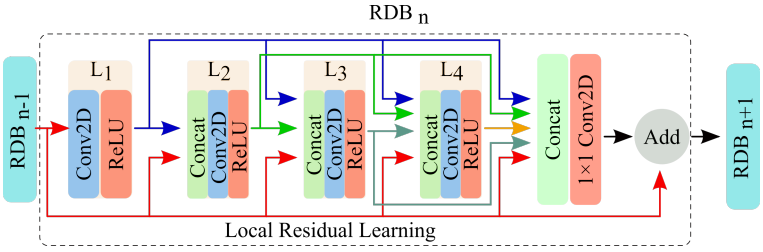

Figure 4.26: Residual Dense Block architecture.

convolutional layers leading to a local residual learning. The local feature fusion within each RDB is utilised to learn more useful features from the previous and current local features, therefore, stabilising the training process as the network depth increases. Consequently, RDB enables direct links from the previous RDB to all layers of the current RDB, resulting in a contiguous memory (CM) mechanism.

In this work, the implemented deep learning model was inspired by the RDN [72]. The model architecture is presented in Fig. 4.27. The first segment in the model is the

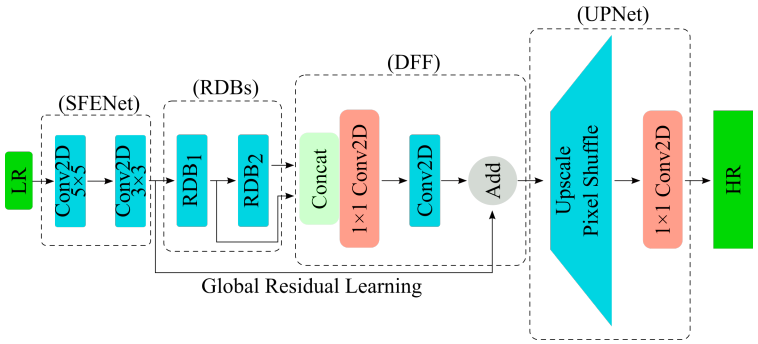

Figure 4.27: Implemented Residual Dense Network architecture.

Shallow Feature Extraction Net (SFENet) which consists of two cascaded convolutional layers responsible for extracting shallow features from the original LR input. Then, the extracted features from SFENet are transferred to the segment of RDBs in which two RDBs were utilised.

The third segment is the Dense Feature Fusion (DFF) which is responsible for fusing features that include global feature fusion and global residual learning. The purpose of global feature fusion is to learn global hierarchical features holistically. Hence, DFF fully utilise all features from all preceding segments.

The last segment in the model is the Up-Sampling Net (UPNet), in which I applied the pixel shuffle technique [166]. Further, the pixel shuffle performs sub-pixel convolution

operation that is responsible to reshape its input tensor by rearranging the elements $(H \times W \times r^2)$ to $(rH \times rW \times 1)$, where H is the height, W is the width, (r^2) is total number of channels, and r is the up-scaling factor. Accordingly, the number of channels at the last layer (output from DFF segment) must equal $C.r^2$ for the total number of pixels in order to match the HR image to be obtained. Hence, the up-scaling factor r equals to 16, as our aim is to obtain HR output image of size (512×512) from the LR input image of size (32×32). Figure 4.28 illustrates the process of the sub-pixel convolution layer as it is made up of two steps: a general convolutional operation and pixel rearrangement. Further, it works through combining each pixel on multiple-channel feature maps into one $(r \times r)$ square area in the output image. Therefore, each pixel on feature maps is equivalent to the sub-pixel on the generated output image. The final convolutional layer has 1 filter of size (1×1), which will produce 1 output channel as the HR images are in grayscale.

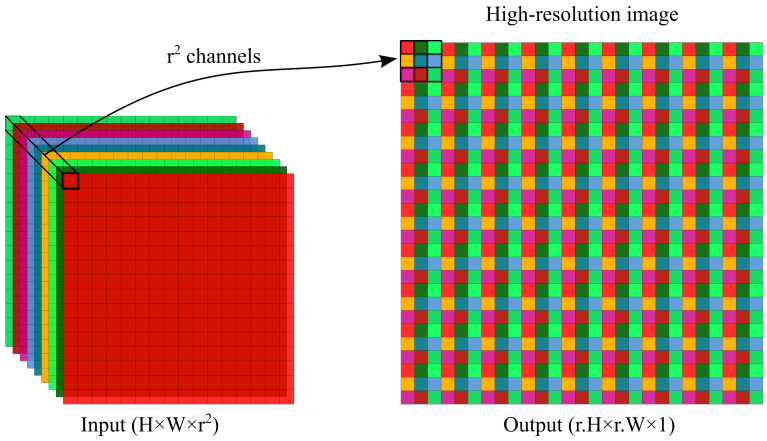

Figure 4.28: Sub-pixel convolution layer.

Furthermore, Fig. 4.29 presents the plot of the training loss and validation loss values with respect to epochs during the training phase for the DLSR model. The number of epochs for the DLSR model was set to 250. As shown in the Fig. 4.29, the developed AE-ConvLSTM model converges, and it has no signs of overfitting or underfitting.

4.7 Summary

Full wavefield acquired by SLDV of propagating Lamb waves in a CFRP plate contains beneficial information concerning the investigated specimen, such as the discontinuities (i.e., delamination and boundaries) with which the waves interact. Hence, distinct patterns of wave reflection appear regarding different delamination locations, sizes, and shapes. Such distinct patterns can be learned by deep learning methods to identify the

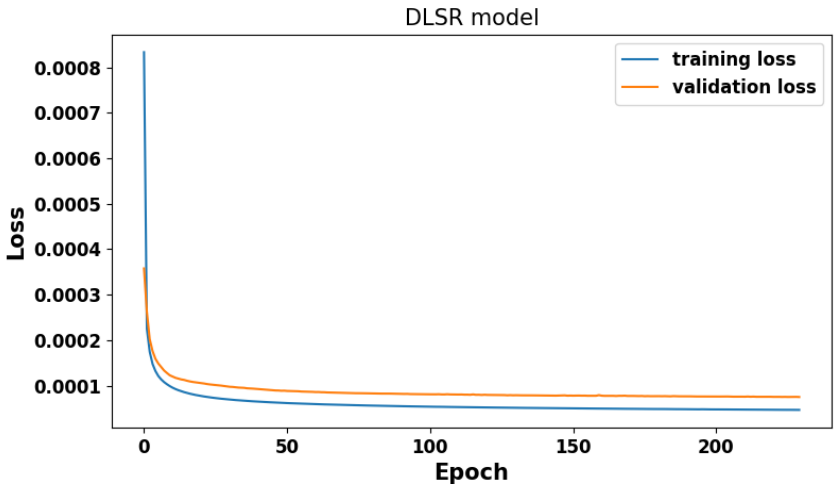

Figure 4.29: DLSR model: training and validation losses during training phase.

delamination. Accordingly, a large dataset of 475 cases of a full wavefield of propagating Lamb waves in a CFRP plate interacting with delaminations with random locations, shapes, and sizes was generated. The developed deep learning methods offer an end-to-end approach to damage identification. The first developed model was a CNN classifier, which can localise the delamination with a bounding box around it. The developed CNN classifier was trained on RMS images of the full wavefield. The second utilised approach was pixel-wise image segmentation, in which I developed five FCN models that are capable of identifying the delamination. The FCN models were also trained on RMS images of the full wavefield. For the next developed model, I took a further step in which I directly utilised the full wavefield frames of propagating Lamb waves in an end-to-end deep learning model. Finally, in the last developed model (DLSR), I attempted to reconstruct a high-resolution full wavefield from spatially sparse measurements. Accordingly, the measurement time required to obtain the full wavefield by the SLDV is reduced significantly. Consequently, the recovered full wavefield frames that result from the DLSR model can be utilised to identify the damage.

Chapter 5

Results and Discussions

In this chapter, the results and discussions regarding delamination identification in CFRP plates are presented. Accordingly, to verify the developed DL models, I evaluated them on 95 unseen numerical test cases and further on experimental test cases. Moreover, I have selected four numerical test cases to present. The selected four numerical cases were chosen to represent the random distribution of delamination locations.

Furthermore, I have applied the super-resolution image reconstruction technique to LR full wavefield animations for both the numerical test cases and the experimental case. Then, I applied the AE-ConvLSTM model to the reconstructed frames in order to identify the delamination.

Accordingly, to evaluate the performance of the proposed models, the intersection over union IoU (Jaccard index) was applied as the accuracy metric. IoU is estimated by determining the intersection area between the ground truth and the predicted output. Furthermore, we have two output classes (damaged and undamaged). The IoU was calculated for the damaged class only. The illustration of the IoU metric is presented in Fig. 5.1 where Eqn. (5.1) defines the IoU metric:

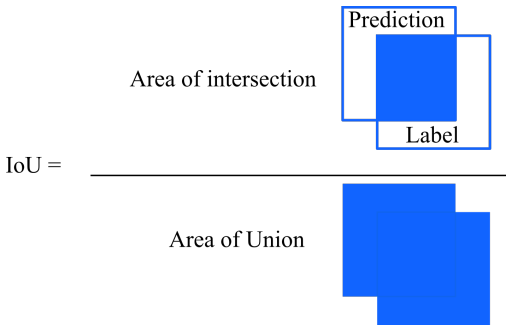

Figure 5.1: Intersection over union.

$$\text{IoU} = \frac{Intersection}{Union} = \frac{\hat{Y} \cap Y}{\hat{Y} \cup Y}, \tag{5.1}$$

where $\hat{Y}$ is the predicted output, and Y is the ground truth (label).

Additionally, the percentage area error ϵ depicted in Eqn. (5.2) was utilised to evaluate the performance of the FCN models and the Autoencoder ConvLSTM model:

$$\epsilon = \frac{|A - \hat{A}|}{A} \times 100\%, \tag{5.2}$$

where A and $\hat{A}$ refer to the area in mm^2 of the damage class in the ground truth and the predicted output, respectively. Such a metric can indicate how close the area of the predicted delamination is to the ground truth. Accordingly, the lower the value of ϵ, the higher the accuracy of the identified damage.

Two metrics are utilised for evaluating the DLSR model developed to perform super-resolution image reconstruction of the full wavefield. The first metric is the peak signal-to-noise ratio (PSNR), which refers to the maximum possible power of a signal and the power of the distorting noise that affects the quality of its representation. Equation (5.3) depicts the mathematical representation of the PSNR:

$$PSNR = 20 \log_{10} \left(\frac{R}{\sqrt{MSE}} \right), \tag{5.3}$$

where R represents the maximum fluctuation value that exists in the input image, and its equal to 255, as I used an 8-bit unsigned integer data type. MSE refers to the mean square error between the predicted output and the corresponding ground truth (see Eqn. 4.2).

The second utilised metric is the Pearson correlation coefficient that measures the linear relationship between two variable matrices X (represents the ground truth values) and Y (represents the predicted values), and its value is between -1 and 1, where:

- -1 represents a perfect negative linear correlation,
- 0 represents no linear correlation,
- 1 represents a perfect positive linear correlation.

Equation 5.4 depicts the mathematical formula to calculate Pearson CC commonly denoted as r_{xy}:

$$r_{xy} = \frac{\sum_{i=1}^{n}(x_i - \bar{x})(y_i - \bar{y})}{\sqrt{\sum_{i=1}^{n}(x_i - \bar{x})^2}\sqrt{\sum_{i=1}^{n}(y_i - \bar{y})^2}}, \tag{5.4}$$

where n is the number of sample points, x_i, y_i are the individual value points representing the ground truth and predicted values, respectively, and $\bar{x}$ is the mean value of the sample, analogously to $\bar{y}$.

In the following, I will present and discuss the results of the developed CNN classifier models in section 5.1. In section 5.2, the results of the five developed FCN models will

be presented and discussed. Accordingly, a comparison between the developed FCN models will be made. In section 5.3, the results and discussion regarding the developed AE-ConvLSTM model are presented. Finally, in section 5.4, I will present the results of applying the developed DLSR model to numerical cases to identify the damage in the reconstructed frames. Furthermore, I will apply the DLSR model to an experimental scenario to identify the delamination.

5.1 Predictions of CNN classifier models

In this section, I present the predicted outputs of utilising the CNN classifier on the selected four RMS numerical cases (from the top of the plate), which have delaminations of different locations, shapes, and angles.

In the first numerical case, the delamination is located at left edge of the plate, as shown in Fig. 5.2a, representing its ground truth (GT). The predicted output using (14×14) and (16×16) patches are presented in Fig. 5.2b and Fig. 5.2c. For the second numerical case, the delamination is located at upper left corner of the plate, as shown in Fig. 5.2d, representing its ground truth (GT). The predicted output using (14×14) and (16×16) patches are presented in Fig. 5.2e and Fig. 5.2f. In third numerical case, the delamination is located near to the center upper edge of the plate, as shown in Fig. 5.2g, representing its ground truth (GT). The predicted output using (14×14) and (16×16) patches are presented in Fig. 5.2h and Fig. 5.2i. It is important to notice that the first, second and the third cases are considered difficult due to the edge wave reflections that have the similar patterns as delamination reflection. However, the CNN classifiers were able to detect the delamination in such difficult cases. For four numerical case, the delamination is located in the upper left quarter of the plate, as shown in Fig. 5.2j, representing its ground truth (GT). The predicted output using (14×14) and (16×16) patches are presented in Fig. 5.2k and Fig. 5.2l.

Table 5.1 presents the IoU values for CNN classier with respect to the input patch size for the numerical cases shown in Fig. 5.2. Furthermore, the mean IoU for all 95 test cases is (0.16) and (0.2) for (14×14) and (16×16) patches, receptively. Consequently, it can be concluded that when increasing the input resolution (i.e., using (16×16) patches), the obtained IoU values increased. It should also be mentioned, that for both input patches, the CNN classifier was able to detect all the delaminations for the 95 test cases.

Moreover, the CNN classifier model was tested on experimental data, however, due to the poor quality of the obtained results, I did not present them.

Table 5.1: IoU values of numerical cases.

Case	Patches	
	(14×14)	(16×16)
1	0.26	0.34
2	0.18	0.23
2	0.07	0.04
4	0.12	0.24

5.2 Predictions of FCN pixel-wise segmentation models

5.2.1 Numerical cases

In this section, five FCN models, including Res-UNet, VGG16 encoder-decoder, FCN-DenseNet, PSPNet, and GCN, were evaluated on four selected damage cases of an RMS (from the bottom surface of the plate).

The first exemplary delamination case is shown in Fig. 5.3. The delamination is located at the left edge of the plate, and it is surrounded by a line to represent its shape and location as shown in Fig. 5.3a. Figures 5.3b- 5.3f show the predicted output of the Res-UNet, VGG16 encoder-decoder, PSPNet, FCN-DenseNet and GCN models, respectively. All models properly indicate the location of the delamination. Moreover, pixels related to delamination location are clustered into a single spot without any additional noise. The GCN model better visually resembles the actual shape of the delamination than other models.

In the second delamination case, shown in Fig. 5.4, the delamination is located at the upper left corner of the plate, and it is surrounded by an ellipse to represent its shape and location as shown in Fig. 5.4a. This is the most challenging damage scenario because of reflections coming from plate edges overshadows reflections from damage. As a result, changes in RMS patterns are barely visible. Figures 5.4b - 5.4f show the predicted output of the Res-UNet, VGG16 encoder-decoder, PSPNet, FCN-DenseNet and GCN models, respectively. In this delamination case the PSPNet model were not able to identify the damage. However, the rest models perform reasonably well, considering the difficult damage scenario.

The third delamination case is shown in Figure 5.5. The delamination is located at the upper middle of the plate and it is surrounded by an ellipse to represent its shape and location as shown in Fig. 5.5a. Figures 5.5b - 5.5f show the predicted output of the Res-UNet, VGG16 encoder-decoder, PSPNet, FCN-DenseNet and GCN models, respectively. In this case, the elliptical shape of delamination is best preserved by Res-UNet and FCN-DenseNet.

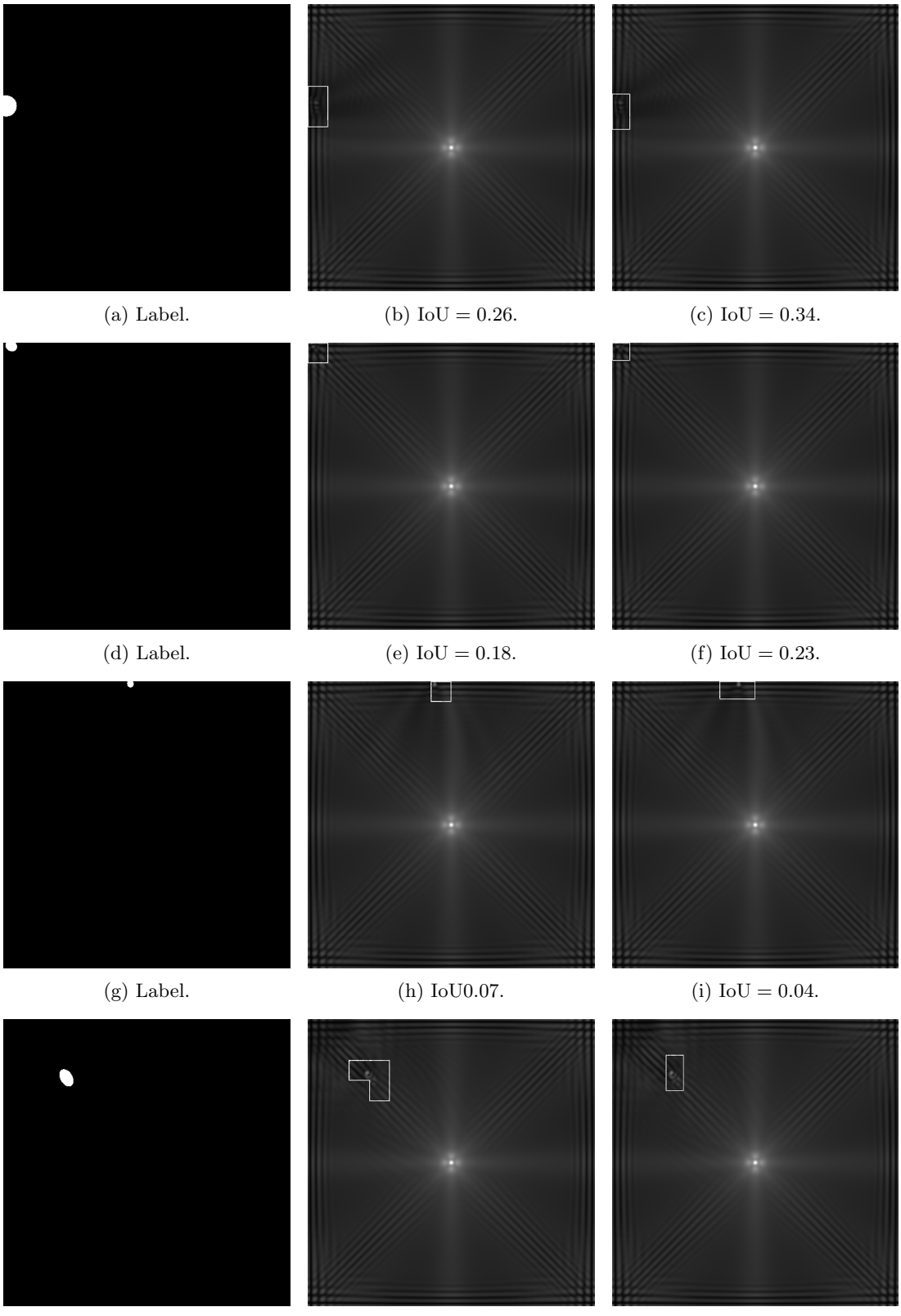

(a) Label. (b) IoU = 0.26. (c) IoU = 0.34.

(d) Label. (e) IoU = 0.18. (f) IoU = 0.23.

(g) Label. (h) IoU0.07. (i) IoU = 0.04.

(j) Label. (k) IoU = 0.12. (l) IoU = 0.24.

Figure 5.2: Output predictions for the implemented CNN classifiers.

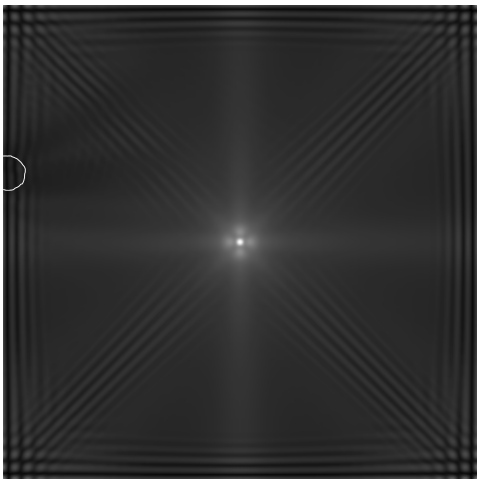

(a) RMS & Label.

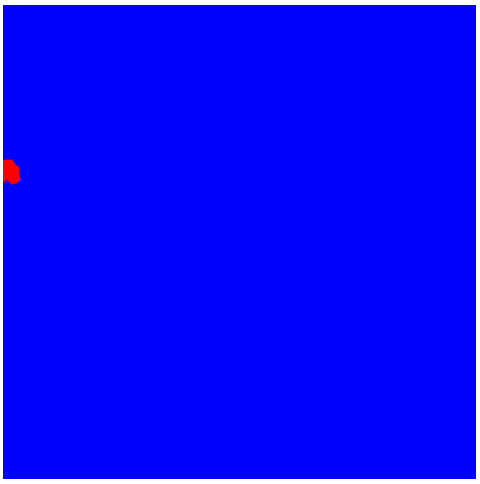

(b) Res-UNet.

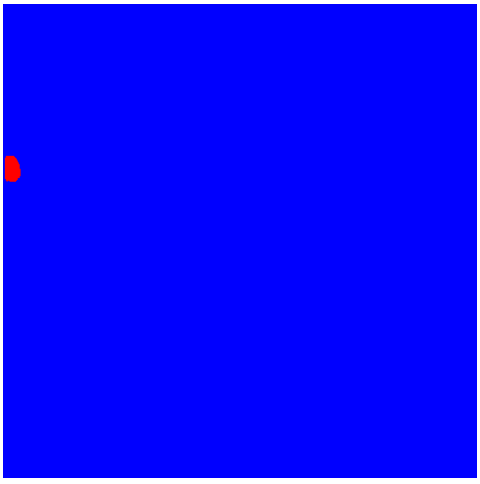

(c) VGG16 encoder-decoder.

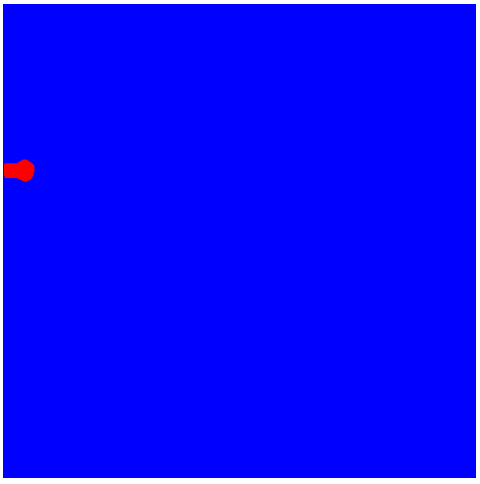

(d) PSPNet.

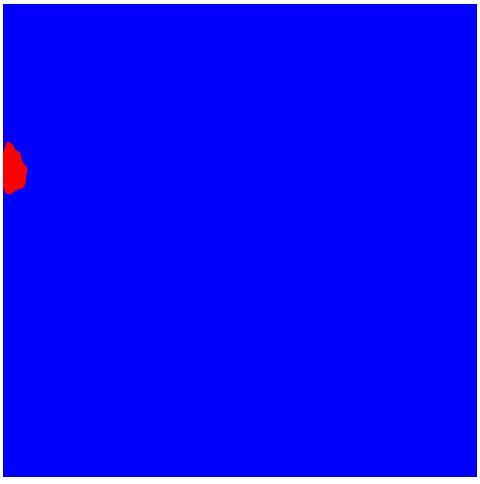

(e) FCN-DenseNet.

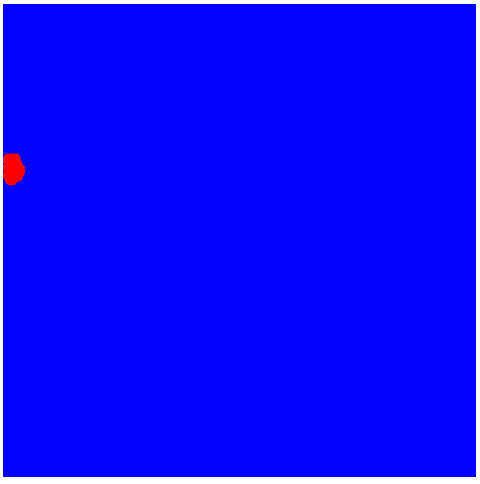

(f) GCN.

Figure 5.3: First delamination case based on numerical data.

In the fourth delamination case, shown in Fig. 5.6, the delamination is located at the upper left quarter of the plate, and it is surrounded by an ellipse to represent its shape and location as shown in Fig. 5.6a. Figures 5.6b - 5.6f show the predicted output of

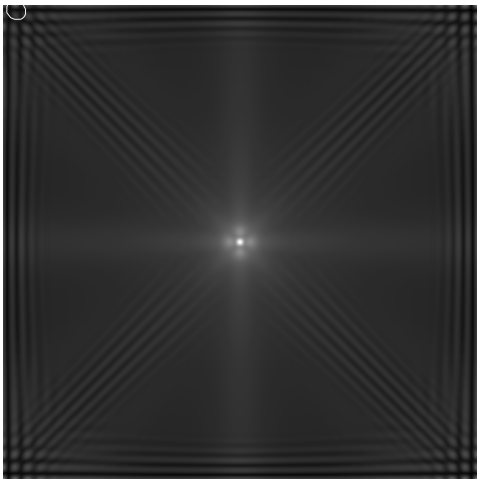

(a) RMS & Label.

(b) Res-UNet.

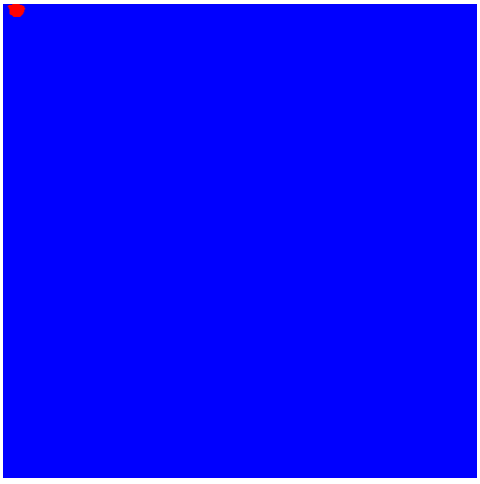

(c) VGG16 encoder-decoder.

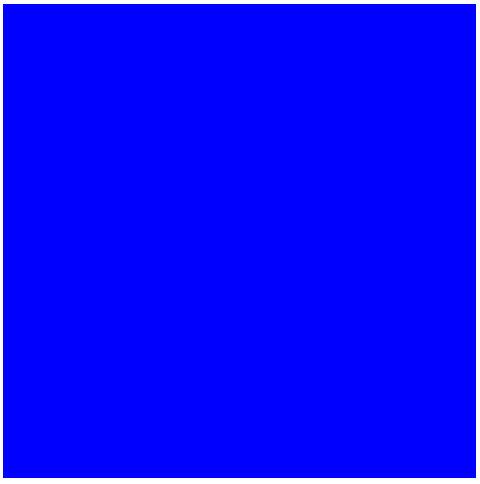

(d) PSPNet.

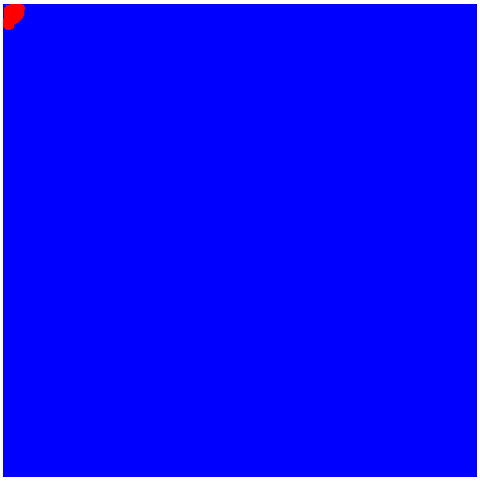

(e) FCN-DenseNet.

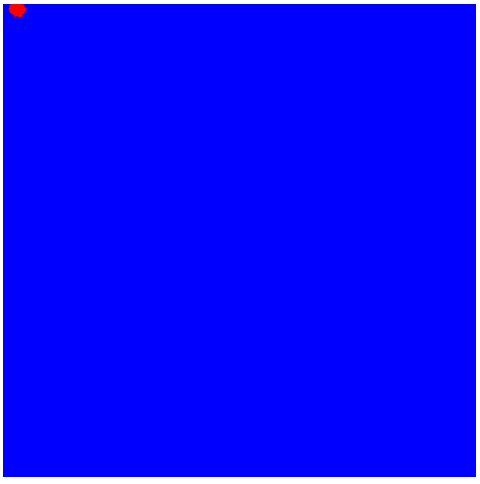

(f) GCN.

Figure 5.4: Second delamination case based on numerical data.

the Res-UNet, VGG16 encoder-decoder, PSPNet, FCN-DenseNet and GCN models, respectively. All models perform reasonably well for this damage case.

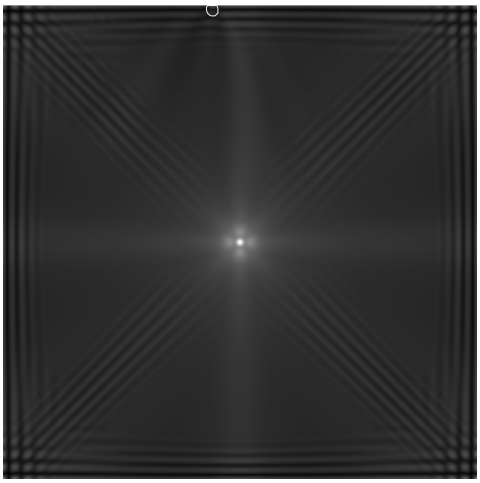

(a) RMS & Label.

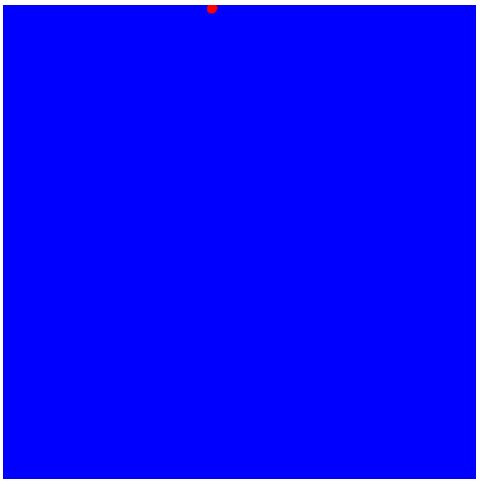

(b) Res-UNet.

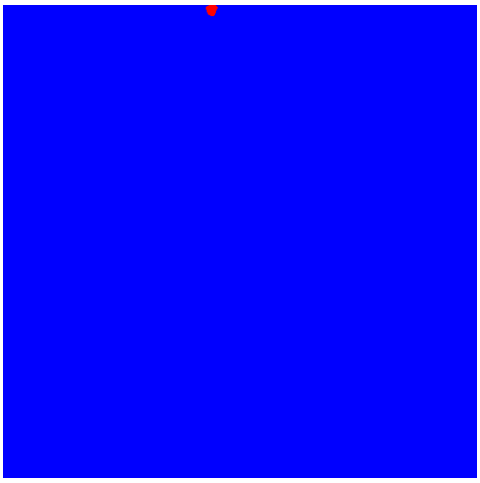

(c) VGG16 encoder-decoder.

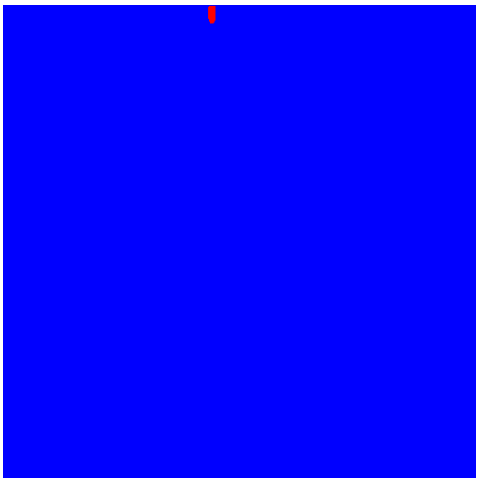

(d) PSPNet.

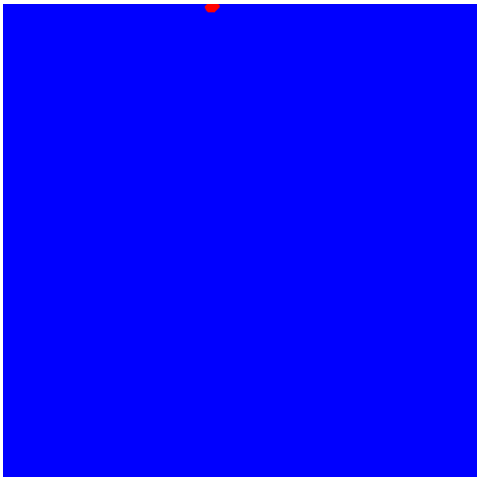

(e) FCN-DenseNet.

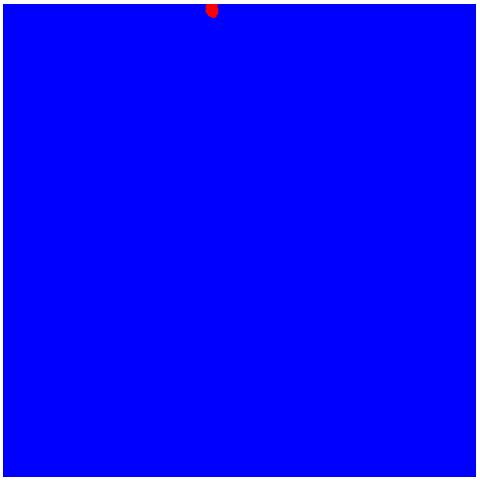

(f) GCN.

Figure 5.5: Third delamination case based on numerical data.

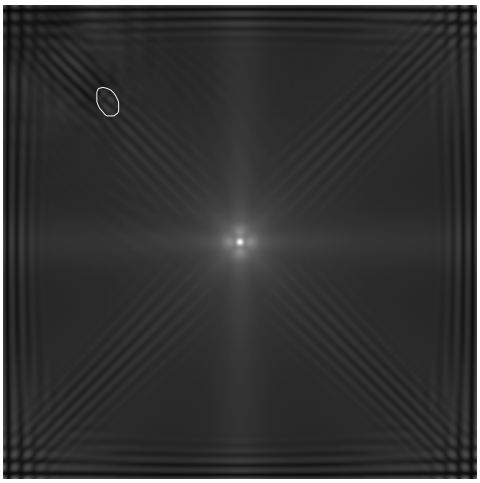

(a) RMS & Label.

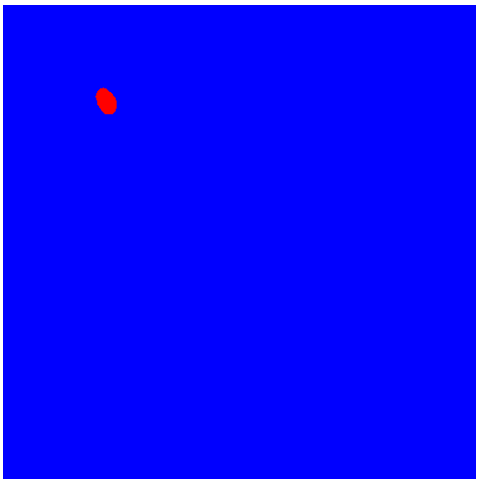

(b) Res-UNet.

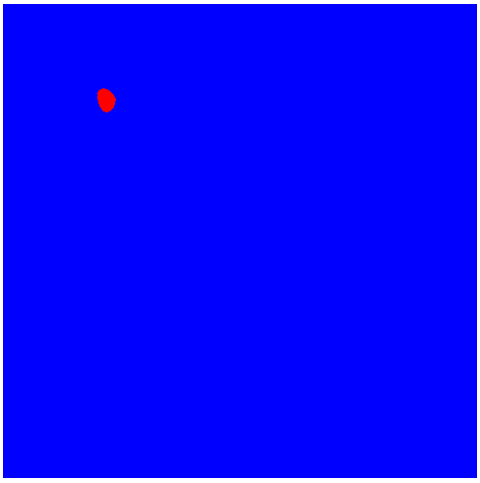

(c) VGG16 encoder-decoder.

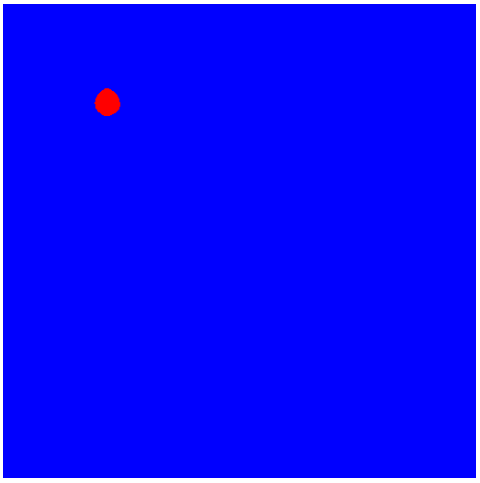

(d) PSPNet.

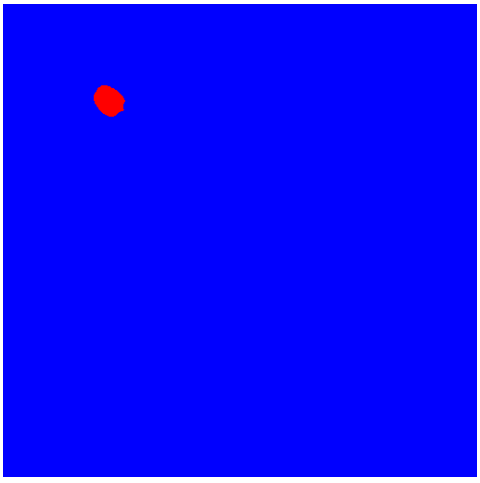

(e) FCN-DenseNet.

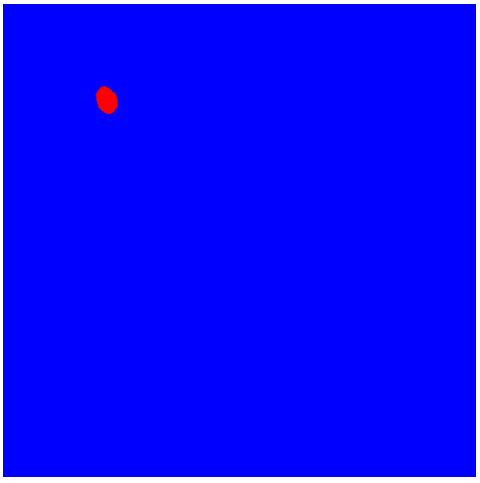

(f) GCN.

Figure 5.6: Fourth delamination case based on numerical data.

Table 5.2 presents the evaluation metrics for all FCN models, regarding the numerical cases shown in Figs. 5.3, 5.4, 5.5, and 5.6. Table 5.2 gathers the actual delamination area A, predicted delamination area $\hat{A}$, intersection over union IoU and percentage area error ϵ with respect to each case. The overall performance of the GCN model is better than other models for the selected delamination scenarios.

Table 5.2: Evaluation metrics of the four numerical cases.

Model	case number	A [mm^2]	Predicted output		
			IoU	$\hat{A}$ [mm^2]	ϵ
Res-UNet	1	717	0.50	402	43.93%
	2	257	0.45	143	44.36%
	3	105	0.67	88	16.19%
	4	537	0.80	478	10.99%
VGG16 encoder-decoder	1	717	0.51	410	42.82%
	2	257	0.69	203	21.01%
	3	105	0.75	117	11.43%
	4	537	0.65	385	28.31%
FCN-DenseNet	1	717	0.73	1073	49.65%
	2	257	0.52	505	96.50%
	3	105	0.66	118	12.38%
	4	537	0.72	815	51.77%
PSPNet	1	717	0.39	596	16.88%
	2	257	0.00	0	−%
	3	105	0.44	156	48.57%
	4	537	0.77	610	13.59%
GCN	1	717	0.79	666	7.11%
	2	257	0.71	215	16.34%
	3	105	0.72	177	68.57%
	4	537	0.86	523	2.61%

Table 5.3 presents the mean and maximum values of IoU calculated for the previously unseen numerical test set for all FCN models. Table 5.3 shows that all models have a relatively high IoU, indicating their ability to detect and localise the delamination.

Table 5.3: Analysis of numerical cases.

Model	mean IoU	max IoU
Res-UNet	0.66	0.89
VGG16 encoder-decoder	0.57	0.84
FCN-DenseNet	0.68	0.92
PSPNet	0.55	0.91
GCN	0.76	0.93

5.2.2 Experimental cases

In this section, FCN models are evaluated using experimentally acquired data. Similarly to the synthetic dataset, we applied a frequency of 50 kHz to excite a signal in a transducer placed at the centre of the plate. $A0$ mode wavelength for this particular CFRP material at such frequency is about 19.5 mm. The measurements were performed by using Polytec PSV-400 SLDV on the bottom surface of the plate with dimensions of 500×500 mm. The measurements were conducted on a regular grid of 333×333 points. The measurement area was aligned with the plate edges. The sampling frequency was 512 kHz. The experimental case is for a CFRP specimen with a single delamination. A plain weave fabric reinforcement was used for manufacturing the composite specimen. The delamination between layers of the fabric was created artificially by a Teflon insert of a thickness 250 μm. The Teflon of a square shape was inserted during specimen manufacturing, so its shape and location are known. The number of full wavefield frames for this case is $f_n = 256$. Furthermore, the measured full wavefield was further processed by an energy compensated RMS which takes into account wave attenuation. The results of such operation are shown in Fig. 5.7a. The delamination is surrounded by a square frame representing its shape and location. Figures (5.7b - 5.7f) shows delamination prediction maps for Res-UNet, VGG16 encoder-decoder, PSPNet, FCN-DenseNet and GCN models, receptively.

Table 5.4 presents the evaluation metrics for all FCN models, regarding the experimental case shown in Figs. 5.7. Table 5.4 gathers the actual delamination area A, predicted delamination area $\hat{A}$, intersection over union IoU and percentage area error ϵ with respect to each FCN model. The overall performance of the GCN model is better than other models for the selected delamination scenarios. Similarly to the numerical dataset, the best accuracy was achieved by using GCN.

Table 5.4: Evaluation metrics of the experimental case.

Model	A [mm^2]	Predicted output		
		IoU	$\hat{A}$ [mm^2]	ϵ
Res-UNet	210	0.58	323	53.8%
VGG16 encoder-decoder		0.62	320	52.4%
FCN-DenseNet		0.54	386	83.8%
PSPNet		0.49	580	176.2%
GCN		0.72	309	47.1%

It should be noted that the developed FCN-DenseNet model presented in [164] was compared to the conventional adaptive wavenumber filtering method presented in [44, 47].

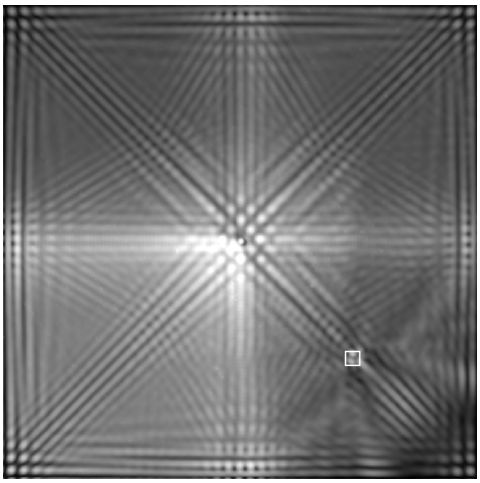

(a) ERMS CFRP Teflon inserted & Label.

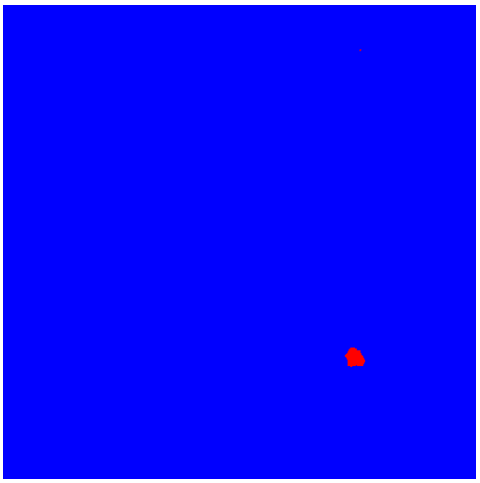

(b) Res-UNet.

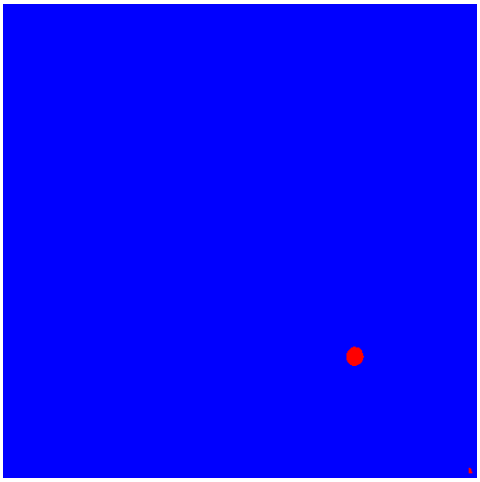

(c) VGG16 encoder-decoder.

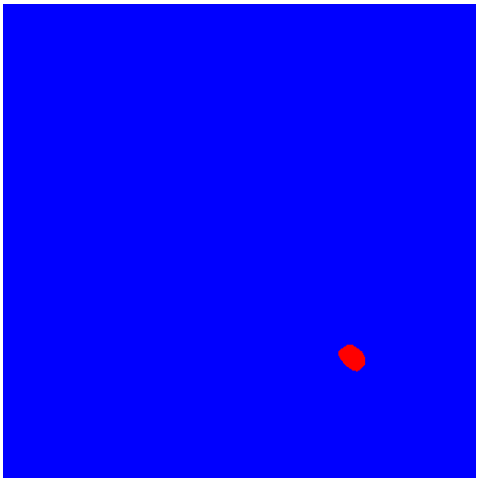

(d) PSPNet.

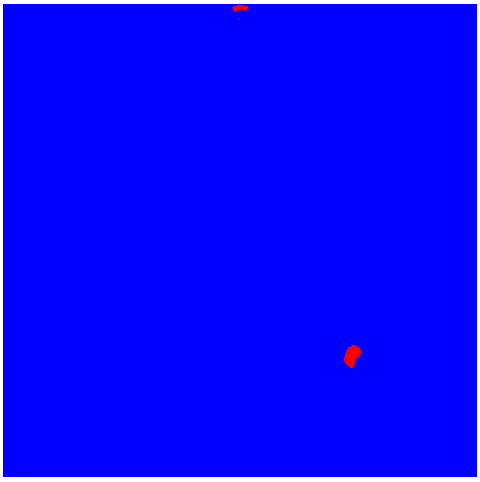

(e) FCN-DenseNet.

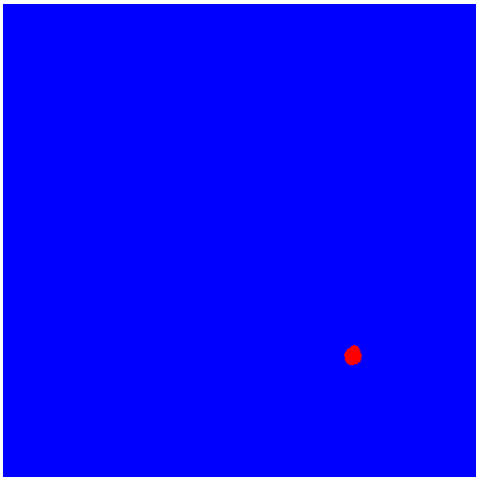

(f) GCN.

Figure 5.7: Fourth delamination case based on numerical data.

The FCN models show good generalisation behaviour in predicting the delamination in the unseen numerically generated data. We can observe that the models can identify delamination with nearly no noise, indicating that the models can generalize and detect

delamination on previously unseen data. It has been shown that the achieved accuracy of the FCN models presented in [167] surpasses the accuracy of previous models in [164] with an improvement of 22.47%. Given that the provided models were only trained on a numerically generated dataset, they had a high degree of generalisation. Additionally, the models show their ability to generalise by detecting the delamination in the experimentally acquired data.

Figure 5.8 presents a comparison between the predicted outputs regarding the experimental case with the adaptive wavenumber filtering presented in [44, 47] and the two versions of the developed FCN-DenseNet models presented in [164] and [167], respectively. Figure. 5.8a shows the damage map represents the energy-based root mean square index of frames filtered in the wavenumber domain (ERMSF). To eliminate low values from the ERMSF, a binary threshold is applied as shown in Fig. 5.8b. The threshold level was set to minimise the influence of edge noise while still highlighting the damage. The calculated IoU equals 0.401. Figure. 5.8c shows the predicted output for the developed FCN-DenseNet model in [164], and the calculated IoU equals 0.081. Fig. 5.8d shows the predicted output of the improved FCN-DenseNet model developed in [167], and the calculated IoU equals to 0.54. Accordingly, the improved version of the FCN-DenseNet model developed in [167] surpasses both the adaptive wavenumber filtering method and the FCN-DenseNet model developed in [164].

5.3 Predictions of autoencoder ConvLSTM model

In this section, the evaluation of the developed AE-ConvLSTM model will be presented on the numerical test data and, further, on the experimental data to demonstrate its capability to predict delamination location, shape, and size. Hence, the four representative damage cases were selected from the numerical dataset to show the performance of the developed models. For numerical cases, it should be noted that the predicted results were obtained using only the first window of frames after the interaction with the damage, as the delamination ground truths are provided, which is not the case for real-life scenarios as in the experimental section. As a result, I skipped the task of producing intermediate predictions and further calculating the RMS image because the predicted results show the highest IoU achieved across all possible sliding window positions (see Fig. 4.20).

5.3.1 Numerical cases

For the numerical cases, the same delamination cases were selected as previously. In the first numerical case, the delamination is located at left edge of the plate,

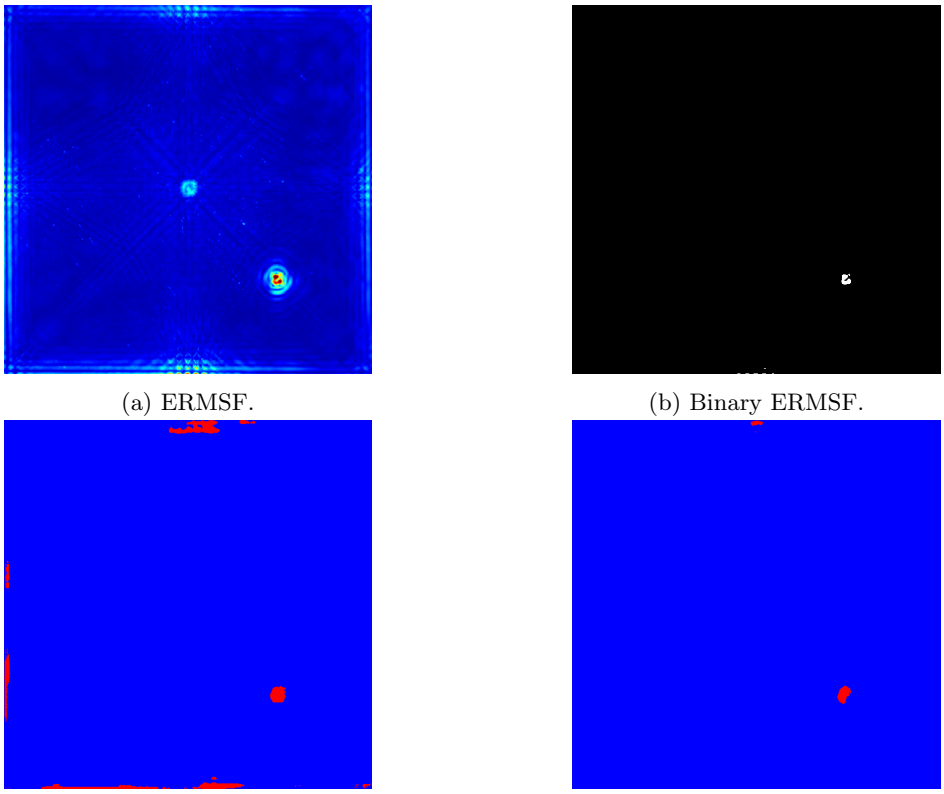

(a) ERMSF. (b) Binary ERMSF.

(c) FCN-DenseNet [164] (d) FCN-DenseNet [167]

Figure 5.8: Comparsion of the experimental case by using the adaptive wavenumber filtering method [44, 47], FCN-DenseNet [164], FCN-DenseNet [167].

as shown in Fig. 5.9a, representing its ground truth (GT). The predicted output of the AE-ConvLSTM model is shown in Fig. 5.9b In the second numerical test case, the delamination is located at the left upper corner of the plate, as shown in Fig. 5.9c, which represents the GT. This case is also considered difficult due to the waves reflected from the edges have similar patterns to those reflected from the delamination. Figure 5.9d shows predicted damage map of AE-ConvLSTM model. In the third case, the delamination is located in the upper centre of the edge as shown in Fig. 5.9e, representing the GT. Figure 5.9f shows the predicted output of this case. The fourth test case has a delamination located upper left quarter as shown in Fig. 5.9g representing the GT. The predicted damage map of this case is presented in Fig. 5.9h.

As shown in all predicted damage maps, the developed AE-ConvLSTM model can accurately identify the shape, size , and location of the delamination without any noise regardless of how difficult the test case is.

Table 5.5 presents the evaluation metrics for AE-ConvLSTM model regarding the numerical cases shown in Fig. 5.9. Table 5.5 gathers the actual delamination area A, predicted delamination area $\hat{A}$, intersection over union IoU and percentage area error ϵ with respect to each case.

Table 5.5: Evaluation metrics of the four numerical cases.

case number	A [mm^2]	Predicted output		
		IoU	$\hat{A}$ [mm^2]	ϵ
1	717	0.78	613	14.5%
2	257	0.53	171	33.46%
3	105	0.94	106	0.95%
4	537	0.94	549	2.23%

Table 5.6 presents a comparison of the mean (IoU) for 95 numerical test cases with respect to the DL models. As shown in Table 5.6, AE-ConvLSTM model takes as input animations of the full wavefields, whereas the rest models presented in [164, 167] take as input RMS images. As anticipated, the IoU value when taking animations as an input outperforms that when taking only the RMS images as input.

Table 5.6: Mean IoU for numerical cases with respect to the input of the model.

Input	Model	mean IoU
Animations	Autoencoder ConvLSTM	0.87
RMS images	FCN-DenseNet [164]	0.62
	FCN-DenseNet [167]	0.68
	GCN [167]	0.76

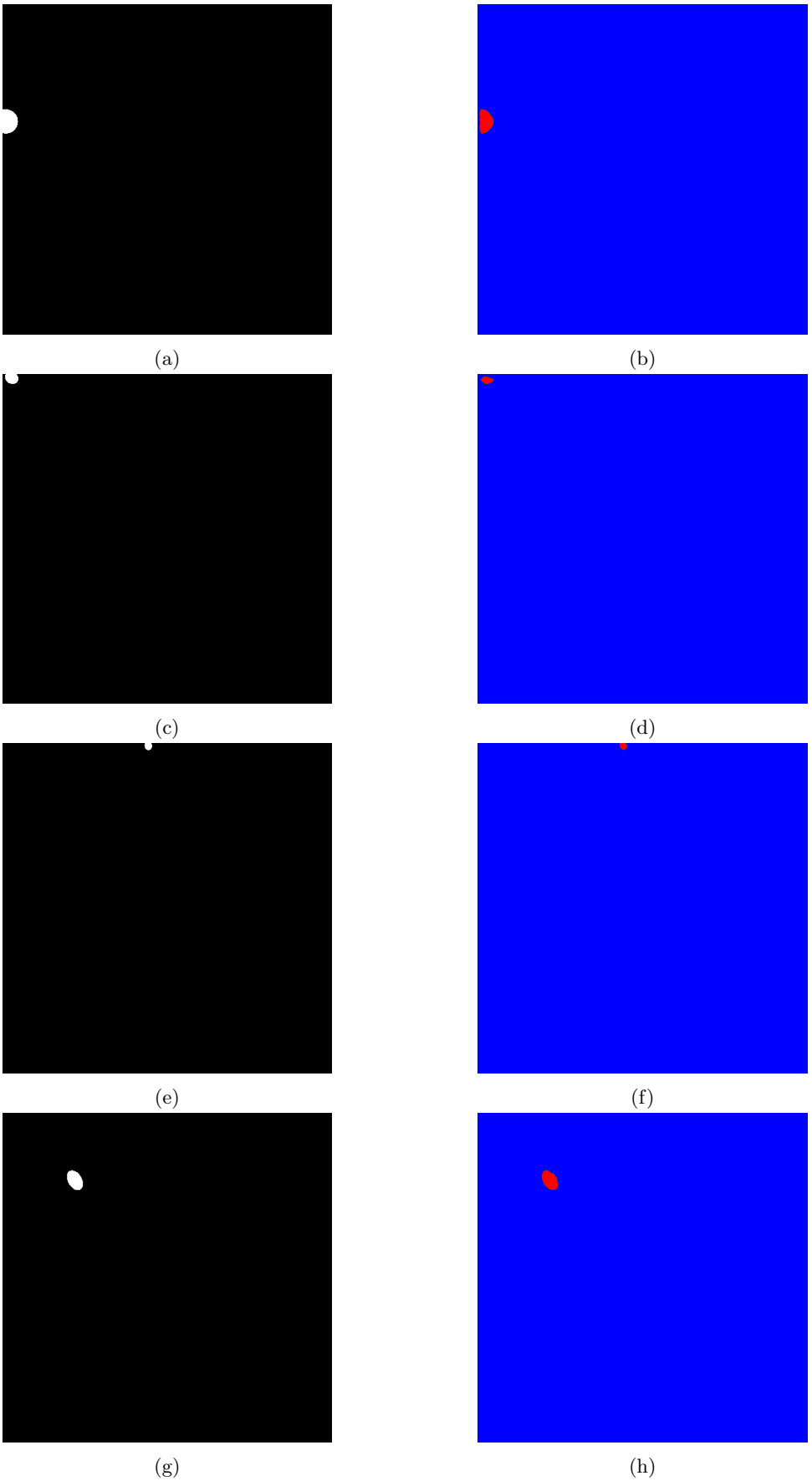

Figure 5.9: Four delamination cases based on numerical data (AE-ConvLSTM).

5.3.2 Experimental cases

Single delamination

In this section, the investigation of AE-ConvLSTM model using experimentally acquired data of a single delamination case presented in subsection. 5.2.2 is presented. The Teflon of a square shape was inserted during specimen manufacturing, so its shape and location are known. Based on that, the ground truth was prepared manually and it is shown in Fig. 5.10a. Furthermore, the number of full wavefield frames for this case is $f_n = 256$. Figure 5.10b shows the predicted output of the AE-ConvLSTM model for a window of frames $(72 - 96)$ for which the highest IoU $= 0.47$ was achieved. Furthermore, the percentage area error metric ϵ for AE-ConvLSTM model was equal to 86.67%.

It should be noted that for the same damage scenario, the IoU value for the models developed previously in [164] was low (IoU $= 0.081$).

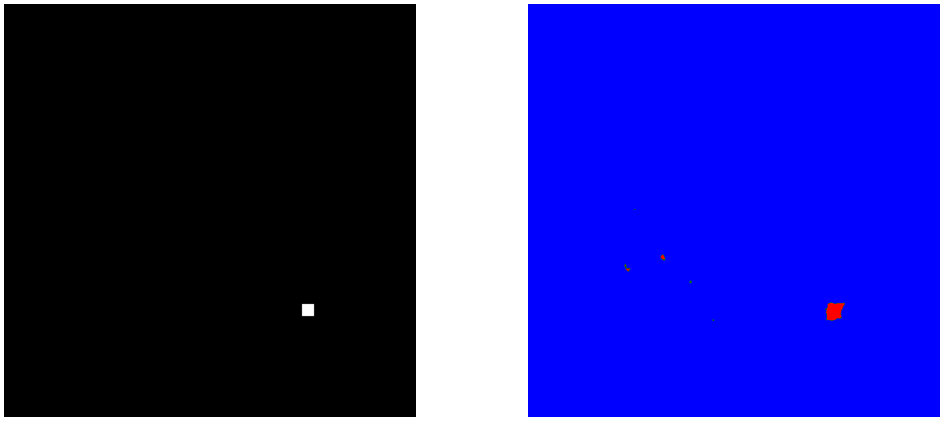

(a) GT of Teflon insert. (b) IoU = 0.47.

Figure 5.10: Experimental case: single delamination of Teflon insert.

The predictions were highest for the window of frames corresponding to the first interaction of the guided waves with the delamination. Hence, such frames contain the most valuable feature patterns regarding delamination. This behaviour is depicted in Fig. 5.11, which shows the IoU values with respect to the predicted outputs as I slide the window over all input frames from the starting frame till the end. Since there are 256 frames of full wavefield in this damage case, there are 232 windows. Consequently, the AE-ConvLSTM model has 232 consecutive predictions. Furthermore, in Fig. 5.11a three places for the sliding window were selected. The first place depicted in a dark blue star shown in Fig. 5.11b represents a window centered at frame $f_n = 84$, which correspond to the initial interaction of guided waves with the delamination. The second place is depicted in the pink pentagon shape shown in Fig. 5.11b which represents a

window centered at frame $f_n = 141$ corresponding to guided waves reflected from the boundaries. We can notice the drop in the IoU values as these frames have fewer damage features. The third place, depicted in the green circle shown in Fig. 5.11b represents a window centered at frame $f_n = 218$ corresponding to the interaction of guided waves reflected from the edges with the delamination. As we can see, the value of IoU increases again as the valuable feature patterns regarding delamination start to appear again.

The predicted outputs of AE-ConvLSTM model for windows centered at frame 84 (the dark blue star), frame 141 (pink pentagon), and frame 218 (the green circle) are shown in Fig. 5.12. Apart from correctly identified delamination, some noise is obtained near edges of the specimen.

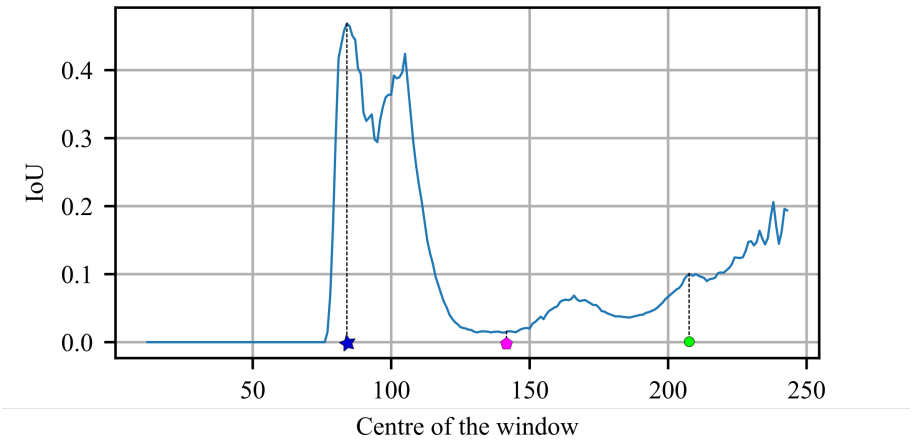

(a) IoU for the sliding window centered at consecutive frames.

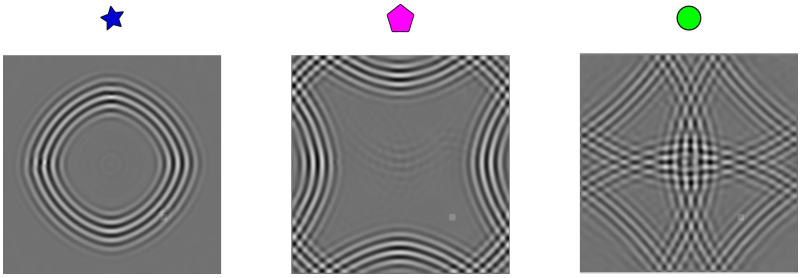

(b) Corresponding frames of guided waves.

Figure 5.11: IoU for the sliding window of frames (Teflon insert-single delamination).

Figure show the RMS image for the experimental case of single delamination predicted the AE-ConvLSTM model. Additionally, to separate undamaged and damaged classes from the RMS images, we applied a binary threshold with a value ($threshold = 0.5$) as shown in Fig 5.13b. The threshold level was selected to limit the influence of noise and, at the same time, highlight the damage. The calculated IoU values for the case of single delamination is IoU= 0.42.

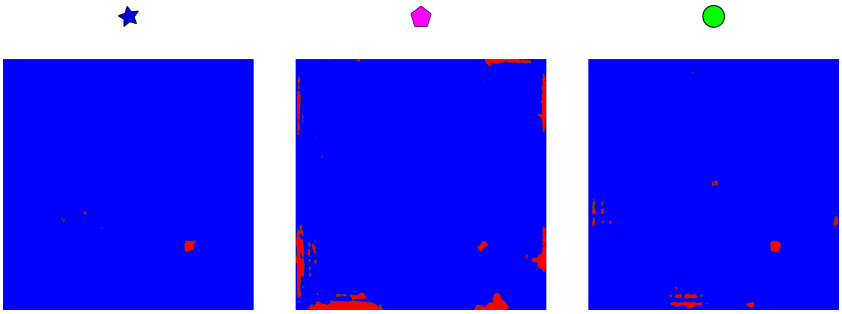

Figure 5.12: Predictions for window centered at selected frames (Teflon insert - single delamination).

Table 5.7 presents the evaluation metrics for the AE-ConvLSTM model regarding the experimental case of single delamination shown in Fig. 5.13b. As shown in Table 5.7, the actual A and predicted areas $\hat{A}$ of delaminations were computed in [mm^2] with respect to each case. The percentage area error ϵ was calculated for both models accordingly.

Table 5.7: Evaluation metrics for experimental case of single delamination.

Experimental case	A [mm^2]	AE-ConvLSTM model		
		IoU	$\hat{A}$ [mm^2]	ϵ
Single delamination	225	0.42	420	86.67%

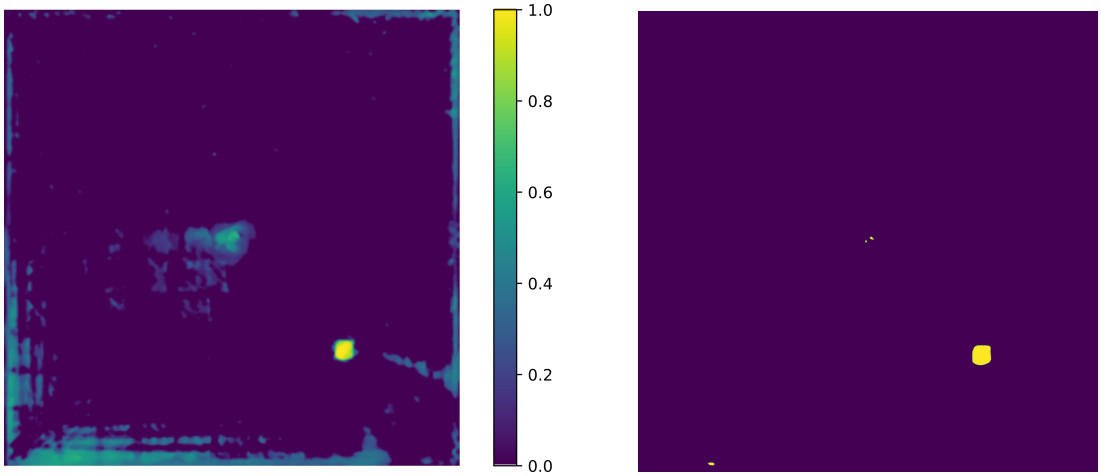

(a) RMS image (damage map). (b) Thresholded RMS image.

Figure 5.13: Teflon insert - single delamination.

Multiple delaminations

In the second experimental case, we investigated three specimens of carbon/epoxy laminate reinforced by 16 layers of plain weave fabric as shown in Fig. 5.14. Teflon inserts with a thickness of 250 μm were used to simulate the delaminations. The prepregs GG 205 P (fibres Toray FT 300–3K 200 tex) by G. Angeloni and epoxy resin IMP503Z-HT by Impregnatex Compositi were used for the fabrication of the specimen in the autoclave. The average thickness of the specimen was 3.9 ± 0.1 mm.

In Specimen II, three large artificial delaminations of elliptic shape were inserted in the upper thickness quarter of the plate between the 4^{th} and the 5^{th} layer. The delaminations were located at the same distance, equal to 150 mm from the centre of the plate. For Specimen III delaminations were inserted in the middle of the cross-section of the plate between 8^{th} layer and 9^{th} layer. For Specimen IV, three small delaminations were inserted in the upper quarter of the cross-section of the plate, and three large delaminations were inserted at the lower quarter of the cross-section of the plate between the 12^{th} layer and 13^{th} layer. The details of Specimen II, III, and IV are presented in Fig. 5.14.

Furthermore, the SLDV measurements were conducted from the bottom surface of the plate. Consequently, Specimen II is the most difficult case. It is because the delaminations in the cross-section are farther away from the bottom surface than in other specimens (III and IV). As a consequence, the reflections from delaminations are barely visible in the measured wavefield. For Specimens II, III, and IV, we have generated $f_n = 512$ consecutive frames representing the full wavefield measurements in the plate. The measurement parameters were the same as in the experiment with the single delamination.

Since SLDV measurements were conducted from the bottom surface of the plate, the GT images and the output predictions of the proposed models are flipped horizontally (mirrored). Figure 5.15a shows the GT image of Specimen II. Figure 5.15b shows the predicted output of AE-ConvLSTM model, in which the highest IoU= 0.35 was achieved for window of frames $(68 - 92)$.

Figure 5.15c shows the GT image of Specimen III. Figure 5.15d shows the predicted output of AE-ConvLSTM model, in which the highest IoU= 0.32 was achieved for window of frames $(60 - 84)$.

Figure 5.15e shows the GT image of Specimen IV. The largest delaminations in the cross-sections were assumed to be GT because the full wavefield was acquired from the bottom surface of the specimen. We need to mention that such a case with stacked

delaminations in the cross-section was not modeled numerically (see Specimen IV in Fig. 5.14). Although the models were not trained on such a scenario, the predictions were satisfactory. Figure 5.15f shows the predicted output of AE-ConvLSTM model, in which the highest IoU= 0.27 was achieved for window of frames $(68 - 92)$.

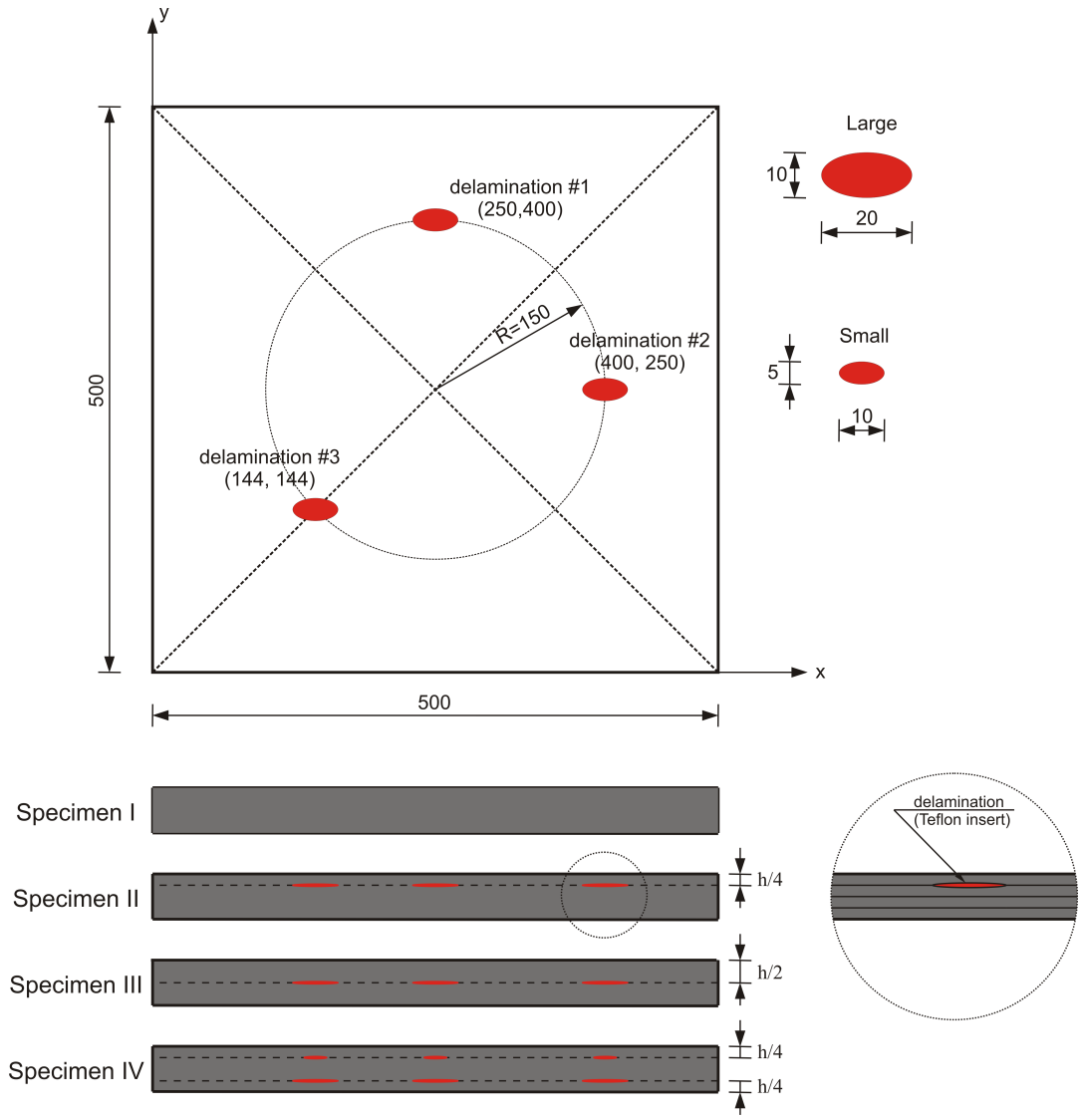

Figure 5.14: Delamination arrangements in the specimen.

It is worth mentioning that FCN-DenseNet model was tested, which I developed previously [164] for data related to specimens II-IV. However, poor results were obtained. This is attributed to the fact that RMS images are fed to FCN-DenseNet, which carries a limited amount of damage-related information. On the other hand, currently proposed methods utilise full wavefield frames, which carry more damage-reach features.

Moreover, in Fig. 5.16a, we presented the calculated IoU values corresponding to predicted outputs of AE-ConvLSTM model regarding Specimen IV as the window

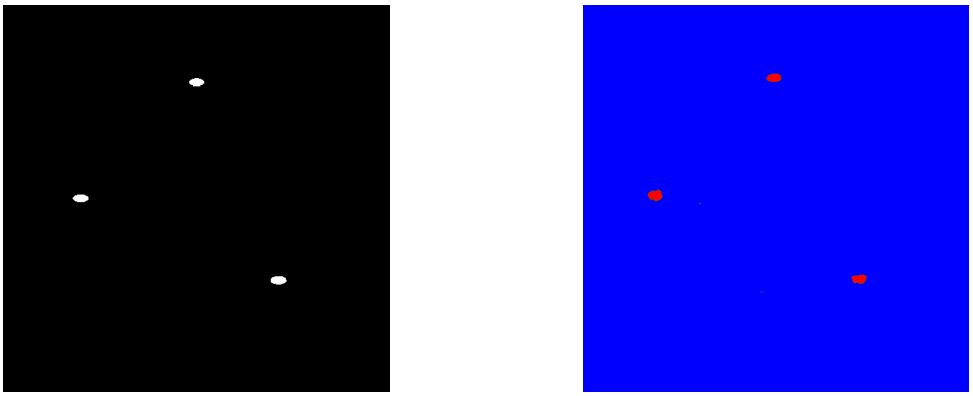

(a) GT of Specimen II.

(b) IoU = 0.35.

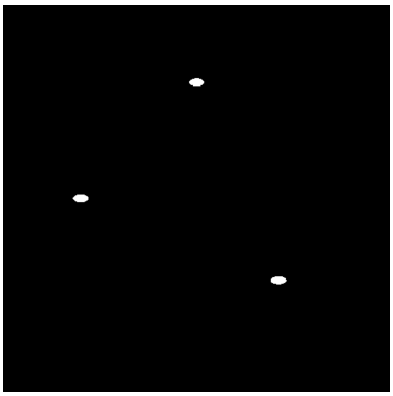

(c) GT of Specimen III.

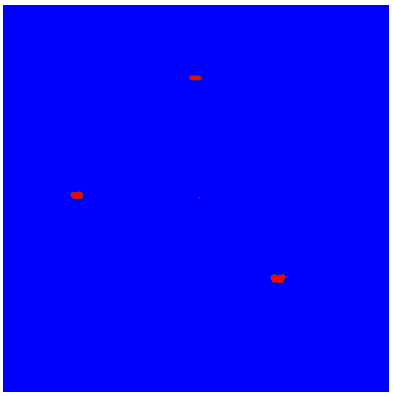

(d) IoU = 0.32.

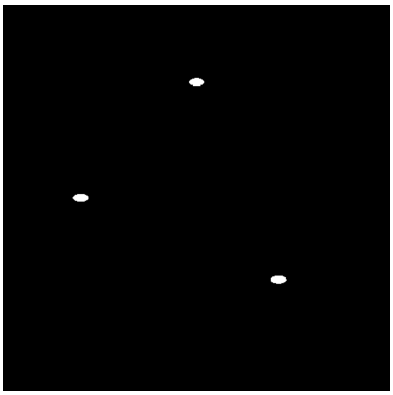

(e) GT of Specimen IV.

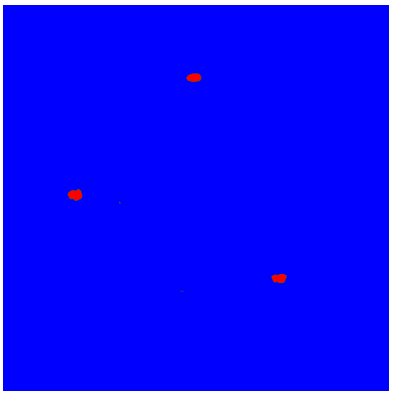

(f) IoU = 0.27.

Figure 5.15: Experimental cases of Specimens II, III, and IV.

of size 24 frames slides, over the 512 full wavefield frames. The developed model starts to identify the delaminations after propagating guided waves interact with the delaminations.

The red square depicted in Fig. 5.16b corresponds to IoU value calculated for the window of frames before the interactions with delaminations (the frame for the centre of the window is shown). This behaviour is expected since the models were trained on those frames depicting the beginning of the interactions of guided wave with delamination.

As a result, valuable patterns start to appear later on.

The light blue star depicted in Fig. 5.16 refers to a window of frames regarding the initial interactions of propagating guided waves with the delaminations and before reflecting from the edges. Hence, valuable patterns regarding the damage are starting to appear.

The pink pentagon shape depicted in Fig. 5.16 refers to a window of frames that pass the initial interaction with the delaminations. Furthermore, it shows the reflections of the guided waves from the edges just before interacting with the delaminations again. As can be seen, the calculated IoU values drop drastically. Because the model learns patterns of the wavefront as it passes through the delamination region, which has high amplitudes, it neglects reflections caused by delamination because they have low amplitudes.

The green circle depicted in Fig. 5.16 refers to the a window of frames that represent waves reflection from boundaries and their interaction with the damage. Although this frame shows complex patterns of wave reflections, the model can extract the valuable damage features and identify the delaminations accordingly.

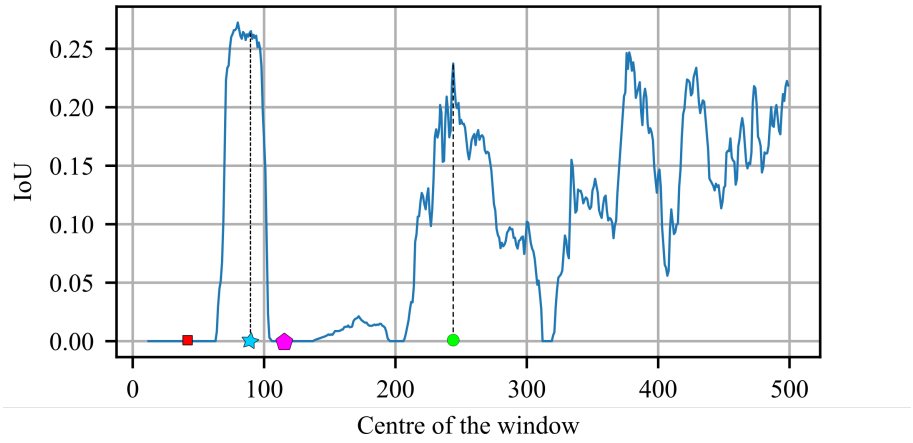

(a) IoU for the sliding window centered at consecutive frames.

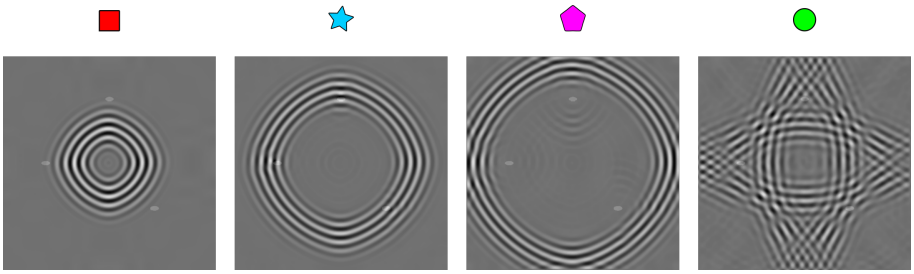

(b) Corresponding frames regarding the centre of the windows of frames of guided waves.

Figure 5.16: IoU for the sliding window of frames (Specimen IV).

Figure 5.17 shows the predicted outputs corresponding to the window of frames for the red square, light blue star, pink pentagon, and green circle, respectively.

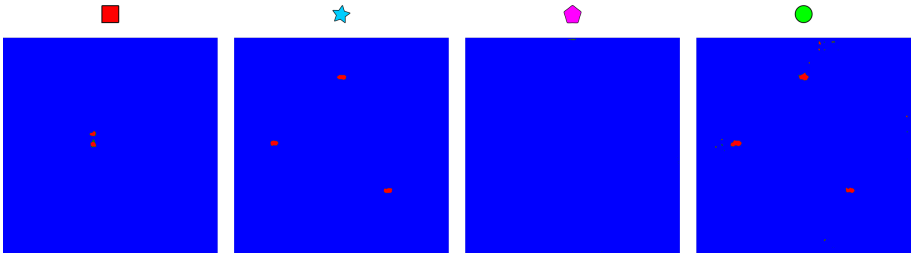

Figure 5.17: Predictions for window centered at selected frames (Specimen IV).

The RMS image depicting the damage map of Specimen IV is presented in Fig. 5.18a. Figure 5.18b shows the thresholded RMS image, and the calculated IoU= 0.23.

Furthermore, the mean percentage area error ϵ with respect to the three delaminations (Specimen IV) is equal to 10.61%.

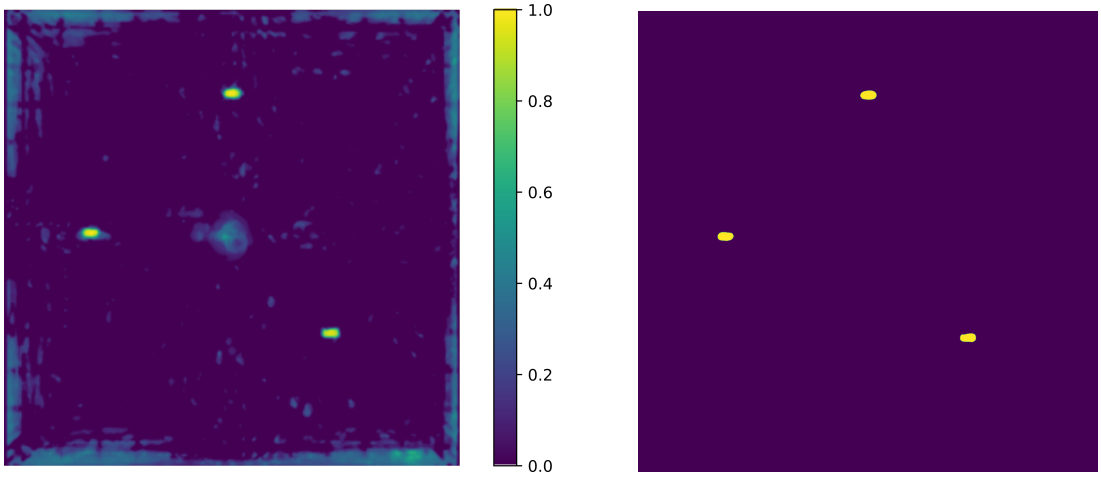

(a) (b)

Figure 5.18: Specimen IV: (a) RMS image (damage map), (b) Thresholded RMS image.

5.4 Predictions of DLSR model

In this section, the performance evaluation of the developed DLSR model based on the numerical test cases are presented. The DLSR model was trained on the full wavefield animation of a window size 128 frames per case Accordingly, each numerical test case was evaluated at three different frames (time steps):

- The first frame represents the initial interaction of the guided waves with the delamination (the first frame in the window).
- The second frame represents the interaction with the delamination after 64 frames of the initial interaction (the middle frame in the window).
- The third frame represents the interaction with the delamination after 128 frames of the first frame (the last frame in the window).

Additionally, the developed DLSR model was evaluated in an experimental test case to demonstrate its capability for super-resolution image reconstruction. Additionally, the conventional CS approach was applied as a reference with a different number of points used for the reconstruction of the wavefield in the experimental test case. Moreover, two types of masks (sub-sampling schemes) for the construction of the measurement matrix were tested, namely random mask and jitter mask. The jitter mask was defined according to the algorithm presented in [68]. It should be noted that in the CS method, priors were not exploited.

5.4.1 Numerical cases

The results of recovering HR frames for the first numerical test case by the developed DLSR model are presented in Fig. 5.19. In this case, the delamination is located at the upper left quarter of the plate. The reference frames for this test case are $N_f = 127$, $N_f = 191$, and $N_f = 255$ presented in Figs. 5.19a, 5.19b and 5.19c, respectively. Additionally, the region of guided waves interaction with the delamination is depicted with a square box. Figures 5.19d, 5.19e, and 5.19f show the corresponding recovered frame at $N_f = 127$, $N_f = 191$, and $N_f = 255$, respectively, with the DLSR model.

The calculated quality metrics for the whole plate regarding the first test case are presented in Table 5.8, which proves that the DLSR model can map the LR frames to HR frames with high quality.

Figure 5.20 presents a zoom in at the delamination region that shows the interaction of the guided waves with the delamination regarding the test case presented in Fig. 5.19.

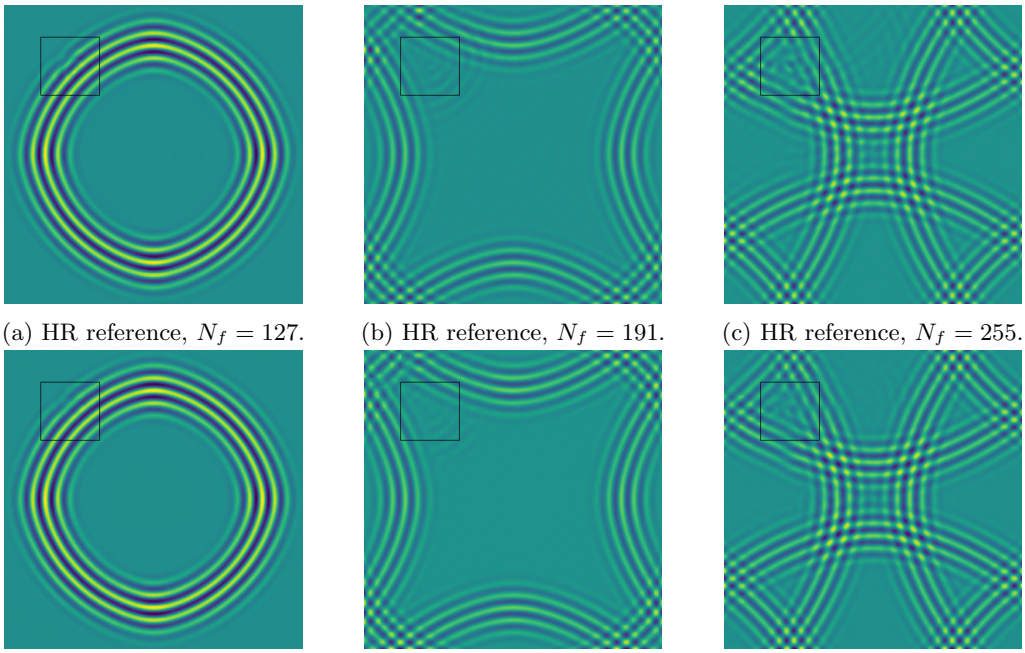

(a) HR reference, $N_f = 127$. (b) HR reference, $N_f = 191$. (c) HR reference, $N_f = 255$.

(d) SR frame, $N_f = 127$. (e) SR frame, $N_f = 191$. (f) SR frame, $N_f = 255$.

Figure 5.19: First numerical case with respect to the reconstruction of whole plate.

Figures 5.20a, 5.20b, and 5.20c show the reference delamination regions with respect to Figs. 5.19a, 5.19b, and 5.19c, respectively. Figures 5.20d, 5.20e, and 5.20f show the zoom in of the reconstructed frames of Figs. 5.19d, 5.19e, and 5.19f, respectively.

The calculated quality metrics for the delamination region regarding the first test case are presented in Table 5.8. The acquired quality proves that the DLSR model can map the LR frames to HR frames with high quality at the delamination region.

Figure 5.21 show the results of HR frames reconstruction for the second numerical test case by the developed DLSR model. Furthermore, the delamination is located at the upper edge centre of the plate in this case. The reference frames for this test case are $N_f = 154$, $N_f = 218$, and $N_f = 282$ presented in Figs. 5.21a, 5.21b and 5.21c, respectively. The region of guided waves interaction with the delamination is depicted with a square box. Figures 5.21d, 5.21e, and 5.21f show the corresponding recovered frame at $N_f = 154$, $N_f = 218$, and $N_f = 282$, respectively, with the DLSR model.

The calculated quality metrics for the whole plate regarding the second test case are presented in Table 5.8. The results prove that the DLSR model can map the LR frames to HR frames with high quality.

Figure 5.22 presents a zoom in at the delamination region that shows the interaction of the guided waves with the delamination regarding the test case presented in Fig. 5.21. Figures 5.22a, 5.22b, and 5.22c show the reference delamination regions with respect to Figs. 5.21a, 5.21b, and 5.21c, respectively. Figures.5.22d, 5.22e, and 5.22f show the

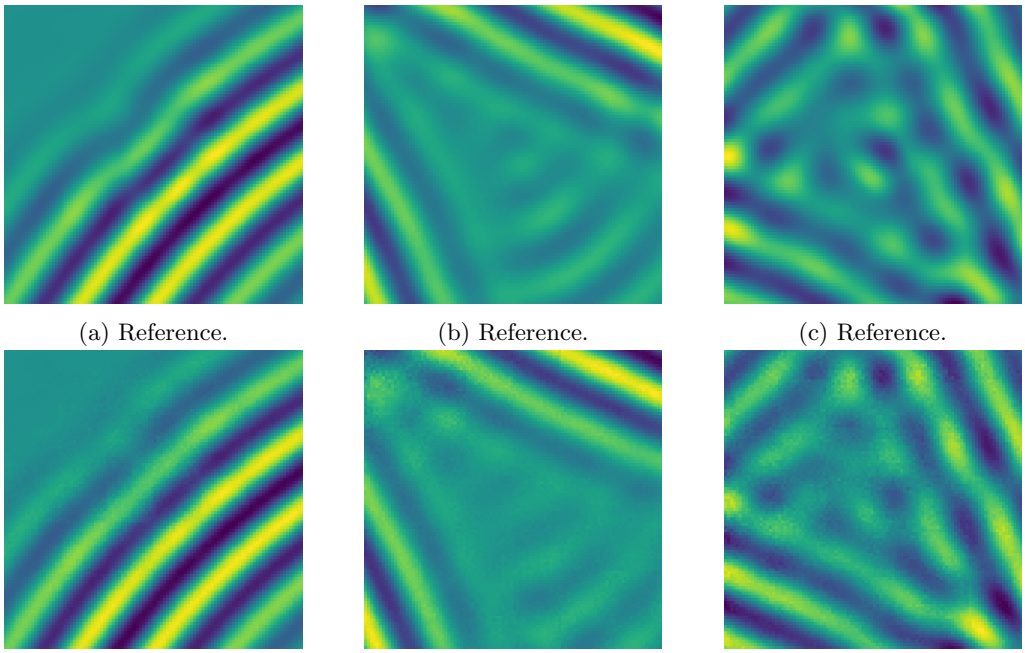

(a) Reference. (b) Reference. (c) Reference.

(d) Prediction. (e) Prediction. (f) Prediction.

Figure 5.20: First numerical case with respect to the delamination region.

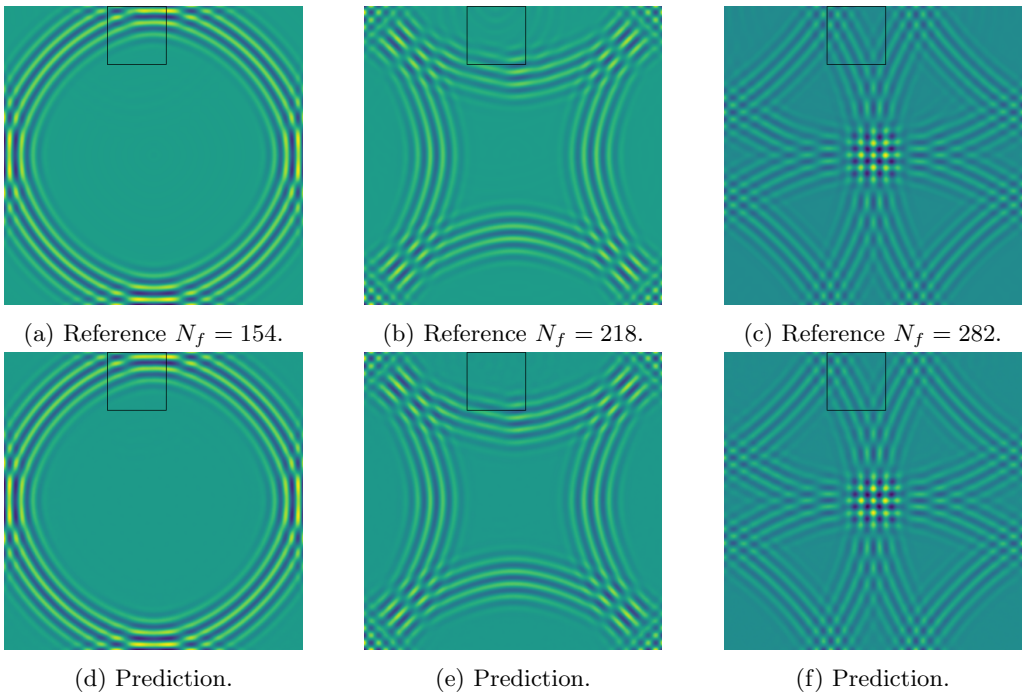

(a) Reference $N_f = 154$. (b) Reference $N_f = 218$. (c) Reference $N_f = 282$.

(d) Prediction. (e) Prediction. (f) Prediction.

Figure 5.21: Second numerical case with respect to the reconstruction of whole plate.

zoom in of the reconstructed frames of Figs.5.21d, 5.21e, and 5.21f, respectively.

The calculated quality metrics for the delamination region regarding the second test case are presented in Table 5.8. The acquired quality proves that the DLSR model can map the LR frames to HR frames with high quality at the delamination region.

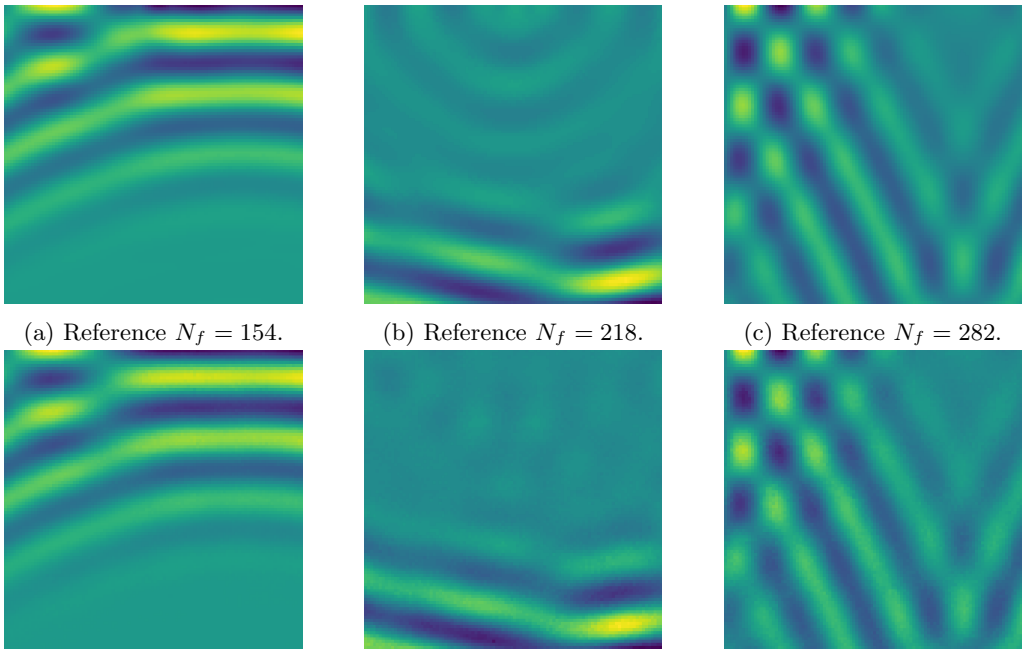

(a) Reference $N_f = 154$. (b) Reference $N_f = 218$. (c) Reference $N_f = 282$.

(d) Prediction. (e) Prediction. (f) Prediction.

Figure 5.22: Second numerical case with respect to the delamination region.

Figure 5.23 show the results of HR frames reconstruction for the third numerical test case by the developed DLSR model. Furthermore, the delamination is located at the left edge centre of the plate in this case. The reference frames for this test case are $N_f = 211$, $N_f = 275$, and $N_f = 339$ presented in Figs. 5.23a, 5.23b and 5.23c, respectively. The region of guided waves interaction with the delamination is depicted with a square box. Figures 5.23d, 5.23e, and 5.23f show the corresponding recovered frame at $N_f = 211$, $N_f = 275$, and $N_f = 339$, respectively, with the DLSR model.

The calculated quality metrics for the whole plate regarding the second test case are presented in Table 5.8. The measured quality metrics prove that the DLSR model can map the LR frames to HR frames with high quality at the delamination region.

Figure 5.24 presents a zoom in at the delamination region that shows the interaction of the guided waves with the delamination regarding the test case presented in Fig. 5.23. Figures 5.24a, 5.24b, and 5.24c show the reference delamination regions with respect to Figs. 5.23a, 5.23b, and 5.23c, respectively. Figures.5.24d, 5.24e, and 5.24f show the zoom in of the reconstructed frames of Figs.5.23d, 5.23e, and 5.23f, respectively. The calculated quality metrics for the delamination region regarding the first test case are presented in Table 5.8. The measured quality metrics prove that the DLSR model can map the LR frames to HR frames with high quality at the delamination region.

Figure 5.25 show the results of HR frames reconstruction for the fourth numerical test case by the developed DLSR model. Furthermore, the delamination is located at the

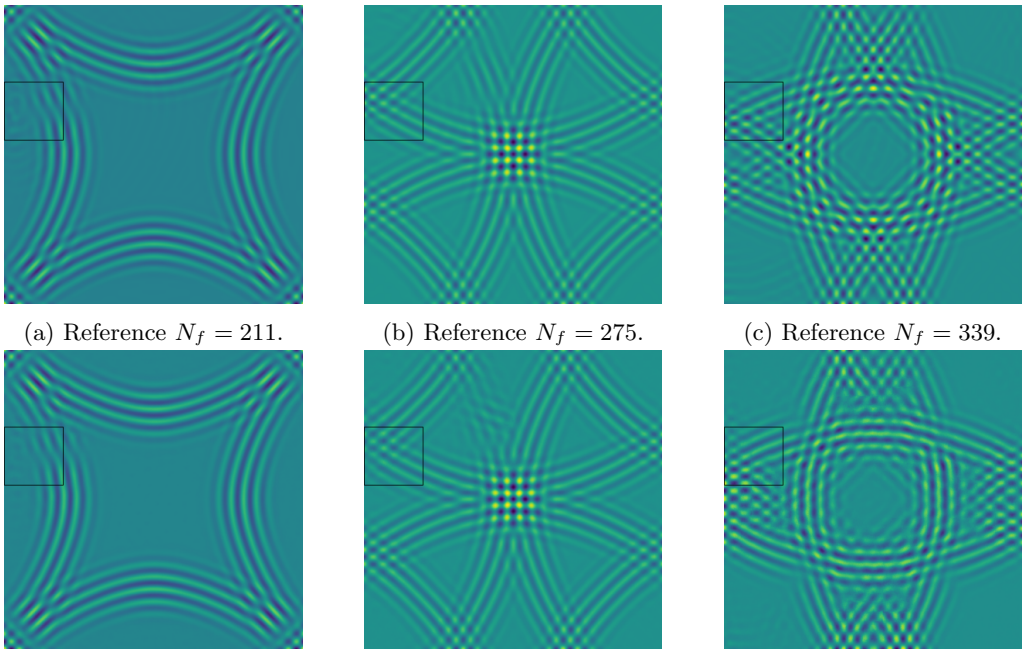

(a) Reference $N_f = 211$. (b) Reference $N_f = 275$. (c) Reference $N_f = 339$.

(d) Prediction. (e) Prediction. (f)

Figure 5.23: Third numerical case with respect to the reconstruction of whole plate.

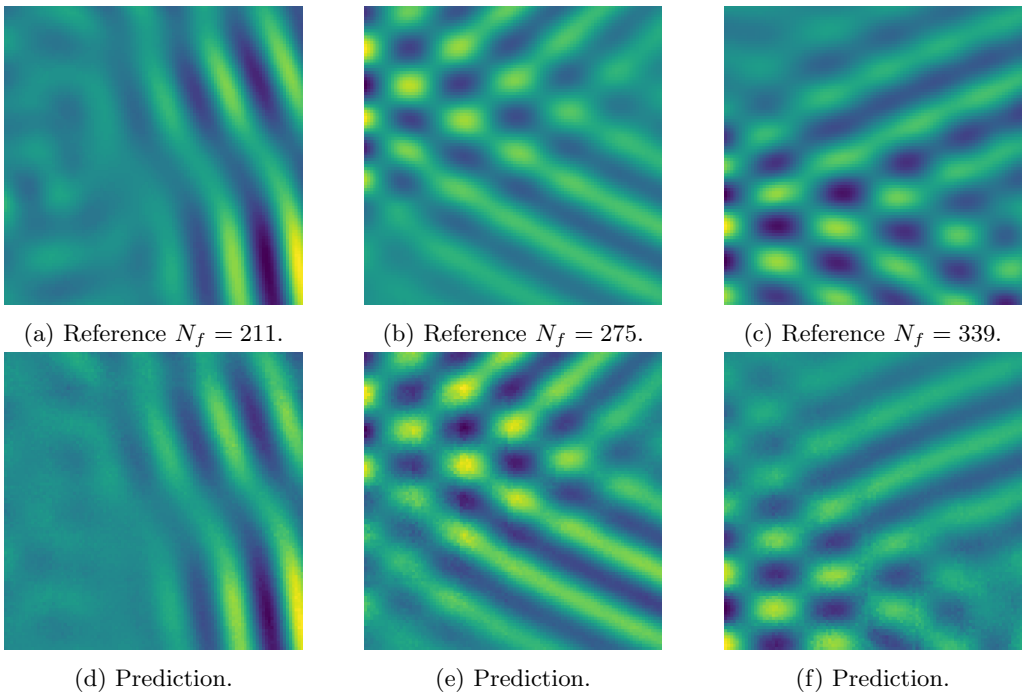

(a) Reference $N_f = 211$. (b) Reference $N_f = 275$. (c) Reference $N_f = 339$.

(d) Prediction. (e) Prediction. (f) Prediction.

Figure 5.24: Third numerical case with respect to the delamination region.

upper left corner of the plate in this case. The reference frames for this test case are $N_f = 159$, $N_f = 223$, and $N_f = 287$ presented in Figs. 5.25a, 5.25b and 5.25c, respectively. The region of guided waves interaction with the delamination is depicted with a square box. Figures 5.25d, 5.25e, and 5.25f show the corresponding recovered frame at $N_f = 159$, $N_f = 223$, and $N_f = 287$, respectively, with the DLSR model.

The calculated quality metrics for the whole plate regarding the second test case are presented in Table 5.8.

Figure 5.26 presents a zoom in at the delamination region that shows the interaction of the guided waves with the delamination regarding the test case presented in Fig. 5.25. Figures 5.26a, 5.26b, and 5.26c show the reference delamination regions with respect to Figs. 5.25a, 5.25b, and 5.25c, respectively. Figures 5.26d, 5.26e, and 5.26f show the zoom in of the reconstructed frames of Figs.5.25d, 5.25e, and 5.25f, respectively. The calculated quality metrics for the delamination region regarding the first test case are presented in Table 5.8.

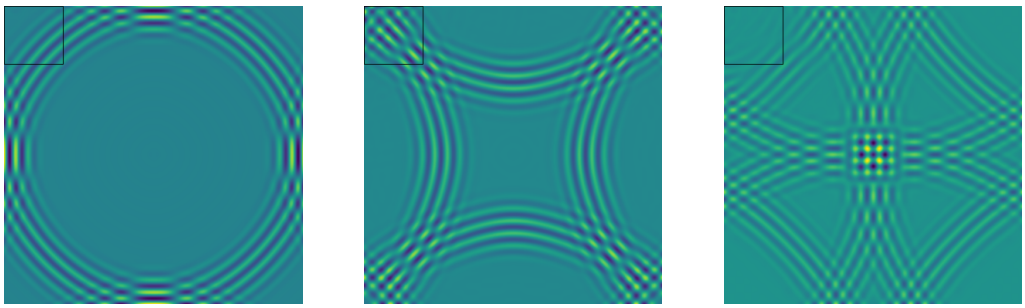

(a) Reference $N_f = 159$. (b) Reference $N_f = 223$. (c) Reference $N_f = 287$.

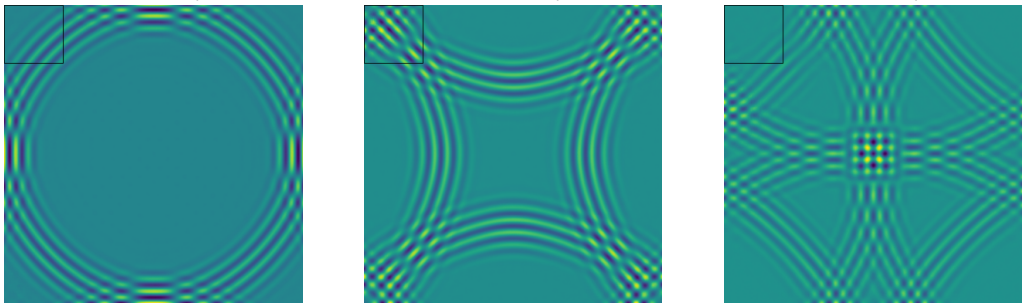

(d) Prediction. (e) Prediction. (f) Prediction.

Figure 5.25: Fourth numerical case with respect to the reconstruction of whole plate.

5.4.2 Experimental case

Experimental studies were performed on a $(500 \times 500 \times 3.9)$ mm^3 CFRP laminate composed of 16 plain-woven prepreg layers (GG 205P) stacked in one direction. During the specimen production, three Teflon inserts were put in between layers at the positions and sizes presented in Fig. 5.27.

Guided waves were excited by 10 mm wide round PZT attached to the centre of the plate front surface with cyanoacrylate glue. A hann-window-modulated 50 kHz five-cycle sinusoidal signals were used for excitation purposes. Out-of-plane velocities were measured in 389286 randomly spaced points covering the whole back surface of the specimen using SLDV. The sampling frequency was 512 kHz, and at each point, 512

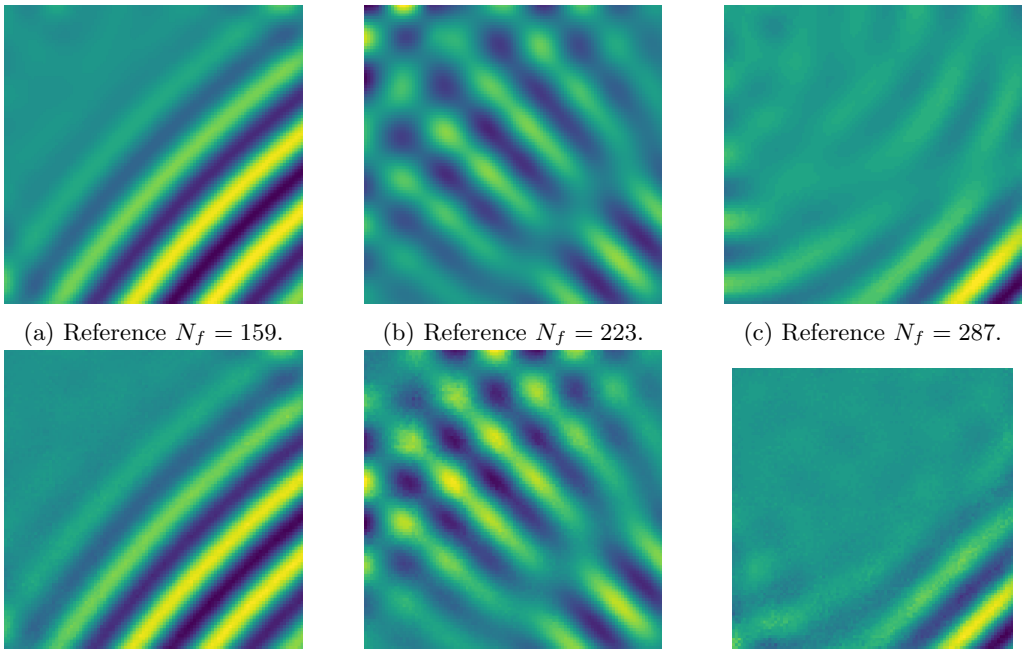

(a) Reference $N_f = 159$. (b) Reference $N_f = 223$. (c) Reference $N_f = 287$.

(d) Prediction. (e) Prediction. (f) Prediction.

Figure 5.26: Fourth numerical case with respect to the delamination region.

Table 5.8: Quality metrics for the DLSR model for four numerical test cases calculated at three different frames N_f per case.

		plate		delamination	
Case	N_f	PSNR	PEARSON CC	PSNR	PEARSON CC
1	127	42.95	0.999	33.02	0.993
	191	39.97	0.993	39.95	0.981
	255	36.91	0.992	30.57	0.948
2	154	47.00	0.998	38.52	0.995
	218	44.87	0.996	41.75	0.972
	282	42.18	0.992	42.05	0.992
3	211	44.37	0.996	40.04	0.980
	275	38.81	0.988	32.92	0.964
	339	24,35	0.829	26.50	0.921
4	159	48.60	0.998	46.67	0.998
	223	37.64	0.989	24.32	0.916
	287	39.64	0.989	40.62	0.871

time samples (1 ms) were registered ten times and averaged. The backside of the specimen was covered with retroreflective film to increase surface reflectivity and thus improve the SNR of measured signals.

Figure 5.28 presents a comparison of the recovered full HR frame and the delamination region at ($N_f = 110$) with various number of measurement points N_p with the CS method. As shown in Fig. 5.28, when the value of N_p increases, we get a better recovery of both the full HR frame and the exact delamination region. However, for lower values of N_P such as $N_p = 1024$, the PSNR and Pearson CC values for the

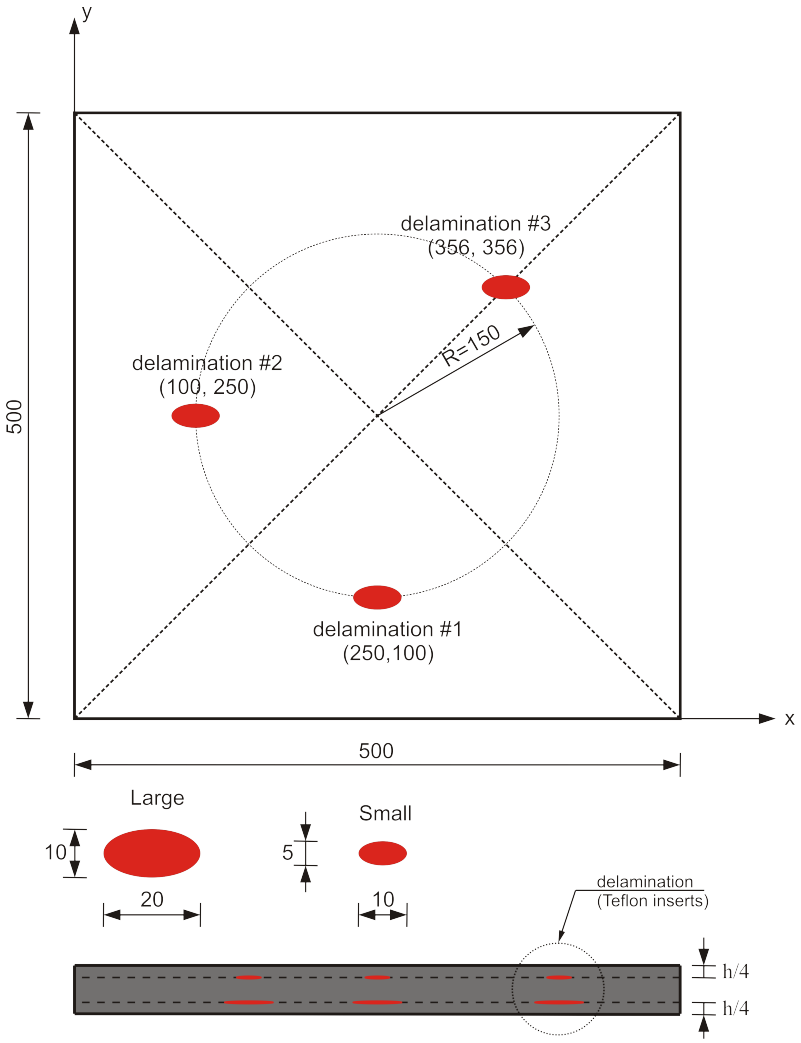

Figure 5.27: Delamination arrangements in the specimen.

recovered HR frame were poor, indicating that the conventional CS method is not efficient below the Nyquist sampling rate.

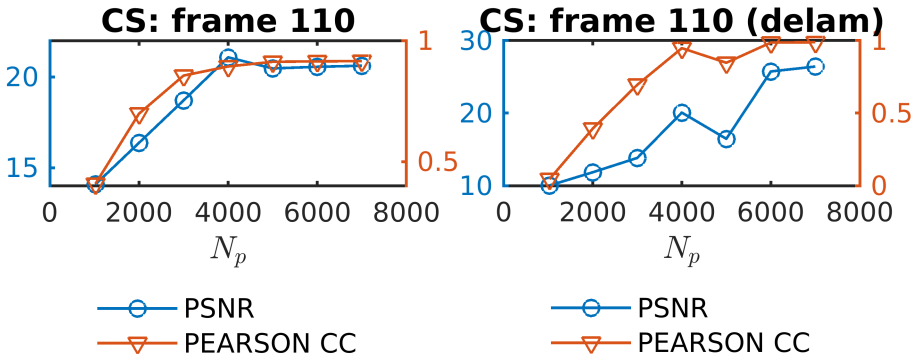

Figure 5.28: Comparison of reconstruction accuracy depending on the number of measurement points N_p.

Figure 5.29 shows the recovery of the reference frame presented in Fig. 5.29b at $N_f = 110$ with the CS method and DLSR model. Figures 5.29b, 5.29c and 5.29d show reconstructed HR frames with CS method at $N_p = 1024$, $N_p = 3000$ and $N_p = 4000$ points, respectively. As expected, when decreasing the N_p points, the CS method is not able to recover HR frames accurately. Figure 5.29e presents the reconstructed HR frame with the DLSR model. The DLSR model recovered the HR frame with $N_p = 1024$ points, which is 19.2% of the Nyquist sampling rate.

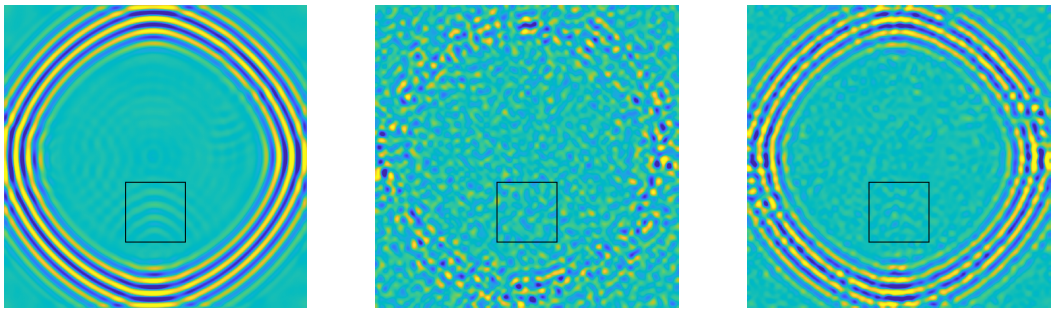

(a) Reference. (b) CS: 1024 points. (c) CS: 3000 points.

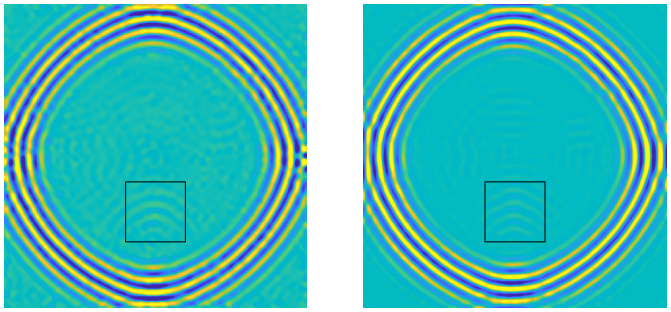

(d) CS: 4000 points. (e) DLSR model

Figure 5.29: Comparison of reference wavefield with reconstructed one by CS and DLSR for the frame $N_f = 110$. Rectangle box indicates the region of the strongest reflection from delamination.

Furthermore, Fig. 5.30 presents the recovery of the HR frame $N_f = 110$ at the delamination region with respect to Fig. 5.29. Figure 5.30a shows the reference region of interest we are attempting to recover, which shows reflected waves from damage. Figures 5.30b and 5.30c show a poor reconstruction of the reflected waves at $N_p = 1024$ and $N_p = 3000$, respectively, using the CS method. Figure 5.30d shows the recovery of the reflected frames at $N_p = 4000$ using the CS method, in which the reflected waves are recognisable. Figure 5.30e shows the recovery of the reflected waves using DLSR model. The recovered reflected waves from damage using DLSR model are visible and can be easily recognised, which indicates that the DLSR approach can be more efficient than the conventional CS method.

Next, reconstruction accuracy metrics were calculated for each consecutive frame N_f and put together in Fig. 5.31. It should be noted that PSNR behaviour is very similar

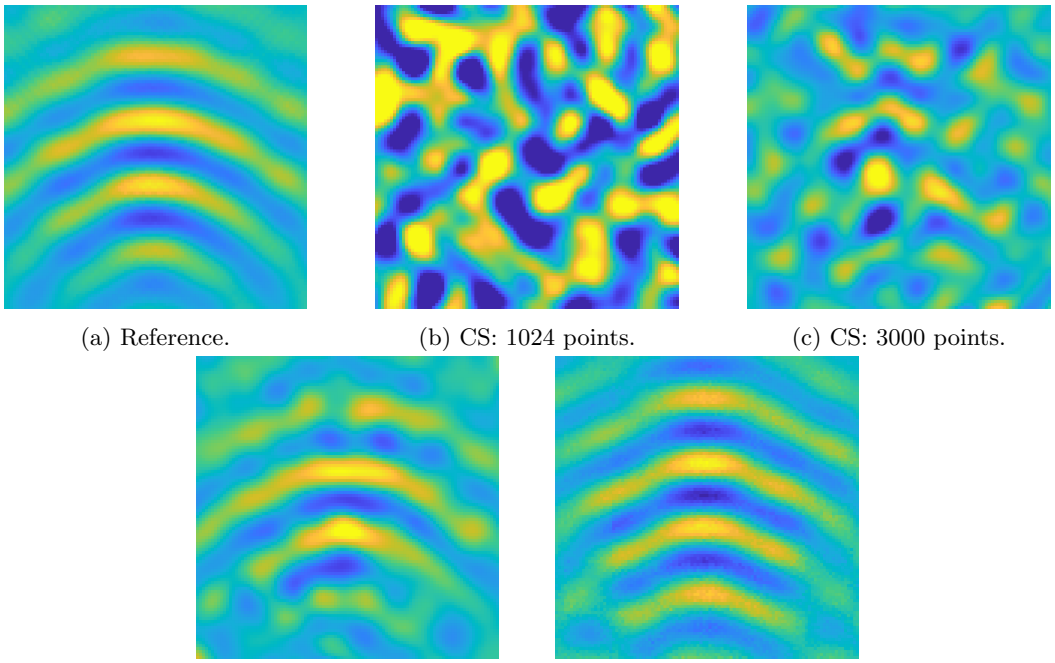

(a) Reference. (b) CS: 1024 points. (c) CS: 3000 points.

(d) CS: 4000 points. (e) DLSR model.

Figure 5.30: Comparison of reference wavefield with reconstructed one by CS and DLSR for the region of delamination reflection (close up region of frame $N_f = 110$ as indicated in Fig. 5.29.

regardless the applied reconstruction method. Moreover, the PSNR values obtained by DLSR model by using only 1024 points are on the level similar to CS by using 3000 points. However, the obtained Pearson CC values for DLSR model is lower than for CS and reach negative values at the frame corresponding to the moment when A0 mode reaches the edges of the plate.

Table 5.9 presents a detailed comparison of the quality metrics for CS methods with applied jitter and random masks and DLSR model for various numbers of points N_p and the corresponding compression ratios CR. Metrics were calculated for the frame $N_f = 110$ on the whole plate and delamination region, respectively. It should be underlined, that for $N_p = 1024$ points, the CS recovery algorithm behaves poorly at the delamination region whereas DLSR model is still able to achieve high PSNR and Pearson CC values.

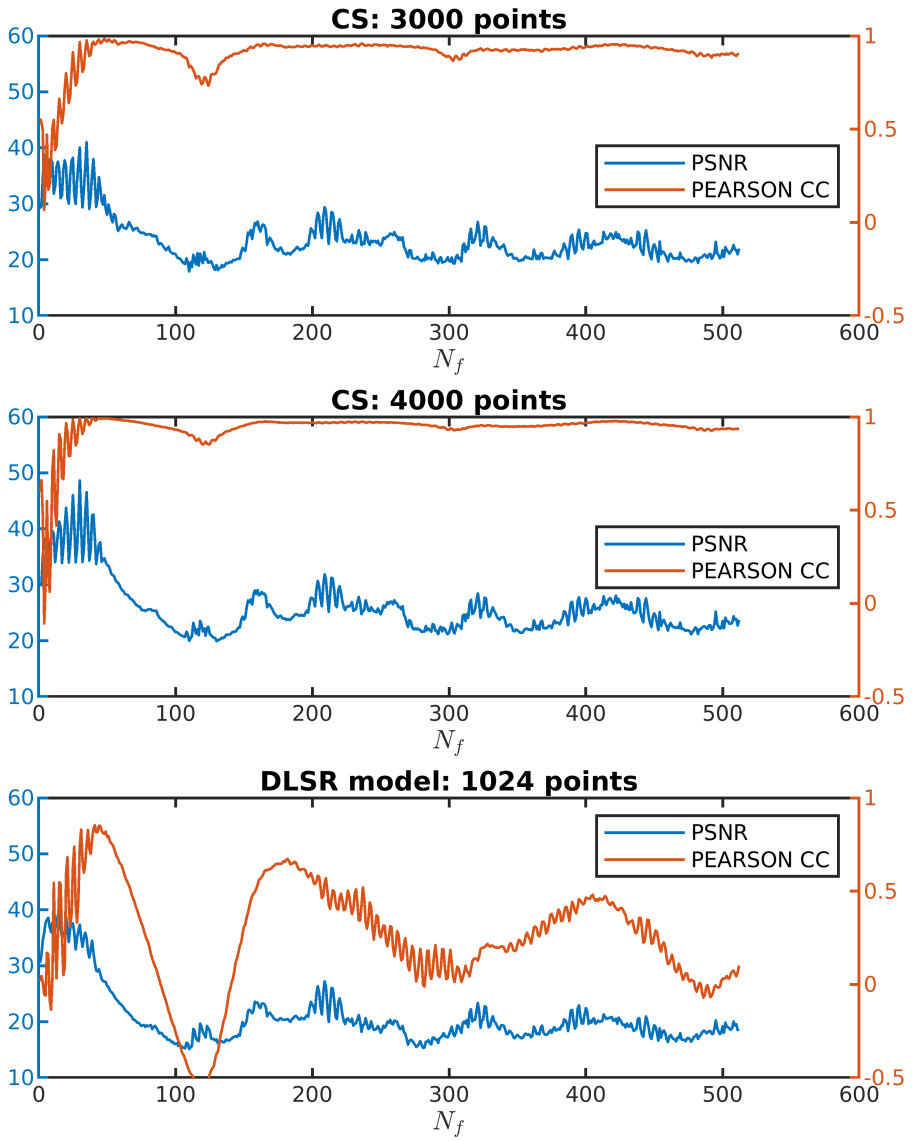

Figure 5.31: Comparison of reconstruction accuracy at frame number N_f.

Table 5.9: Quality metrics for tested methods for various number of points N_p and corresponding compression ratios CR calculated for the frame no $N_f = 110$.

			plate		delamination	
Method	N_p	CR [%]	PSNR	PEARSON CC	PSNR	PEARSON CC
DLSR Model	1024	19.2	15.1	-0.46	31.9	0.71
CS: jitter	1024	19.2	13.3	0.4	11.7	0.16
CS: random	1024	19.2	13.4	0.41	10.2	0.24
CS: jitter	3000	56.3	19.2	0.88	14.9	0.8
CS: random	3000	56.3	17.9	0.83	14	0.57
CS: jitter	4000	75.1	20.8	0.91	19.6	0.94
CS: random	4000	75.1	17.9	0.83	14	0.57

5.5 Summary

The results of investigating several end-to-end DL models are presented in this chapter. The developed DL models were trained on a large synthetically generated dataset representing the full wavefield of the Lamb waves propagating in a CFRP plate and their interaction with discontinuities such as delamination and the plate edges, acquired by SLDV.

The first developed DL models were trained on RMS images to perform delamination detection and localisation through bounding boxes. Hence, two CNN models were developed according to the RMS image resolution of 14×14 and 16×16 blocks with a size of 32×32 pixels, respectively. The CNN models were evaluated on numerical test cases, proving their ability to detect and localise delamination in previously unseen data. The IoU metric was applied to evaluate the obtained results. However, these models were not able to predict delaminations properly for the experimental test cases.

The DL models for pixel-wise image segmentation were also trained on RMS images in a one-to-one scheme to perform delamination identification. Accordingly, five FCN models were developed: Res-UNet, VGG16 encoder-decoder, FCN-DenseNet, PSPNet, and GCN. The FCN models were evaluated on numerical test cases demonstrating their ability to identify delamination in previously unseen data. Furthermore, the FCN models were evaluated on an experimental test case, in which the models showed their capability to generalise.

The AE ConvLSTM model was trained on a many-to-one scheme, in which a number of full wavefield frames were input to the DL model to perform delamination identification. To evaluate the performance of the AE ConvLSTM model, I tested it on several numerical test cases, showing its ability to identify the delamination of previously unseen data. The AE ConvLSTM model was evaluated on several experimental test cases, indicating its capability to generalise well.

The last developed DL model (DLSR) presents a remarkable way of acquiring HR wavefields with fewer measuring points to reduce acquisition time. The DLSR model was also numerically and experimentally evaluated. It demonstrates its ability to recover HR frames from the LR frames with high accuracy, resulting in a significantly faster data acquisition process.

Chapter 6

Conclusions and Future work

In this chapter, I present the conclusions regarding the outcomes of the work presented in this dissertation. Furthermore, I present the potential future work that could be carried out from the present work.

6.1 Conclusions

The importance of SHM systems originated from their ability to monitor the condition of structures in real-time. SHM systems can be developed using data-driven methods, which require a huge amount of data that are captured by monitoring the status of a structure. In recent years, non-contact systems have gained attention for damage detection and localisation in SHM applications. Full wavefields of elastic waves propagation can be excited by a fixed piezoelectric transducer and measured using scanning laser Doppler vibrometry (SLDV). The main objective of this dissertation was to investigate the feasibility of utilising deep learning-based approaches for delamination identification in composite laminated structures. Accordingly, in this dissertation, I present for the first time the utilisation of the full wavefield of Lamb waves propagation in composite laminates along with deep learning approaches for delamination identification.

Full wavefields of elastic waves propagating in a composite laminate contain extensive, valuable, and complex information regarding the discontinuities in the plate, such as delamination or edges. Such information can be utilised to train deep learning models to perform damage identification in an end-to-end approach. Accordingly, with deep learning approaches, it is possible to use registered data in its raw form without the need to perform feature engineering, extraction, and classification. Hence, such an approach has an end-to-end structure that automatically learns and discovers the hidden features in high-dimensional input data. Although deep learning approaches usually require

more time during training, they can still sustain rapid and faster testing compared to conventional signal processing and machine learning methods.

The main outcomes of this dissertation can be summarized as follow:

- Developing CNN classifier models capable of performing the first levels of SHM, namely damage detection and localisation.
- Developing several FCN models for image semantic segmentation capable of performing damage identification and size estimation through training on RMS images of the full wavefields. Moreover, applying data augmentation techniques to the training dataset (475 RMS images) such as flipping the images horizontally, vertically, and diagonally and further applying K-fold cross-validation to the training dataset have improved the performance of the developed models in their generalisation capability. The results were promising, and the deep learning models surpassed the conventional technique ii.e. adaptive wavenumber filtering in detecting delaminations of different shapes, sizes and angles in the unseen numerically generated data. Additionally, the models show their ability to generalise by detecting the delamination in the experimentally acquired data.
- Developing a novel deep learning-based method that presents an end-to-end approach that performs a many-to-one sequence prediction to detect the location, size, and shape of delamination. The developed model can identify and estimate delaminations through simultaneously processing a sequence of a certain number of frames of a full wavefield. Therefore, using a certain number of full wavefield frames is sufficient for delamination identification. To assess its generalisation capability, the model was evaluated on various experimentally measured cases of single and multiple Teflon-insert delaminations. The results were promising, and yet the experimental case of multiple delaminations was difficult because the model had only been trained on scenarios with single delamination. As a result, the model demonstrated its ability to detect multiple delaminations at once in real-world scenarios.
- It can be concluded that the performance of the AE-ConvLSTM model, which takes animations of full wavefield as an input, surpasses that of the FCN models that take only the RMS images as input.
- Despite the advantages of acquiring full wavefield by SLDV, it requires several hours of automatic measurements to improve the signal-to-noise ratio (SNR) of ultrasonic responses via averaging procedures. Therefore, there is a paramount

need to develop a method to speed up data acquisition while simultaneously maintaining the valuable and complex information content obtained from the full wavefield. Consequently, a deep learning model was developed for super-resolution image reconstruction that can recover the high-resolution full wavefield frames with high accuracy from the low-resolution acquired full wavefield by SLDV. To assess the feasibility of such approach, the DLSR model was compared to the traditional CS technique. The results were promising, with the deep learning model outperforming the traditional technique in reconstructing the full wavefield frames for the significantly sub-sampled case (less than 1% of the scan points of the full grid). Furthermore, by reconstructing the full wavefield frames obtained experimentally by SLDV, DLSR model demonstrated the ability to generalize. As a result, it is worth noting that using deep learning approaches for SR frame reconstruction outperforms traditional CS techniques.

6.2 Future work

In the conducted research work, the developed deep learning models for damage detection and localisation were trained on a single type of defect, "delamination", in CFRP structures. Therefore, this work can be expanded to identify other types of defects in CFRP structures. It is noteworthy to mention that generating the utilised dataset in the developed models in this work took roughly three months of computation. However, with the advances in computational power, such a dataset can be generated in a reasonable time. Accordingly, such a dataset will be utilised to train deep learning models that can detect and localise different types of defects at once in an end-to-end approach. The performance of the developed models can be further improved if they are trained on experimental data, allowing them to learn new complex patterns. However, the presented studies are limited to only one type of signal at a carrier frequency of 50 kHz. Accordingly, a new dataset with a higher excitation frequency or broadband frequency (chirp signal) can be generated. Furthermore, the proposed approaches have proven to be feasible for delamination identification. As a result, the next step would be to acquire a large experimental data set consisting of full wavefields from structures with stiffeners and rivets as well as basic plate-like structures. In comparison to a naive numerical data set, such data would significantly improve the performance of the proposed models.

Furthermore, the developed model for super-resolution image reconstruction in this work, trained only on a low-resolution dataset with a compression ratio of 19.2% of the Nyquist sampling rate, which can be further extended to various compression ratios. Another issue that can be further explored and investigated is when recovering an HR frame from an LR frame acquired with a very compressed number of scanning points (below Nyquist sampling rate).

Bibliography

[1] J. Wu, X. Xu, C. Liu, C. Deng, and X. Shao. "Lamb wave-based damage detection of composite structures using deep convolutional neural network and continuous wavelet transform". In: *Composite Structures* 276 (2021), p. 114590.

[2] K. L. Reifsnider, E. G. Henneke, W. W. Stinchcomb, and J. C. Duke. "Damage mechanics and NDE of composite laminates". In: *Mechanics of composite materials*. Elsevier, 1983, pp. 399–420.

[3] D. Balageas, C. P. Fritzen, and A. Güemes. *Structural Health Monitoring*. Ed. by D. Balageas, C.-P. Fritzen, and A. Gemes. London, UK: ISTE, 2010, pp. 1–495.

[4] F. G. Yuan. *Structural Health Monitoring (SHM) in aerospace structures*. Elsevier, 2016, pp. 1–495.

[5] R. Grimberg, D. Prémel, A. Savin, Y. Le Bihan, and D. Placko. "Eddy current holography evaluation of delamination in carbon-epoxy composites". In: *Insight* 43.4 (2001), pp. 260–264.

[6] A. Raghavan and C. E. S. Cesnik. "The Shock and Vibration Digest Review of Guided-wave Structural Health Monitoring". In: *The Shock and Vibration Digest* 39 (2007), pp. 91–114.

[7] D. E. Adams and C. R. Farrar. "Classifying Linear and Nonlinear Structural Damage Using Frequency Domain ARX Models". In: *Structural Health Monitoring* 1.2 (2002), pp. 185–201.

[8] S. W. Doebling, C. R. Farrar, and M. B. Prime. "A summary review of vibration-based damage identification methods". In: *Shock and Vibration Digest* 30.2 (1998), pp. 91–105.

[9] T. Uhl. "The use and challenge of modal analysis in diagnostics". In: *Diagnostyka* 30 (2004), pp. 151–160.

[10] C. U. Grosse and M. Ohtsu. *Acoustic emission testing: Basics for Research-Applications in Civil Engineering*. Springer Berlin Heidelberg, 2008, pp. 1–404.

[11] T. Stepinski, T. Uhl, and W. Staszewski. *Advanced Structural Damage Detection*. Wiley, 2013.

[12] F. Campbell. *Structural Composite Materials*. ASM International, 2010, p. 612.

[13] A. N. Guz' and G. V. Guz'. *Mechanics of composite materials with large-scale curving of filler*. Vol. 18. 4. Taylor Francis, 1983, pp. 434–439.

[14] W. J. Cantwell and J. Morton. "The impact resistance of composite materials - a review". In: *Composites* 22.5 (1991), pp. 347–362.

[15] G. Ramirez. "Book Reviews: Design and Optimization of Laminated Composite Materials". In: *Journal of Structural Engineering* 125.9 (1999), pp. 1082–1082.

[16] J. Cai, L. Qiu, S. Yuan, L. Shi, P. Liu, and D. Liang. "Structural Health Monitoring for Composite Materials". In: *Composites and Their Applications*. InTech, 2012.

[17] S. Nur Azrie Bt Safri, M. T. Sultan, and M. Jawaid. "Damage analysis of glass fiber reinforced composites". In: *Durability and Life Prediction in Biocomposites, Fibre-Reinforced Composites and Hybrid Composites*. Elsevier, 2018, pp. 133–147.

[18] S. Hassani, M. Mousavi, and A. H. Gandomi. "Structural health monitoring in composite structures: A comprehensive review". In: *Sensors* 22.1 (2022), pp. 1–45.

[19] A. Güemes, A. Fernández-López, P. F. Díaz-Maroto, A. Lozano, and J. Sierra-Perez. "Structural health monitoring in composite structures by fiber-optic sensors". In: *Sensors (Switzerland)* 18.4 (2018).

[20] W. Ostachowicz, P. Kudela, M. Krawczuk, and A. Zak. *Guided waves in structures for SHM: the time-domain spectral element method*. John Wiley and Sons, 2011.

[21] C. Willberg. "Development of a new isogeometric finite element and its application for Lamb wave based structural health monitoring". PhD thesis. Magdeburg, 2013, p. 137.

[22] M. Mitra and S. Gopalakrishnan. "Guided wave based structural health monitoring: A review". In: *Smart Materials and Structures* 25.5 (2016), p. 053001.

[23] A. J. Croxford, P. D. Wilcox, B. W. Drinkwater, and G Konstantinidis. "Strategies for guided-wave structural health monitoring". In: *Proceedings of the Royal Society A: Mathematical, Physical and Engineering Sciences* 463.2087 (2007), pp. 2961–2981.

[24] D. C. Worlton. "Experimental confirmation of lamb waves at megacycle frequencies". In: *Journal of Applied Physics* 32.6 (1961), pp. 967–971.

[25] C. Willberg, S. Duczek, J. M. Vivar-Perez, and Z. A. B. Ahmad. "Simulation Methods for Guided Wave-Based Structural Health Monitoring: A Review". In: *Applied Mechanics Reviews* 67.1 (2015).

[26] S. S. Kessler, S. M. Spearing, and C. Soutis. "Damage detection in composite materials using Lamb wave methods". In: *Smart Materials and Structures* 11.2 (2002), pp. 269–278.

[27] J. B. Ihn and F. K. Chang. "Pitch-catch active sensing methods in structural health monitoring for aircraft structures". In: *Structural Health Monitoring* 7.1 (2008), pp. 5–19.

[28] J. B. Ihn and F. K. Chang. "Detection and monitoring of hidden fatigue crack growth using a built-in piezoelectric sensor/actuator network: I. Diagnostics". In: *Smart Materials and Structures* 13.3 (2004), pp. 609–620.

[29] W. Ostachowicz, T. Wandowski, and P. Malinowski. "Combined distributed and concentrated transducer network for failure indication". In: *Health Monitoring of Structural and Biological Systems 2010*. Vol. 7650. SPIE, 2010, 76503A.

[30] C. R. Farrar and K. Worden. *Structural Health Monitoring: A Machine Learning Perspective*. John Wiley and Sons, 2012.

[31] V. Giurgiutiu. "Structural health monitoring with piezoelectric wafer active sensors". In: *16th International Conference on Adaptive Structures and Technologies*. 2006, pp. 94–100.

[32] P. D. Wilcox. "Omni-directional guided wave transducer arrays for the rapid inspection of large areas of plate structures". In: *IEEE Transactions on Ultrasonics, Ferroelectrics, and Frequency Control* 50.6 (2003), pp. 699–709.

[33] P. Malinowski, T. Wandowski, I. Trendafilova, and W. Ostachowicz. "A phased array-based method for damage detection and localization in thin plates". In: *Structural Health Monitoring* 8.1 (2009), pp. 5–15.

[34] F. Schubert. "A conceptual study on guided wave based imaging techniques for SHM with distributed transducer array". In: *Proc. Structural Health Monitoring*. 2008, pp. 748–757.

[35] W. Qiang and Y. Shenfang. "Baseline-free imaging method based on new pzt sensor arrangements". In: *Journal of Intelligent Material Systems and Structures* 20.14 (2009), pp. 1663–1673.

[36] P. Malinowski, T. Wandowski, and W. Ostachowicz. "Damage detection potential of a triangular piezoelectric configuration". In: *Mechanical Systems and Signal Processing*. Vol. 25. 7. DEStech Publications, 2011, pp. 2722–2732.

[37] O. Putkis, R. P. Dalton, and A. J. Croxford. "The influence of temperature variations on ultrasonic guided waves in anisotropic CFRP plates". In: *Ultrasonics* 60 (2015), pp. 109–116.

[38] A. Marzani and S. Salamone. "Numerical prediction and experimental verification of temperature effect on plate waves generated and received by piezoceramic sensors". In: *Mechanical Systems and Signal Processing* 30 (2012), pp. 204–217.

[39] W. Ostachowicz, M. Radzieński, and P. Kudela. "50th Anniversary Article: Comparison Studies of Full Wavefield Signal Processing for Crack Detection". In: *Strain* 50.4 (2014), pp. 275–291.

[40] A. B. Stanbridge and D. J. Ewins. "Modal testing using a scanning laser Doppler vibrometer". In: *Mechanical Systems and Signal Processing* 13.2 (1999), pp. 255–270.

[41] M. N. Helfrick, C. Niezrecki, P. Avitabile, and T. Schmidt. "3D digital image correlation methods for full-field vibration measurement". In: *Mechanical Systems and Signal Processing* 25.3 (2011), pp. 917–927.

[42] L. Yu and Z. Tian. "Lamb wave Structural Health Monitoring Using a Hybrid PZT-Laser Vibrometer Approach". In: *Structural Health Monitoring: An International Journal* 12.5-6 (2013), pp. 469–483.

[43] M. Ruzzene. "Frequency-wavenumber domain filtering for improved damage visualization". In: *Ultrasonic and Advanced Methods for Nondestructive Testing*

and Material Characterization. World Scientific Publishing Co., 2007, pp. 591–611.

[44] P. Kudela, M. Radzieński, and W. Ostachowicz. "Identification of cracks in thin-walled structures by means of wavenumber filtering". In: *Mechanical Systems and Signal Processing* 50-51 (2015), pp. 456–466.

[45] M. S. Harb and F. G. Yuan. "A rapid, fully non-contact, hybrid system for generating Lamb wave dispersion curves". In: *Ultrasonics* 61 (2015), pp. 62–70.

[46] B Lamboul, B Passilly, J. M. Roche, and D Osmont. "Impact damage detection in sandwich composite structures using Lamb waves and laser vibrometry". In: *AIP Conference Proceedings*. Vol. 1511. American Institute of Physics Inc., 2013, pp. 1003–1010.

[47] M. Radzieński, P. Kudela, A. Marzani, L. De Marchi, and W. Ostachowicz. "Damage identification in various types of composite plates using guided waves excited by a piezoelectric transducer and measured by a laser vibrometer". In: *Sensors (Switzerland)* 19.9 (2019), p. 1958.

[48] H Sohn, D Dutta, J. Y. Yang, M Desimio, S Olson, and E Swenson. "Automated detection of delamination and disbond from wavefield images obtained using a scanning laser vibrometer". In: *Smart Materials and Structures* 20.4 (2011), p. 045017.

[49] Y. K. An. "Impact-Induced Delamination Detection of Composites Based on Laser Ultrasonic Zero-Lag Cross-Correlation Imaging". In: *Advances in Materials Science and Engineering* 2016 (2016).

[50] M. D. Rogge and C. A. Leckey. "Characterization of impact damage in composite laminates using guided wavefield imaging and local wavenumber domain analysis". In: *Ultrasonics*. Vol. 53. 7. Elsevier, 2013, pp. 1217–1226.

[51] Z. Tian, Y. Lingyu, C. Leckey, and J. Seebo. "Guided wave imaging for detection and evaluation of impact-induced delamination in composites". In: *Smart Materials and Structures* 24.10 (2015), p. 105019.

[52] E. B. Flynn, S. Y. Chong, G. J. Jarmer, and J. R. Lee. "Structural imaging through local wavenumber estimation of guided waves". In: *NDT and E International* 59 (2013), pp. 1–10.

[53] P. Kudela, M. Radzienski, and W. Ostachowicz. "Impact induced damage assessment by means of Lamb wave image processing". In: *Mechanical Systems and Signal Processing* 102 (2018), pp. 23–36.

[54] J. Segers, S. Hedayatrasa, G. Poelman, W. Van Paepegem, and M. Kersemans. "Robust and baseline-free full-field defect detection in complex composite parts through weighted broadband energy mapping of mode-removed guided waves". In: *Mechanical Systems and Signal Processing* 151.November (2021).

[55] J. Segers, S. Hedayatrasa, G. Poelman, W. Van Paepegem, and M. Kersemans. "Self-reference broadband local wavenumber estimation (SRB-LWE) for defect assessment in composites". In: *Mechanical Systems and Signal Processing* 163.June (2022).

[56] E. Candes, J. Romberg, and T. Tao. "Stable Signal Recovery from Incomplete and Inaccurate Measurements". In: *Communications on Pure and Applied Mathematics* 8.59 (2006), pp. 1207–1223.

[57] D. Donoho. "Compressed sensing". In: *IEEE Transactions on Information Theory* 52.4 (2006), pp. 1289–1306.

[58] S. S. Chen, D. L. Donoho, and M. A. Saunders. "Atomic Decomposition by Basis Pursuit". In: *SIAM Journal on Scientific Computing* 20.1 (1998), pp. 33–61.

[59] E. Van den Berg and M. P. Friedlander. "Probing the pareto frontier for basis pursuit solutions". In: *SIAM Journal on Scientific Computing* 31.2 (2008), pp. 890–912.

[60] E Van Den Berg and M. P. Friedlander. *SPGL1: A solver for large-scale sparse reconstruction*. 2007.

[61] M. Lustig, D. Donoho, and J. M. Pauly. "Sparse MRI: The application of compressed sensing for rapid MR imaging". In: *Magnetic Resonance in Medicine* 58.6 (2007), pp. 1182–1195.

[62] Z. Gao, L. Dai, S. Han, I. Chih-Lin, Z. Wang, and L. Hanzo. "Compressive Sensing Techniques for Next-Generation Wireless Communications". In: *IEEE Wireless Communications* 25.3 (2018), pp. 144–153. arXiv: `1709.01757`.

[63] F. Herrmann, M. Friedlander, and O. Yilmaz. "Fighting the Curse of Dimensionality: Compressive Sensing in Exploration Seismology". In: *IEEE Signal Processing Magazine* 29.3 (2012), pp. 88–100.

[64] J. B. Harley and J. M. F. Moura. "Sparse recovery of the multimodal and dispersive characteristics of Lamb waves". In: *The Journal of the Acoustical Society of America* 133.5 (2013), pp. 2732–2745.

[65] O. Mesnil and M. Ruzzene. "Sparse wavefield reconstruction and source detection using Compressed Sensing". In: *Ultrasonics* 67 (2016), pp. 94–104.

[66] A. Perelli, T. Di Ianni, L. De Marchi, N. Testoni, and N. Speciale. "Compressive Sensing with warped frequency models in lamb waves damage detection procedures". In: *2012 IEEE International Ultrasonics Symposium*. 2012, pp. 154–157.

[67] A. Perelli, L. De Marchi, L. Flamigni, A. Marzani, and G. Masetti. "Best basis compressive sensing of guided waves in structural health monitoring". In: *Digital Signal Processing: A Review Journal* 42 (2015), pp. 35–42.

[68] T. Di Ianni, L. De Marchi, A. Perelli, and A. Marzani. "Compressive sensing of full wave field data for structural health monitoring applications". In: *IEEE Transactions on Ultrasonics, Ferroelectrics, and Frequency Control* 62.7 (2015), pp. 1373–1383.

[69] Y. Keshmiri Esfandabadi, L. De Marchi, N. Testoni, A. Marzani, and G. Masetti. "Full Wavefield Analysis and Damage Imaging Through Compressive Sensing in Lamb Wave Inspections". In: *IEEE Transactions on Ultrasonics, Ferroelectrics, and Frequency Control* 65.2 (2018), pp. 269–280.

[70] M. Chang, S. Yuan, and F. Guo. "Corrosion monitoring using a new compressed sensing-based tomographic method". In: *Ultrasonics* 101.June 2019 (2020).

[71] R. Dahl, M. Norouzi, and J. Shlens. "Pixel Recursive Super Resolution". In: *Proceedings of the IEEE International Conference on Computer Vision* 2017-Octob (2017), pp. 5449–5458. arXiv: 1702.00783.

[72] Y. Zhang, Y. Tian, Y. Kong, B. Zhong, and Y. Fu. "Residual Dense Network for Image Super-Resolution". In: *Proceedings of the IEEE Computer Society Conference on Computer Vision and Pattern Recognition*. Salt Lake City, June 18-22: IEEE, 2018, pp. 2472–2481.

[73] X. Wang, K. Yu, S. Wu, J. Gu, Y. Liu, C. Dong, Y. Qiao, and C. C. Loy. "ESRGAN: Enhanced super-resolution generative adversarial networks". In: *Proceedings of the European conference on computer vision (ECCV) workshops*. Ed. by L. Leal-Taixé and S. Roth. Vol. 11133 LNCS. Cham: Springer, 2018, pp. 63–79. arXiv: 1809.00219.

[74] Z. Zhang and V. Sze. "FAST: A Framework to Accelerate Super-Resolution Processing on Compressed Videos". In: *IEEE Computer Society Conference on Computer Vision and Pattern Recognition Workshops* 2017-July (2017), pp. 1015–1024. arXiv: 1603.08968.

[75] B. Yan, C. Lin, and W. Tan. "Frame and Feature-Context Video Super-Resolution". In: *Proceedings of the AAAI Conference on Artificial Intelligence* 33 (2019), pp. 5597–5604.

[76] M. Claypool, K. Claypool, and F. Damaa. "The effects of frame rate and resolution on users playing first person shooter games". In: *Multimedia Computing and Networking 2006* 6071 (2006), p. 607101.

[77] B. Park and H. Sohn. "Reconstruction of laser ultrasonic wavefield images from reduced sparse measurements using compressed sensing aided super-resolution". In: *AIP Conference Proceedings* 1806 (2017).

[78] Y. Keshmiri Esfandabadi, M. Bilodeau, P. Masson, and L. De Marchi. "Deep learning for enhancing wavefield image quality in fast non-contact inspections". In: *Structural Health Monitoring* 19.4 (2020), pp. 1003–1016.

[79] G. Brewka. "Artificial intelligence-a modern approach by Stuart Russell and Peter Norvig, Prentice Hall. Series in Artificial Intelligence, Englewood Cliffs, NJ." In: *The Knowledge Engineering Review* 11.1 (1996), pp. 78–79. arXiv: 9809069v1 [arXiv:gr-qc].

[80] C. R. Farrar and K. Worden. "An introduction to structural health monitoring". In: *Philosophical Transactions of the Royal Society A: Mathematical, Physical and Engineering Sciences* 365.1851 (2007), pp. 303–315.

[81] C. R. Farrar, S. W. Doebling, and D. A. Nix. "Vibration-based structural damage identification". In: *Philosophical Transactions of the Royal Society A: Mathematical, Physical and Engineering Sciences* 359.1778 (2001), pp. 131–149.

[82] K. Worden and G. Manson. "The application of machine learning to structural health monitoring". In: *Philosophical Transactions of the Royal Society A: Mathematical, Physical and Engineering Sciences* 365.1851 (2007), pp. 515–537.

[83] E. Figueiredo and A. Santos. "Machine Learning Algorithms for Damage Detection". In: *Vibration-Based Techniques for Damage Detection and Localization in Engineering Structures* (2018), pp. 1–39.

[84] A. Munoz. "Machine Learning and Optimization". In: (2014).

[85] F. Chollet. *Deep Learning with Python*. 2018.

[86] A. Raghavan and C. E. Cesnik. "Effects of Elevated Temperature on Guided-wave Structural Health Monitoring". In: *Journal of Intelligent Material Systems and Structures* 19.12 (2008), pp. 1383–1398.

[87] Z. Su and L. Ye. "Algorithms for Damage Identification – Fusion of Signal Features". In: *dentification of Damage Using Lamb Waves*. Vol. 48. Springer, London, 2009, pp. 195–254.

[88] J. T. Kim, Y. S. Ryu, H. M. Cho, and N. Stubbs. "Damage identification in beam-type structures: Frequency-based method vs mode-shape-based method". In: *Engineering Structures* 25.1 (2003), pp. 57–67.

[89] M. M. Abdel Wahab and G. De Roeck. "Damage detection in bridges using modal curvatures: Application to a real damage scenario". In: *Journal of Sound and Vibration* 226.2 (1999), pp. 217–235.

[90] R. J. Allemang. "The modal assurance criterion - Twenty years of use and abuse". In: *Sound and Vibration* 37.8 (2003), pp. 14–21.

[91] B. Jaishi and W. X. Ren. "Damage detection by finite element model updating using modal flexibility residual". In: *Journal of Sound and Vibration* 290.1-2 (2006), pp. 369–387.

[92] D. Bernal. "Load Vectors for Damage Localization". In: *Journal of Engineering Mechanics* 128.1 (2002), pp. 7–14.

[93] W. J. Staszewski, K. Worden, and G. R. Tomlinson. "Time-frequency analysis in gearbox fault detection using the Wigner-Ville distribution and pattern recognition". In: *Mechanical Systems and Signal Processing* 11.5 (1997), pp. 673–692.

[94] H. Kim and H. Melhem. "Damage detection of structures by wavelet analysis". In: *Engineering Structures* 26.3 (2004), pp. 347–362.

[95] T. R. Hay, R. L. Royer, H. Gao, X. Zhao, and J. L. Rose. "A comparison of embedded sensor Lamb wave ultrasonic tomography approaches for material loss detection". In: *Smart Materials and Structures* 15.4 (2006), pp. 946–951.

[96] P. Ongsulee. "Artificial intelligence, machine learning and deep learning". In: *International Conference on ICT and Knowledge Engineering*. IEEE Computer Society, 2018, pp. 1–6.

[97] A. Khan, N. Kim, J. K. Shin, H. S. Kim, and B. D. Youn. "Damage assessment of smart composite structures via machine learning: a review". In: *JMST Advances* 1.1-2 (2019), pp. 107–124.

[98] A. Raghavan and C. E. S. Cesnik. "Guided-wave signal processing using chirplet matching pursuits and mode correlation for structural health monitoring". In: *Smart Structures and Materials 2006: Sensors and Smart Structures Technologies for Civil, Mechanical, and Aerospace Systems* 6174.May (2006), 61741B.

[99] M. M. Reda Taha, A. Noureldin, J. L. Lucero, and T. J. Baca. *Wavelet transform for structural health monitoring: A compendium of uses and features*. 2006.

[100] A. Graps. "An Introduction to Wavelets". In: *IEEE Computational Science and Engineering* 2.2 (1995), pp. 50–61.

[101] Y. Liu, K. Li, S. Song, Y. Sun, Y. Huang, and J. Wang. "The research of spacecraft electrical characteristics identification and diagnosis using PCA feature extraction". In: *International Conference on Signal Processing Proceedings, ICSP*. Vol. 2015-Janua. October. IEEE. IEEE, 2014, pp. 1413–1417.

[102] C. Wang, W. Guan, J. Gou, F. Hou, J. Bai, and G. Yan. "Principal component analysis based three-dimensional operational modal analysis". In: *International Journal of Applied Electromagnetics and Mechanics* 45.1-4 (2014). Ed. by X. Maldague and T. Takagi, pp. 137–144.

[103] V. H. Nguyen and J.-C. Golinval. "Fault detection based on kernel principal component analysis". In: *Engineering Structures* 32.11 (2010), pp. 3683–3691.

[104] F. Liu, W. Wang, T. Shen, J. Peng, and W. Kong. "Rapid Identification of Kudzu Powder of Different Origins Using Laser-Induced Breakdown Spectroscopy." In: *Sensors (Basel, Switzerland)* 19.6 (2019), p. 1453.

[105] A. Datteo, F. Lucà, and G. Busca. "Statistical pattern recognition approach for long-time monitoring of the G.Meazza stadium by means of AR models and PCA". In: *Engineering Structures* 153 (2017), pp. 317–333.

[106] M. A. Torres-Arredondo, D. A. Tibaduiza, L. E. Mujica, J. Rodellar, and C. P. Fritzen. "Data-driven multivariate algorithms for damage detection and identification: Evaluation and comparison". In: *Structural Health Monitoring* 13.1 (2014), pp. 19–32.

[107] I. Jolliffe. *Principal Component Analysis*. Springer Series in Statistics. New York: Springer-Verlag, 2002, p. 488.

[108] N Dervilis, M Choi, S. G. Taylor, R. J. Barthorpe, G Park, C. R. Farrar, and K Worden. "On damage diagnosis for a wind turbine blade using pattern recognition". In: *Journal of Sound and Vibration* 333.6 (2014), pp. 1833–1850.

[109] K. Worden, G. Manson, and N. R. Fieller. "Damage detection using outlier analysis". In: *Journal of Sound and Vibration* 229.3 (2000), pp. 647–667.

[110] C. R. Farrar and K. Worden. "Machine Learning and Statistical Pattern Recognition". In: *Structural Health Monitoring*. Wiley, 2012, pp. 295–320.

[111] A. P. Dempster, N. M. Laird, and D. B. Rubin. " Maximum Likelihood from Incomplete Data Via the EM Algorithm ". In: *Journal of the Royal Statistical Society: Series B (Methodological)* 39.1 (1977), pp. 1–22.

[112] F.-G. Yuan, S. A. Zargar, Q. Chen, and S. Wang. "Machine learning for structural health monitoring: challenges and opportunities". In: *Proc. of SPIE*. Vol. 11379. 23. SPIE-Intl Soc Optical Eng, 2020, p. 2.

[113] Y. LeCun, Y. Bengio, and G. Hinton. "Deep learning". In: *Nature* 521.7553 (2015), pp. 436–444.

[114] J. Brownlee. *Long Short-term Memory Networks with Python: Develop Sequence Prediction Models with Deep Learning*. Vol. 1. 1. Jason Brownlee, 2017, p. 228.

[115] K. Fukushima. "Neocognitron: A self-organizing neural network model for a mechanism of pattern recognition unaffected by shift in position". In: *Biological Cybernetics* 36.4 (1980), pp. 193–202.

[116] A. Krizhevsky, I. Sutskever, and G. E. Hinton. "ImageNet classification with deep convolutional neural networks". In: *Communications of the ACM* 60.6 (2017), pp. 84–90.

[117] P. J. Werbos. "Backpropagation Through Time: What It Does and How to Do It". In: *Proceedings of the IEEE* 78.10 (1990), pp. 1550–1560.

[118] S. Hochreiter and J. Schmidhuber. "Long Short-Term Memory". In: *Neural Computation* 9.8 (1997), pp. 1735–1780.

[119] A. Graves and N. Jaitly. "Towards end-to-end speech recognition with recurrent neural networks". In: *International conference on machine learning*. PMLR. 2014, pp. 1764–1772.

[120] K. Cho, B. van Merriënboer, D. Bahdanau, and Y. Bengio. "On the properties of neural machine translation: Encoder–decoder approaches". In: *Proceedings of SSST 2014 - 8th Workshop on Syntax, Semantics and Structure in Statistical Translation* (2014), pp. 103–111. arXiv: `1409.1259`.

[121] S. H. I. Xingjian, Z. Chen, H. Wang, D.-Y. Yeung, W.-K. Wong, and W.-c. Woo. "Convolutional LSTM network: A machine learning approach for precipitation nowcasting". In: *Advances in neural information processing systems*. 2015, pp. 802–810.

[122] Y. LeCun, Y. Bengio, and G. Hinton. "Deep learning". In: *Nature* 521.7553 (2015), pp. 436–444.

[123] J. Schmidhuber. "Deep Learning in neural networks: An overview". In: *Neural Networks* 61 (2015), pp. 85–117. arXiv: `1404.7828`.

[124] K. Worden, C. R. Farrar, G. Manson, and G. Park. "The fundamental axioms of structural health monitoring". In: *Proceedings of the Royal Society A: Mathematical, Physical and Engineering Sciences* 463.2082 (2007), pp. 1639–1664.

[125] S. Das, A. Chattopadhyay, and A. N. Srivastava. "Classifying induced damage in composite plates using one-class support vector machines". In: *AIAA Journal* 48.4 (2010), pp. 705–718.

[126] G. Dib, O. Karpenko, E. Koricho, A. Khomenko, M. Haq, and L. Udpa. "Ensembles of novelty detection classifiers for structural health monitoring using guided waves". In: *Smart Materials and Structures* 27.1 (2018).

[127] J. Vitola, M. A. Vejar, D. A. T. Burgos, and F. Pozo. "Data-Driven Methodologies for Structural Damage Detection Based on Machine Learning Applications". In: *Pattern Recognition - Analysis and Applications* (2016).

[128] D. A. Tibaduiza, L. E. Mujica, J. Rodellar, and A. Güemes. "Structural damage detection using principal component analysis and damage indices". In: *Journal of Intelligent Material Systems and Structures* 27.2 (2016), pp. 233–248.

[129] N Godin, S Huguet, R Gaertner, and L Salmon. "Clustering of acoustic emission signals collected during tensile tests on unidirectional glass/polyester composite

using supervised and unsupervised classifiers". In: *NDT & E International* 37.4 (2004), pp. 253–264.

[130] T. Kohonen. "The self-organizing map". In: *Proceedings of the IEEE* 78.9 (1990), pp. 1464–1480.

[131] P. Nazarko and L. Ziemiański. "Application of elastic waves and neural networks for the prediction of forces in bolts of flange connections subjected to static tension tests". In: *Materials* 13.16 (2020), p. 3607.

[132] F. Pashmforoush, R. Khamedi, M. Fotouhi, M. Hajikhani, and M. Ahmadi. "Damage Classification of Sandwich Composites Using Acoustic Emission Technique and k-means Genetic Algorithm". In: *Journal of Nondestructive Evaluation* 33.4 (2014), pp. 481–492.

[133] P. Nazarko and L. Ziemianski. "Damage detection in aluminum and composite elements using neural networks for Lamb waves signal processing". In: *Engineering Failure Analysis* 69 (2016), pp. 97–107.

[134] Y.-J. J. Cha, W. Choi, and O. Büyüköztürk. "Deep Learning-Based Crack Damage Detection Using Convolutional Neural Networks". In: *Computer-Aided Civil and Infrastructure Engineering* 32.5 (2017), pp. 361–378.

[135] Y. Z. Lin, Z. H. Nie, and H. W. Ma. "Structural Damage Detection with Automatic Feature-Extraction through Deep Learning". In: *Computer-Aided Civil and Infrastructure Engineering* 32.12 (2017), pp. 1025–1046.

[136] Z. Liu, Y. Cao, Y. Wang, and W. Wang. "Computer vision-based concrete crack detection using U-net fully convolutional networks". In: *Automation in Construction* 104 (2019), pp. 129–139.

[137] G. H. Beckman, D. Polyzois, and Y. J. Cha. "Deep learning-based automatic volumetric damage quantification using depth camera". In: *Automation in Construction* 99 (2019), pp. 114–124.

[138] W. Choi and Y. J. Cha. "SDDNet: Real-Time Crack Segmentation". In: *IEEE Transactions on Industrial Electronics* 67.9 (2020), pp. 8016–8025.

[139] M. Słoński, K. Schabowicz, and E. Krawczyk. "Detection of flaws in concrete using ultrasonic tomography and convolutional neural networks". In: *Materials* 13.7 (2020), p. 1557.

[140] M. Słoński and M. Tekieli. "2D digital image correlation and region-based convolutional neural network in monitoring and evaluation of surface cracks in concrete structural elements". In: *Materials* 13.16 (2020), p. 3527.

[141] M. Słoński. "A comparison of deep convolutional neural networks for image-based detection of concrete surface cracks". In: *Computer Assisted Methods in Engineering and Science* 26.2 (2019), pp. 105–112.

[142] A. Güemes, A. Fernandez-Lopez, A. R. Pozo, and J. Sierra-Pérez. *Structural health monitoring for advanced composite structures: A review.* 2020.

[143] J. Melville, K. S. Alguri, C. Deemer, and J. B. Harley. "Structural damage detection using deep learning of ultrasonic guided waves". In: *AIP Conference Proceedings* 1949 (2018), p. 230006.

[144] D. Sammons, W. P. Winfree, E. Burke, and S. Ji. "Segmenting delaminations in carbon fiber reinforced polymer composite CT using convolutional neural networks". In: *AIP Conference Proceedings* 1706 (2016).

[145] D. Chetwynd, F. Mustapha, K. Worden, J. A. Rongong, S. G. Pierce, and J. M. Dulieu-Barton. "Damage Localisation in a Stiffened Composite Panel". In: *Strain* 44.4 (2008), pp. 298–307.

[146] A. De Fenza, A. Sorrentino, and P. Vitiello. "Application of Artificial Neural Networks and Probability Ellipse methods for damage detection using Lamb waves". In: *Composite Structures* 133 (2015), pp. 390–403.

[147] V. Ewald, R. M. Groves, and R. Benedictus. "DeepSHM: A deep learning approach for structural health monitoring based on guided Lamb wave technique". In: *Sensors and Smart Structures Technologies for Civil, Mechanical, and Aerospace Systems*. February. 2019, pp. 84–99.

[148] Y. Keshmiri Esfandabadi, M. Bilodeau, P. Masson, and L. De Marchi. "Deep learning for enhancing wavefield image quality in fast non-contact inspections". In: *Structural Health Monitoring* 19.4 (2020), pp. 1003–1016.

[149] J. Melville, K. S. Alguri, C. Deemer, and J. B. Harley. "Structural damage detection using deep learning of ultrasonic guided waves". In: *AIP Conference Proceedings* 1949.April (2018).

[150] J. Melville. "Structural Damage Detection Using Dictionary Learning". PhD thesis. The University of Utah, 2017.

[151] F. Chollet. *Keras*. `https://github.com/fchollet/keras/`. 2015.

[152] M. Abadi, A. Agarwal, P. Barham, E. Brevdo, Z. Chen, C. Citro, G. S. Corrado, A. Davis, J. Dean, M. Devin, et al. "TensorFlow: Large-Scale Machine Learning on Heterogeneous Distributed Systems". In: *arXiv preprint arXiv:1603.04467* (2016). arXiv: `1603.04467`.

[153] P. Kudela, J. Moll, and P. Fiborek. "Parallel spectral element method for guided wave based structural health monitoring". In: *Smart Materials and Structures* 29.9 (2020), p. 095010.

[154] E. Shelhamer, J. Long, and T. Darrell. "Fully Convolutional Networks for Semantic Segmentation". In: *IEEE Transactions on Pattern Analysis and Machine Intelligence* 39.4 (2017), pp. 640–651. arXiv: `1411.4038`.

[155] G. Bonaccorso. *Mastering Machine Learning Algorithms: Expert techniques for implementing popular machine learning algorithms, fine-tuning your models, and understanding how they work*. Packt Publishing Ltd, 2020, p. 798.

[156] P. Kudela. "RMS of Lamb wavefield interacting with delamination - numerical". In: *Mendeley Data* V1 (2020).

[157] K. Srinivasan, A. K. Cherukuri, D. R. Vincent, A. Garg, and B. Y. Chen. "An efficient implementation of artificial neural networks with K-fold cross-validation for process optimization". In: *Journal of Internet Technology* 20.4 (2019), pp. 1213–1225.

[158] K. He, X. Zhang, S. Ren, and J. Sun. "Deep residual learning for image recognition". In: *Proceedings of the IEEE Computer Society Conference on Computer Vision*

and Pattern Recognition. Vol. 2016-Decem. 2016, pp. 770–778. arXiv: 1512.03385.

[159] O. Ronneberger, P. Fischer, and T. Brox. "U-net: Convolutional networks for biomedical image segmentation". In: *International Conference on Medical image computing and computer-assisted intervention*. Vol. 9351. Springer Verlag, 2015, pp. 234–241. arXiv: 1505.04597.

[160] K. Simonyan and A. Zisserman. "Very deep convolutional networks for large-scale image recognition". In: *3rd International Conference on Learning Representations, ICLR 2015 - Conference Track Proceedings*. Packt Publishing, 2015, pp. 1–14. arXiv: 1409.1556.

[161] S. Jegou, M. Drozdzal, D. Vazquez, A. Romero, and Y. Bengio. "The One Hundred Layers Tiramisu: Fully Convolutional DenseNets for Semantic Segmentation". In: *IEEE Computer Society Conference on Computer Vision and Pattern Recognition Workshops*. Vol. 2017-July. Packt Publishing, 2017, pp. 1175–1183. arXiv: 1611.09326.

[162] H. Zhao, J. Shi, X. Qi, X. Wang, and J. Jia. "Pyramid scene parsing network". In: *30th IEEE Conference on Computer Vision and Pattern Recognition, CVPR 2017*. Vol. 2017-Janua. Packt Publishing, 2017, pp. 6230–6239. arXiv: 1612.01105.

[163] C. Peng, X. Zhang, G. Yu, G. Luo, and J. Sun. "Large kernel matters - Improve semantic segmentation by global convolutional network". In: *Proceedings - 30th IEEE Conference on Computer Vision and Pattern Recognition, CVPR 2017*. Vol. 2017-Janua. Packt Publishing, 2017, pp. 1743–1751. arXiv: 1703.02719.

[164] A. A. Ijjeh, S. Ullah, and P. Kudela. "Full wavefield processing by using FCN for delamination detection". In: *Mechanical Systems and Signal Processing* 153 (2021), p. 107537.

[165] P. Kudela and A. Ijjeh. *Synthetic dataset of a full wavefield representing the propagation of Lamb waves and their interactions with delaminations*. 2021.

[166] W. Shi, J. Caballero, F. Huszar, J. Totz, A. P. Aitken, R. Bishop, D. Rueckert, and Z. Wang. "Real-Time Single Image and Video Super-Resolution Using an Efficient Sub-Pixel Convolutional Neural Network". In: *Proceedings of the IEEE Computer Society Conference on Computer Vision and Pattern Recognition*. Vol. 2016-Decem. IEEE Computer Society, 2016, pp. 1874–1883. arXiv: 1609.05158.

[167] A. A. Ijjeh and P. Kudela. "Deep learning based segmentation using full wavefield processing for delamination identification: A comparative study". In: *Mechanical Systems and Signal Processing* 168 (2022), p. 108671.